Doctoral Dissertation

Microfluidic device for high-throughput and high-sensitive flow cytometry toward cell and droplet analysis

（細胞と液滴の高速・高精度フローサイトメトリー解析に向けたマイクロ流体デバイスの開発）

Liu Xun

September 2023

Division of Material Science

Graduate School of Science and Technology

Nara Institute of Science and Technology

Contents

1. Introduction

1.1. Flow cytometry in cell detection and analysis

Flow cytometry is a powerful tool for cell detection and analysis; many physical fields can be applied to microfluidic chips to get various morphological and biochemical information from different cells[1], [2]. Fig.1.1 shows the schematics of common commercial flow cytometry, these kinds of cytometry utilize a special nozzle as the hydrodynamic focusing chamber to arrange cells flowing through the detection area. The cell is always detected with fluorescence for most commercial flow cytometry, as shown in Fig.1.1a; in addition, to realize cell sorting, the commercial flow cytometry uses the aqueous droplet in oil as the carrier of cells, with different charging for these droplets, with high-voltage electric field, droplets will be separated.

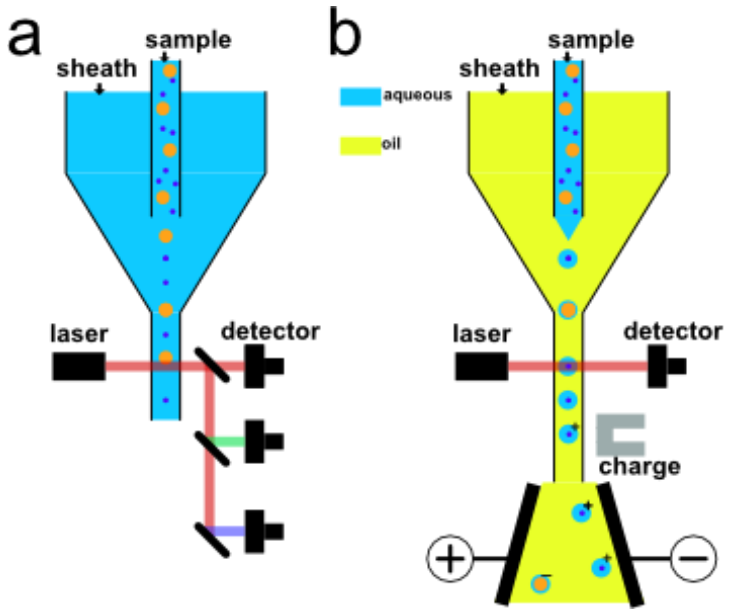

Fig. 1.1: Schematics of common flow cytometry: (a) cell detection; (b) cell detection and sorting.

1.1.1. Optical flow cytometry

The optical flow cytometry is the most commonly used method in commercial flow cytometry for detecting cells or particles through fluorescence[3]. The traditional optical flow cytometry

consists of three parts, the optical path, microfluidic device and the data processing system. To ensure cells or particles can be irradiated by the exciting light, the microfluidic device of optical flow cytometry should supply a good focusing ability to make cells and particles move through the optical path[4].

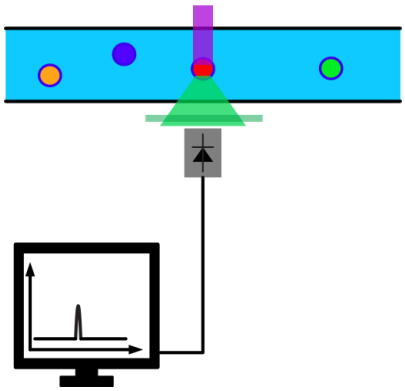

Fig. 1.2: Schematics of optical flow cytometry

Comparing to other flow cytometries shown in Fig.1.2, the optical flow cytometry has simpler channel and data processing, only including active light sours, filter and photodetector. However, the main challenge is the requirements of fluorescence-based labeling ,which may pose some biochemical issues to cells[5].

1.1.2. Imaging flow cytometry

Among all kinds of flow cytometries, imaging flow cytometry (IFC) can provide much more information and directly detect the morphological characteristics of cells[6], such as intercellular components analysis by fluorescence imaging[7], [8], Raman spectrum[9]; and visualization of 3D structure shapes of cells by tomographic imaging[10], light sheet scanning[11], [12] or rotating cells[13]. Fig.1.3 shows the common structure of imaging flow cytometry, incident light irradiates and pass the object, collected by the camera or other photo-detect device to generate the intensity-related[14], [15] or fluorescence-related[8], [16] image. The throughput of imaging flow

cytometry relates to many factors like frame rate of camera, data transfer and field of view (FOV); and the velocity, focusing, and concentration of particles or cells in sample fluids. This makes the throughput of IFC quite easier to improve; for example, imaging with multi-channels[17], [18] or wide channels[19] simultaneously with a large FOV.

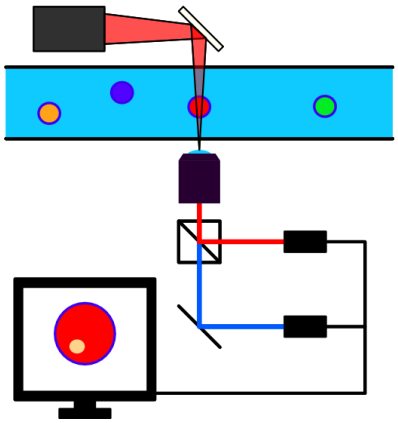

Fig. 1.3: Schematics of imaging flow cytometry

However, more information from imaging means more data will be generated during imaging process, which require powerful data-handling or data-compressing[20], [21]. Moreover, the components of imaging flow cytometry are always much more expensive[22].

1.1.3. Impedance flow cytometry

Impedance cytometry is a label-free method to carry out cell detection and analysis based on impedance spectroscopy[23] which widely used in cells analysis[24], food security[25], protein detection[26] and drug resistance[27] for the advantages like precision and efficient. With a low detection frequency (< 1 MHz), It can easily measure the size[28], [29], amount[30], [31], shape[32], phenotypes[33], and position[31], [34], [35] of cells. Additionally, by applying high-frequency detection voltage (> 1 MHz), cell membrane could be partly conductive[36], [37], some intracellular components[38] and property[39] could be detected from micro to nano scale[40],

[41]. With some constrict channel, cell deformation[42] can also be monitored. As shown in Fig.1.4, three electrodes are set on the bottom of microchannel, AC voltage is applied in the middle electrode while the two sides are connected for the data-collection; cell or particle passing through the detection area change the local resistance and generate the voltage signals. The fabrication of microfluidic chip for impedance flow cytometry is usually more complex than other flow cytometry as the electrodes are always assembled on the chip, like lithograph-based coplanar electrodes[43], [44] and liquid metal-based 3-D electrodes[45], [46]. Unlike the imaging flow cytometry, impedance flow cytometry output the one-dimensional data, which requires some data processing to extract the relevant information, this limitation affects the detection accuracy of impedance flow cytometry. Therefore, stable conditions during detection are necessary to meet the demands of impedance flow cytometry.

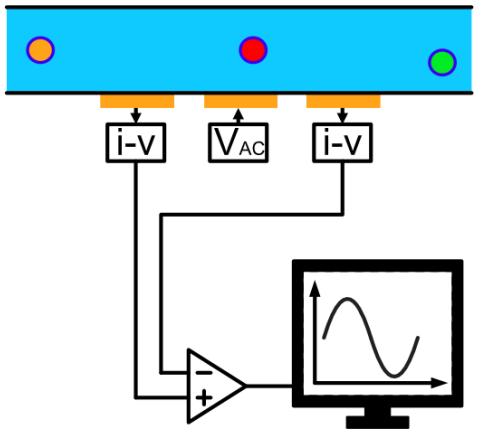

Fig. 1.4: Schematics of imaging flow cytometry

1.2. Cell focusing in microfluidic chip

In flow cytometry, as each sensor exhibits varying sensitivity in different areas, achieving equilibrium positions for cells or particles is crucial for accurate detection[47]; the technologies

to drive cells moving with the similar trajectories is called cell focusing. A stable positioning of the target enhances detection sensitivity and accuracy[48]. For example, cells can be imaged clearly only when they are near the optical focal plane of the microscopy system, and the imaging quality is further improved when cells are focused in the center of the field of view (FOV)[22]. In impedance cytometry, cell near the electrodes can generate signals with higher amplitude[30], [46]. Moreover, focusing can also help to organize the particles or cells, separate objects for precise measurement[49]. To maintain the target flow at a stable location in the cross-section of channel, the cell focusing should be considered in design. Most cell focusing methods can be sorted into two groups, the passive cell focusing and active cell focusing[50].

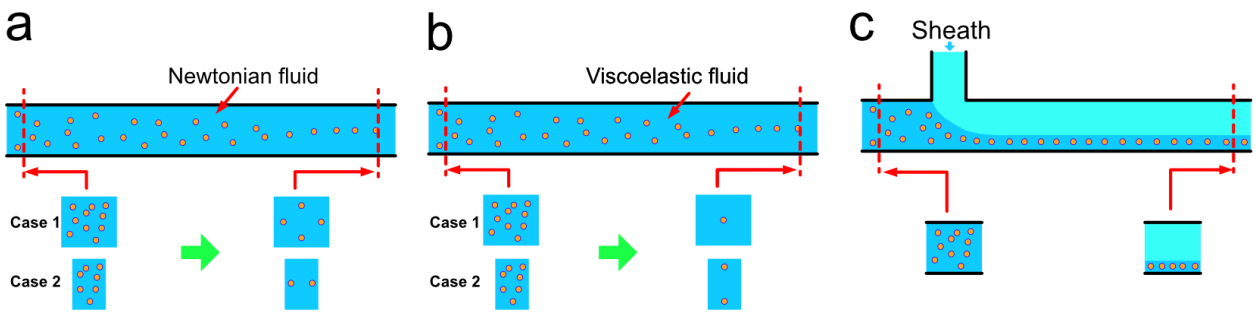

Fig. 1.5: Three common passive cell focusing methods, A-A and B-B represent the cross-section at initial and end of channel; (a) inertial focusing, four equilibrium positions for square cross-section (case 1) and two equilibrium positions near long boundaries for rectangle cross-section (case 2); (b) viscoelastic focusing, one equilibrium position for square cross-section (case 1) and two equilibrium positions near short boundaries for rectangle cross-section (case 2); (c) hydrodynamic focusing, sheath press sample flow to a concentrated distribution area.

1.2.1. Passive focusing

The passive cell focusing method is the simplest approach to achieve cell focusing in microfluidics. Without any external influences, cells or particles in a solution can be driven to a small range solely through the hydrodynamic effects of the flow[51]. The most common passive focusing method is inertial focusing[52], like Fig.1.5a shows. As particles or cells flow along the channel, two inertial forces come into play: the shear-gradient lift force and the wall-induced lift

force[53]; These forces act in opposite directions on the cell[54], and drive it to an equilibrium position where the forces balance each other. Due to the simple principle, inertial focusing is widely used in various flow cytometry[55]. However, the inertial effect is relatively weak compared to the hydrodynamic force, which necessitates longer channels. To overcome this limitation, enhancements such as stepped channel[56], [57], serpentine channel[58]–[60] have been developed to enhance the inertial focusing. Additionally, replacing the standard Newtonian fluid with a viscoelastic fluid can enhance the performance of inertial focusing by reducing the number of equilibrium positions within the channel cross-section[61]–[63], like shown in Fig.1.5b. For example, while a channel with a square cross-section has four equilibrium positions with inertial focusing, the use of a viscoelastic fluid reduces it to one equilibrium position[64]. However, even with these improvements, the performance of inertial focusing at high velocities or high Reynolds numbers remains suboptimal[65], [66], which limits its applications.

Like Fig.1.5c shows, to achieve efficient focusing from the sample inlet to the detection area, the properties of laminar flow can be utilized through hydrodynamic focusing. By incorporating branch channels, sheath flows can surround[67] or compress[68], [69] the sample flow, directing the sample to the desired area within the cross-section, such as the vicinity of the electrodes in impedance flow cytometry[70]. In comparison to inertial focusing, hydrodynamic focusing can achieve effective focusing even at high velocities or Reynolds numbers[71].

1.2.2. Active focusing

Active cell focusing methods involve the use of external physical fields to manipulate cells or particles in microchannels, such as electric field[72] or acoustic field[73], [74]. These external fields can exert additional forces on cells, such as dielectrophoresis (DEP) force[75] and acoustic

radiation force[76], [77]. The advantage of active sorting is its rapid response speed, as cells or particles can be immediately affected by the forces upon entering the external physical field. However, active cell focusing methods require additional design or assistance, which increases the complexity of chip fabrication and usage.

1.3. Droplet microfluidics

Droplet microfluidics has been developed as a powerful tool in chemical and biological analysis[78]. Unlike conventional single-phase microfluidics, droplet microfluidics enables the division of samples into small droplets, serving as research units and improving cost-effectiveness[79]. These droplets can be considered as closed volumes, creating mini cell culture environments[80]–[82] or small-scale chemical reaction unit[83], like Fig.1.3a shows. Furthermore, due to their controllable size, droplets can be utilized as substitutes for certain cell manipulations[84] (Fig.1.3b). For example, in commercial flow cytometry, droplets act as carriers for cells, allowing for cell sorting by manipulating the target cells within the droplets[85]; Some transfection methods involve encapsulating cells in droplets with reagents to facilitate intracellular delivery[86]. Additionally, like shown in Fig.1.3c, droplet microfluidics finds extensive applications in polymerase chain reaction (PCR) analysis[87], [88].

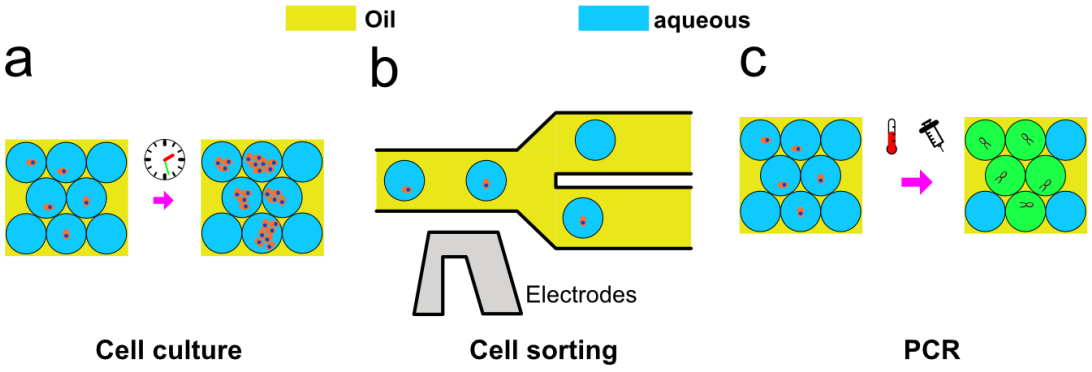

Fig. 1.6: Applications of droplet; (a) cell culture; (b) cell sorting; (c) PCR analysis; the yellow color and blue represents the oil phase and aqueous phase, respectively.

1.4. Aims and outline

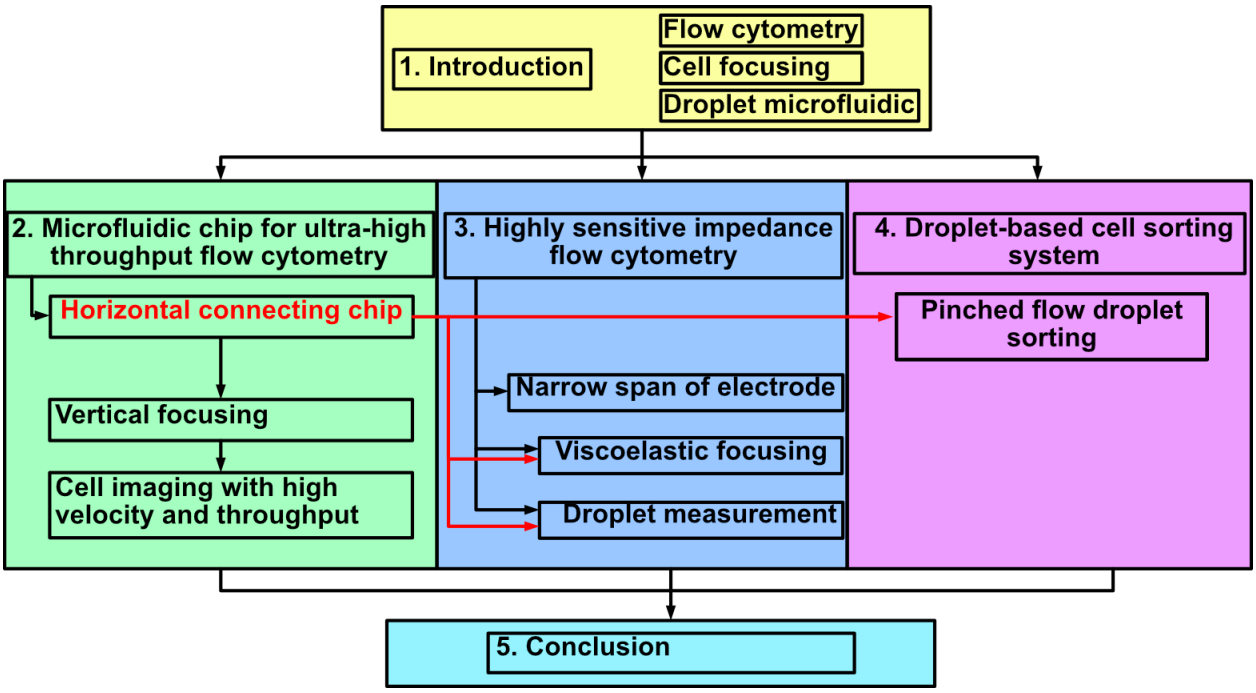

Fig. 1.7: Outline diagram of the dissertation

Microfluidic chips play a crucial role in various types of flow cytometry as they provide a stable environment for cells during other physical or biochemical detections. Sensitivity and throughput are two key parameters that reflect the capability and efficiency of any flow cytometry system.

In this dissertation, my focus is to improve the throughput and sensitivity of flow cytometry. Firstly, I enhance the throughput by developing a novel microfluidic chip structure that enables higher velocity and pressure, allowing for the detection of a large number of samples in a shorter time. For instance, the microfluidic chip designed with this structure can facilitate velocities up to 40 m/s, which is currently the fastest achievable for optofluidic time-stretch (OTS) microscopy, resulting in a minimum throughput of 2,700,000 cells/s. To improve sensitivity, the microfluidic chip is designed based on the principles and requirements of flow cytometry. For example, cell

focusing is implemented in both imaging flow cytometry and impedance flow cytometry to ensure a stable cell position relative to the optical focal plane and coplanar electrodes, respectively. In the impedance flow cytometry, the integration of electrodes on the microfluidic chip allows for accurate detection with narrow electrode spacing or wider positive electrodes, thereby achieving precise measurements.

In addition to flow cytometry for cells, this dissertation also explores droplet measurement and sorting. The objective is to develop a droplet-based cell sorting system, which requires investigating nondestructive methods for droplet measurement. Furthermore, there is a need to design a passive droplet sorting system capable of effectively separating two types of droplets with a small difference in diameter.

The details of each purpose and the related research will be described in each chapter in this dissertation, including five chapters:

Chapter 1: Introduction

This chapter provides an introduction to the background of common flow cytometry, including its basic principles and applications. It discusses the fundamental principles underlying flow cytometry and explores its various applications in different fields. Additionally, the chapter focuses on specific aspects related to the research, such as cell focusing techniques and droplet microfluidics. It presents an overview of current research efforts and evaluations conducted in these areas, most flow cytometries have the demands of higher sensitivity and throughput. The aim of this chapter is to establish the research purpose of the dissertation, which is to enhance the sensitivity and throughput of common flow cytometry by optimizing the design and structure of

microfluidic chips. Moreover, the intention is to explore further applications of flow cytometry beyond its conventional use.

Chapter 2: Microfluidic chip for ultra-high throughput flow cytometry

This chapter focuses on providing a microfluidic chip for optofluidic time-stretch (OTS) microscopy, which is known for its high-speed imaging capabilities. While OTS microscopy claims to be capable of imaging cells moving at 60 m/s[89], its practical use has been limited to imaging cells at speeds of only 1 m/s with common PDMS chips[90] and 25 m/s with whole-glass chips[91]. To address this limitation and offer a powerful and cost-effective solution, I have designed a minimized glass-PDMS-glass microfluidic chip with horizontal connections specifically for imaging cytometry. my chip design focuses on ensuring muscular strength and minimizing layouts, allowing for ultra-high velocities achievable with common syringe pumps. By utilizing hydrodynamic focusing with two sheath flows at high velocities, I can concentrate most samples near the focal plane of the optical system, thereby enhancing the sensitivity of OTS microscopy. Through the implementation of my microfluidic chip in the OTS microscopy system, I have successfully achieved cell imaging at a speed of 40 m/s, which, to the best of my knowledge, is the highest speed achieved in imaging flow cytometry[92].

Chapter 3: Highly sensitive impedance flow cytometry

Chapter 3 focuses on the development of a new microfluidic chip structure that enables extremely high throughput in imaging flow cytometry. This innovative structure is applicable not only to various microfluidic devices used in flow cytometry but also to impedance flow cytometry. The main objective of this chapter is to enhance the sensitivity of impedance flow cytometry for cell

detection and droplet measurement. The sensitivity of impedance flow cytometry is influenced by several factors, including the distribution of the electric field, the position of objects being detected, and the layout of electrodes. This chapter presents three research studies. The first study explores the utilization of narrow-span electrodes with a width of 1 μm to enhance the strength of the electric field, resulting in larger amplitude impedance signals [93]; The second study investigates the use of viscoelastic focusing to achieve a stable cell position in the microchannel, minimizing errors caused by variations in the distance between cells and electrodes. The third study examines how the electrode layout affects impedance detection of droplets. The size of the electrodes and droplets can generate four different results in the differential signals of impedance detection, and this research aims to investigate this relationship. Overall, Chapter 3 contributes to improving the sensitivity of impedance flow cytometry for cell detection and droplet measurement by addressing various factors and introducing innovative approaches.

Chapter 4: Passive size-based droplet sorting

In Chapter 4, a novel concept of a droplet-based cell sorting system is introduced. This system utilizes a pulse laser to selectively target and burst undesired droplets, leaving behind the intact droplets containing the desired cells. The remaining intact droplets, along with small droplets, are then separated using a passive droplet sorting structure. To achieve passive droplet sorting, the principle of pinched flow is investigated through numerical analysis, which guides the design of the sorting channel. By implementing this passive cell sorting channel, successful separation of droplets with diameters larger than 110 μm and smaller than 100 μm is achieved, with each group directed to different outlets. Chapter 4 establishes a new approach to droplet-based cell sorting,

combining laser-based selection with passive sorting, and demonstrates its effectiveness in separating droplets based on size.

Chapter 5: Conclusion

This chapter conclude the works and achievements in this dissertation, and presents the further work in the future.

2. Microfluidic chip for ultra-high throughput flow cytometry

2.1. The optofluidic time-stretch (OTS) microscopy

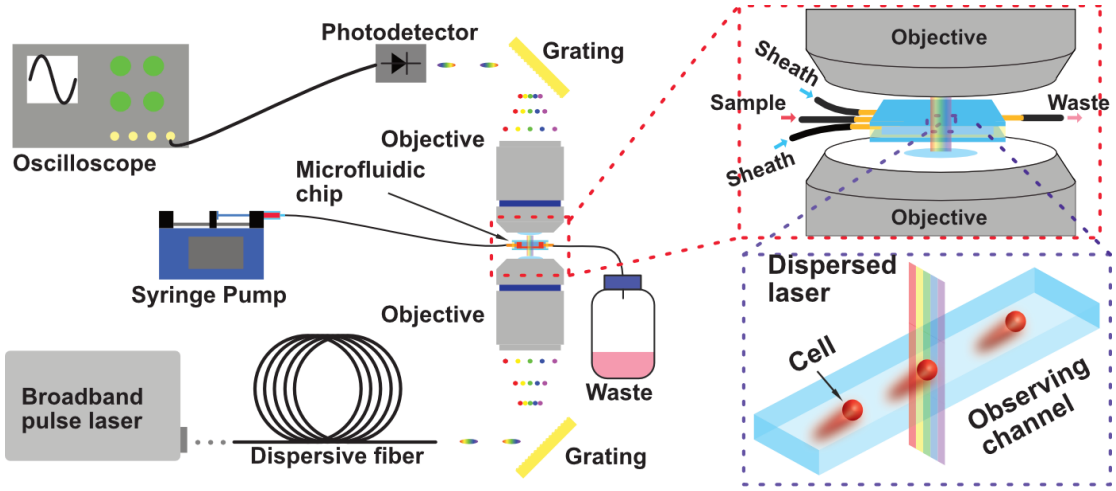

Fig. 2.1: Schematics of the optofluidic time-stretch (OTS) microscopy.

For most IFC, the high velocity of cells can enhance the efficiency and throughput of detection, but high velocity of moving objects means lower exposure time of camera. The optofluidic time-stretch (OTS) microscopy is current the fastest imaging flow cytometry (IFC), which can realize blur-free bright-field imaging at a frame rate of 10 million fps[94] and overcome the trade-off between spatial resolution and throughput[95]. Fig. 2.1 shows the basic optofluidic time-stretch microscopy for cell imaging. Laser pulses from a broadband laser are first dispersed in the time domain by a long dispersive fiber and then dispersed in space by grating. Afterwards, the pulses are focused on cells that are flowing through the microchannels. By an inverse optical path, time dispersive lasers with information of objects are generated and detected by a photodetector. In this process, laser pulse will be firstly stretched into wide wave by long fiber on time-scale and dispersed spatially by grating, the spatial dispersion light will irradiate on cell and the intensity of some position will be changed; by comparing with the waveform of laser pulse before and after

irradiation, every pulse can transfer to one-dimensional image; and cell images could be composited by these one-dimensional images from every pulse, like shown in Fig.2.2a. With this powerful ability, OTS microscopy is claimed to image a moving object at a velocity of 60 m/s[89] which is evaluated with imaging resolution and sampling principle (one pixel require at least two pulses). However, in practical applications, the microfluidic chips could not provide a stable velocity high enough in such a condition. To improve the throughput of IFC, velocity in microfluidic chips needs to approach the allowing velocity of imaging system, like OTS microscopy.

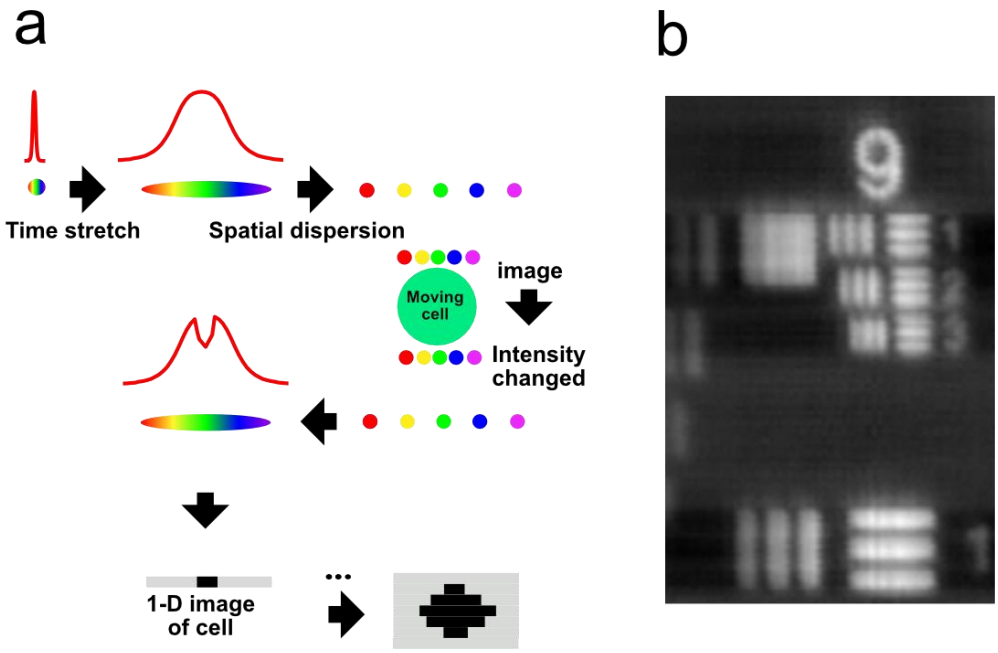

Fig. 2.2: (a) Process from laser pulses to image; (b) OTS image of the USAF-1951 resolution chart.

In these experiments, the OTS microscopy is based on the femtosecond laser (Ti: Sapphire crystal) with a center wavelength of 800 nm, a 3dB bandwidth of 40 nm, and a repetition rate of 80 MHz. The pulse is stretched by the 1.55km single-mode fiber with the dispersion parameter of 186 ps/ (nm km). The stretched pulse is spatially dispersed by the diffraction grating with a groove density of 600 lines/mm, and the sampling rate is set as 10GS/s for 40 μm wide FOV and 40GS/s

for 100 μm wide FOV (spot size is 100 μm also), which is enough for this system without valid information loss and is also helpful for enormous cell data statistics. The NA of the objective is 0.65. Fig.2.2b shows the images of the USAF-1951 resolution chart, and the line pairs of group 9 element 3 of the USAF-1951 resolution chart can be identified in the image. This indicates that the OTS system used for testing has a spatial resolution of ~780 nm, which is consistent with the theoretical calculation[96].

2.2. The PDMS-based microfluidic chip with horizontal connections

2.2.1. The microfluidic chip with high throughput

High flow velocity means high pressure in enclosed microchannels, leading to many unpleasant consequences. High pressure is harmful in microfluidics; for example, it could easily cause leakage and channel deformation, resulting in lower actual flow rates and even chip damage. The most common PDMS-Glass chip devices for OTS imaging can reach a fastest velocity of 10 m/s[97]. To get higher pressure or velocity in microfluidic chips, some more solid materials like metal stainless steel[98], [99], silicon[100], and glass[101] were used. For optical microscopy, glass is a perfect material due to its good optical and mechanical performance[102]; a 1.4 mm thickness glass chip was fabricated to keep low deformation of channels in higher pressure conditions, to drive fluids at a velocity as high as 25 m/s[91]. But the disadvantages of solid chips are quite evident, as complex fabrication processes, using dangerous toxic reagents and multiple equipment[103], special jigs[104], and experienced operators are all required[105]. To realize a

higher velocity in normal PDMS microfluid devices which are simple and inexpensive, optimization of current microfluidic design is required.

In a microchannel, pressure from inlets overcomes the hydraulic resistance and drives liquid flow. The hydraulic resistance is similar to resistance in electric circuit which is in direct proportion to the channel length and inversely proportional to the cross-section of microchannels[106]. Therefore, decreasing hydraulic resistance could be a method to achieve my purpose. Many parameters could be optimized, like the length and cross-section of channels[107], and angles of narrow channels[108]. In OTS microscopy and other imaging system, chips are always limited to the space between objectives[94], and very long channels are always designed to avoid interference from inlets and lenses. Since the inlets could be set horizontally (parallel to microchannels) from the side of the chips to avoid interference[109], chips could be minified by decreasing the length of the useless channels.

However, only high velocity could not satisfy the demand from OTS cytometry. OTS microscopy has a very small focal range, which means the imaging of cells and particles is quite sensitive to the distance to the focal plane in microchannels. The common used microfluidic chip use hydrodynamic focusing with 30 μm height of whole channel, this channel can work at 1 m/s to 10 m/s; however, this single layer can only horizontally focus cells in middle channel and fail to realize vertical focusing[71], [110]. For example, Fig.2.3a shows the OTS images of blood cell without cell focusing, the four cells in this image are the same kind but two in focus and two out of focus, the cells out of focus will have the blur interface and will have large size which is image distortion. The Fig.2.3b and Fig.2.3c shows the OTS images of cells on focal plane and 10 μm far from the focal plane, only 10 μm can make image quality such poor which means the OTS imaging is very sensitive to the cell position. So microfluidic chip should be able to focus cells vertically

at a high velocity. Sheath assisted hydrodynamic focusing is the most simple and direct way to realize 3D focusing[47]. By tandemly arranging inlets of sheath and sample fluids in a straight microchannels, the sheath could push sample to top or bottom of the channel for vertical focusing[68], [69]. But two inlets on one channel make it hard to set horizontal connections to shorter channels. Another kind of vertical hydrodynamic focusing is achieved in multi-layer T[111] or Y[112] shaped channels, where sample channel has a lower height than sheath channels[113]; and vertical focusing could be realized by increasing velocity or Reynolds number[114]. Additionally, the inertial effects in fluid are pretty strong at high velocities, which could affect the focusing of cells in the microchannels[54], leading to a result like cells separation[115], [116] but unstable. Even worse, inertial focusing always demands a long channel[117], which keeps a high flow resistance limiting to a higher velocity.

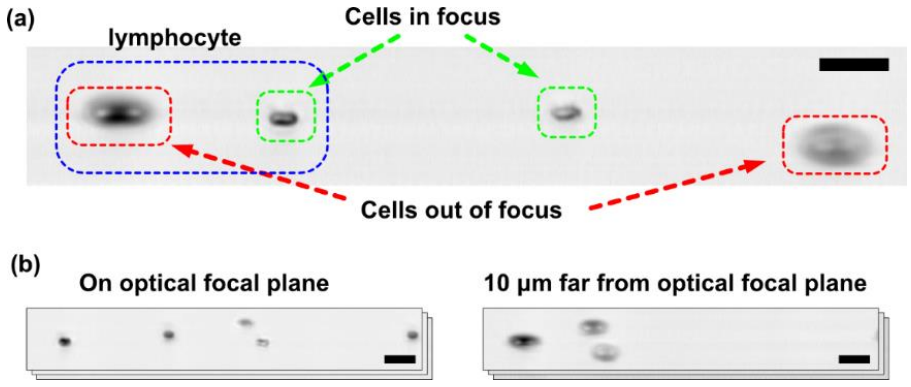

Fig. 2.3: The OTS images of cell on focal and out of focal: (a) OTS images of cells, scale bar: 20 μm; (b) OTS images of cells on focal; OTS images of cells out of focal, scale bar: 20 μm.

2.2.2. The microfluidic chip with horizontal connections

Among PDMS-based microfluidic devices, the microchannel deforms easily under high pressure due to the soft PDMS which can cause the damage of sealing and results in leakage. Nevertheless, if the leakage problem can be controlled, the PDMS would still be the best material

for microfluidic chip because of the easy-fabrication and cost-efficiency. To avoid the leakage, the sealing of connections and PDMS should be stronger enough to resist the deformation of PDMS. Except using solid material to direct limit, the deformation in channel, the structure of microfluidic chip can be optimized instead of just using solid material which make increase the difficulties of fabrication. There are two reasons leading the leakage on PDMS chip; the first is the deformation of PMDS surface which make the relative movement between PDMS and sealing, and the second is the weak adhesion between PDMS and sealing (resin). Here, a new structure of microfluidic chip is created which can enhance the sealing and prevent the leakage; as the leakage problem can be avoided, we still choose the PDMS as the main material of chip.

In OTS microscopy system, microfluidic chip support cells with fast and stable movement. In most microfluidic chips, especially for imaging flow cytometry, most inlets and outlets are vertically inserted into chips, connecting pipelines and micro channels[117], like shown in Fig.2.4a. This kind of connection is quite simple and easy to use. However, some optical components need enough space near the microfluidic chip for imaging flow cytometry. For OTS microscopy, the space is very narrow, limiting the thickness of the microfluidic chip. Figs.2.4b shows the horizontally connecting chip which has no interference with objectives, and makes chips free to move for unlimited observation; while chip with vertical connections is limited by the arrangement of objectives and connections, and chip could only be adjusted in a small range determined by the distance of connections and the diameter of objectives.

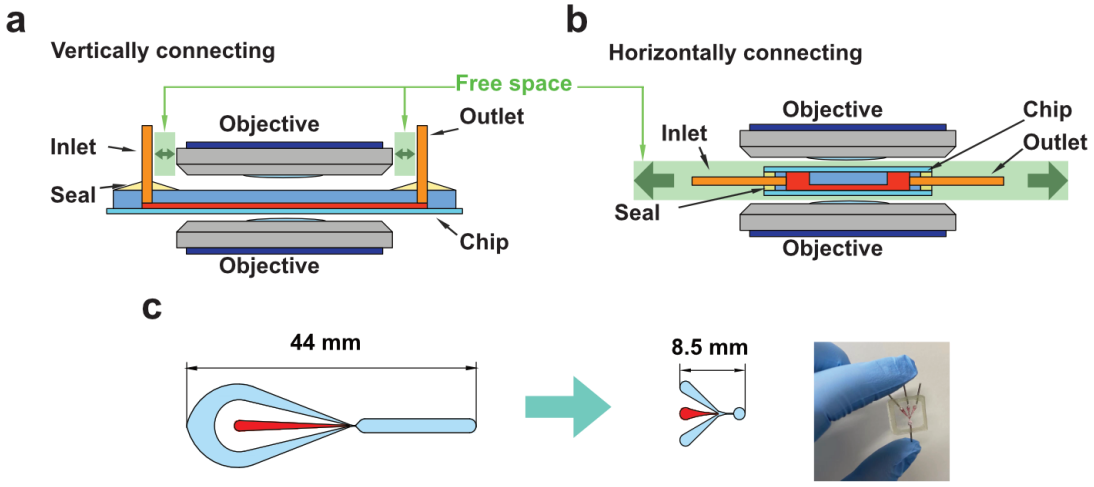

Fig. 2.4: The sketching of chips with horizontal connections (b) and vertical connections (a) locate between two objectives in OTS microscopy; the green area presents the free space the chip could move; (c) The channel design of vertical connecting chip and horizontal connecting chip, the horizontal connecting chip allows the minimization design.

In most microfluidic chips, the function is always realized by a very small part, while the most length of channels is redundant. In Fig.2.4a-b, the chip with horizontal connections is smaller than the chip with vertical connections, because there will be no demand for long channel to ensure the space for objectives. Therefore, the chip can be designed much smaller without concerning the interference of connections and objectives. In my design, most length of the microchannel of vertically connecting chip is optimized, and the narrow observation channel is directly linked with outlets. As shown in Fig.2.4c, the length of the channel is cut from 44 mm with vertical connection to 8.5 mm with horizontal connections. The shorter channel has a low flow resistance, allowing a higher velocity driven by the same pressure. With this structure, the flow can be driven at high velocity, and the PDMS will surround with solid material like glass and resin; the sealing of resin attaching on glass is quite strong, preventing chip from leakage.

2.2.3. Fabrication of horizontal connecting microfluidic chip

Horizontal connections of pipeline and micro channels had been realized in a whole glass microfluidic chip[109], where the holes are directly drilled from the sides toward microchannels by a drilling machine. But this method is easy to cause microchannel contamination and has high requirements in machining equipment. To fabricate the horizontally connecting chip with normal PDMS-glass structure, an eclectic way to reach a similar result is to connect pipeline with a larger storage chamber that connects micro channels. Same like inlets, waste also flows into waste chamber and moves out through horizontal outlets. To drive the higher velocity, microfluidic chip needs to tolerate extreme high pressure, even though the horizontal connection could help to reduce pressure and structure deformation. Some defects in common chips should also be considered, like weak sealing of glue with low surface energy materials like PDMS and PEEK. It's worth noting that normal soft lithograph processes are used in my fabrication, without any requirements for special equipment or techniques.

The fabrication of PDMS-based horizontal connecting microfluidic chip contains the processes below:

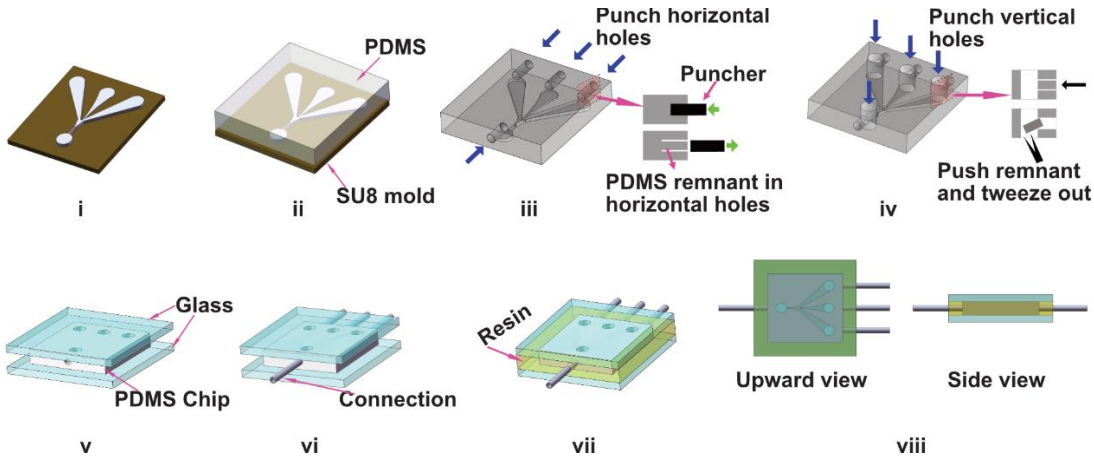

Fig. 2.5: The fabrication steps of PDMS-based horizontal connecting microfluidic chip.

Step i: Prepare the chip mould, the mould can be fabricated by ordinary lithography (spinning coating, baking, exposure and development) with negative photoresist SU-8;

Step ii: Pour the mixed PDMS (ratio of PDMS and curing agent is 10:1) over mould, and place it in a thermostatic drying oven at 80 ℃ for 6 hours for solidification;

Step iii: Cut and peel the PDMS structure with microchannel from mould, and press puncher from side of PDMS structure to generated the inwalls of horizontal holes. no hole generated in this step, and only PDMS is carved for holes of connection;

Step iv: Punch holes vertically at the locations of inlets and outlets by punchers, to create chambers to link connections with channels, these chambers will be enclosed as storage chambers. The cutting parts of PDMS in the last step are now cleaved, and the holes for horizontal connections are fabricated, but the remnant is stuck in horizontal holes. A small tip is used to push the remnant from the side of the connection holes toward the chamber and take the remnant out from the chamber holes. The vertical hole can act as the bridge to link the connections with the microchannel, the vertical hole will be closed by bonding with two glass and generate the chamber;

Step v: To assemble the chip, two glasses are bonded with PDMS to close vertical holes as enclosed storage chambers by plasma cleaner at 75 w, 40mTorr for 60 seconds;

Step vi: Stainless steel capillary tubes are inserted as connections, instead of common PEEK tubes. Steel capillary tubes have the advantages like strong strength, thin wall, low cost, and high surface energy[118], [119], which exhibit excellent adhesiveness with resin;

Step vii: Use epoxy glue (a kind of AB glue) to fulfilled into the interval of two glasses, and wait 12 hours for solidification.

Additionally, to avoid leakage from pipeline, I use PTFE pipeline to connect chip and syringe, with small inner diameter of PTFE pipeline (22S) and larger outer dimeter of stainless-steel

connections (21G) to achieve interference fit; the interference fit of the two hard materials can tolerate high pressure without sealing. PTFE has a good strength to tolerate deformation under high pressure, and also has low coefficient of friction to decrease pressure loss during fluid transport.

2.3. The effects of high velocity on sample focusing and wall-deformation

2.3.1. Simulations of hydrodynamic focusing at different velocity

In imaging cytometry, only cells flowing near the optical focal plane can be clearly imaged. Unfocused cells can lead to blurry imaging and even out of detection. Therefore, microchannels for imaging cytometry should be able to focus cells onto the optical focal plane. Hydrodynamic focusing with sheath fluids is the one of the simplest focusing method[120] and is compatible with most of imaging systems. As mentioned before, the conventional vertical focusing structure, which place vertical focusing inlets behind sample inlets, is difficult to integrate with a horizontal connecting structure. Therefore, I designed a two-layer microchannel with a lower height for sample channel and higher height for sheath channels. This design aims to maximize the flow of cells on the optical focal plane. In the design shown in Fig.2.6a, the two-layer microchannel includes a 30 μm high sample channel, which is less than half of the other layer or channel (70 μm in height), making the samples flow in the bottom half of the channel. To investigate the effects of velocity on the focusing of the sample near the bottom of the microchannel, FEM models are built by a commercial software, COMSOL Multiphysics (COMSOL Inc., Burlington, MA, USA). Additionally, the microchannel is simplified into the junction and observation channels for more efficient calculation, because all focusing processes happen there. The junction is a triangle shaped

channel that is 1mm long, 700 μm wide, and 70 μm high, while the long narrow observation channel is 1mm long, 100 μm wide, and 70 μm high.

The simulation can be directly carried by solve the Navier–Stokes equations:

$$\rho\left(\frac{\partial \mathbf{u}}{\partial t} + \mathbf{u}\cdot\nabla\mathbf{u}\right) = \nabla\cdot\left[-\mathrm{p}\mathbf{I} + \mu\left(\nabla\mathbf{u} + \nabla\mathbf{u}^{\mathrm{T}}\right)\right]$$

$$-\nabla\cdot\mathbf{u} = 0 \qquad \text{(Eq.2.1)}$$

where t denotes time; ρ is the fluid density; μ is the dynamic viscosity of the fluid; **u** is the fluid velocity; p is the pressure; **I** is the unitary tensor; The distribution of the sample flow can be traced by streamline method or the mass diffusion. The diffusion can be simulated with the module of transport of diluted species, and couple the Eq.2.1 with the mass balance equation:

$$\nabla\cdot\mathbf{J} + \mathbf{u}\cdot\nabla c = R$$

$$\mathbf{J} = -D\nabla c \qquad \text{(Eq.2.2)}$$

where the **J** represent the mass flux diffusive flux vector; **u** is the fluid velocity which is same as in Eq.2.1; *R* is reaction rate expression for species; *D* denotes the diffusion coefficient; c is the concentration of the species, the unit of concentration in mass diffusion is mol/m^3. As the mass diffusion is just for trace the sample distribution, the diffusion coefficient (*D*) is set as a value small enough but larger than 0;

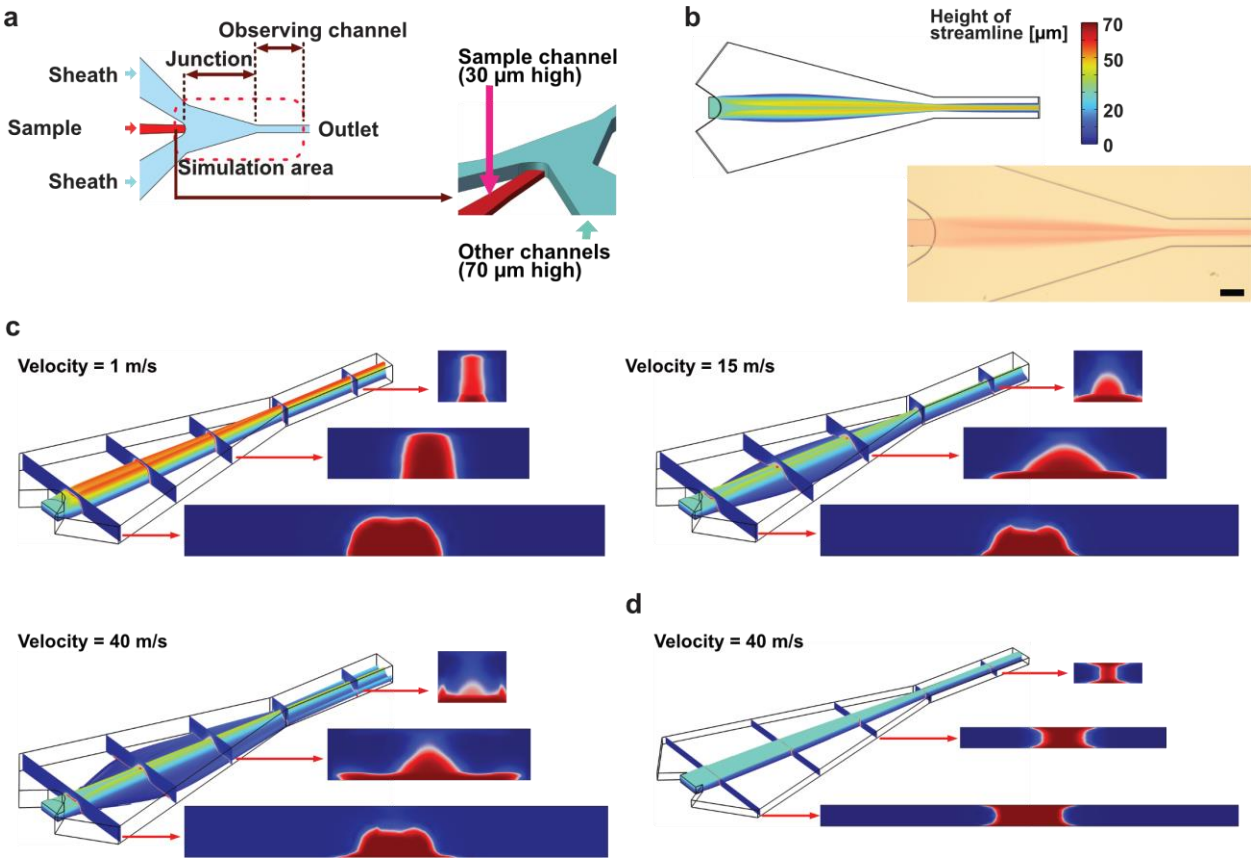

Fig. 2.6: Simulation of sample fluid distribution at the focusing junction; (a) Main structure of my microchannel design, two layers are highlighted with different colours, sample channel (red) has a height of 30 µm, while other channels (Pale cerulean) are 70 µm high; (b) Simulation was carried at the junction and observation channels, where all processes of focusing happen. Colour bar represents the height of the sample; and the experiment result of red ink in the junction at 5 m/s is shown, which agrees with the simulation result; (c) Sample distribution in the channel and its streamline in the two-layer channel at different velocities of 1 m/s, 15 m/s, and 40 m/s; (d) Simulation of single layer channel at 40 m/s.

Fig.2.6b top shows the simulation result obtained at the flow velocity of 5 m/s. To verify the simulation model, an experimental image (below) achieved at the same flow condition (total flow rate is 2.1 mL/min with a 2:2:1 ratio of sheath and sample fluids) is shown at the bottom. In the experimental image, a red ink trail was clearly observed, which matches the shape (profile) of the sample fluid in the simulation. The intensity of red color of red ink trail also matches the color of streamline in the simulation, which represents the height of sample fluid. Further simulations were

carried out by turning flow velocity from 1m/s to 40 m/s with a certain ratio of flow rates between sheath and sample fluids. The simulation results obtained from three different flow velocities are shown in Fig.2.6c; each small image contains a main image of streamlines and three graphs of cross-sectional view at different positions of the channel. I found that sample fluid is pinched to center and spread from top to bottom of the channel at 1 m/s, while it spreads in the horizontal direction to the bottom side of the channel at 40 m/s. This result indicated that higher velocity of sheath fluid can lead high inertial effects which enabled the spreading of sample fluid at the bottom of the channel. The proposed two-layer design of the channel offers a narrow focal plane and thus a better focusing performance that increased with flow velocity. Additionally, the simulation of single layer channel is also carried which is shown in Fig.2.6d, in single layer channel, the compression from the sheath is symmetry toward up and down sides, results in sample tends to distributed near the bottom and top. However, the optical focal plane only has one height in channel, the two-sides distribution can make half cells out of imaged; moreover, the small cross-section can always increase the flow resistance which obstruct the efforts for higher velocity.

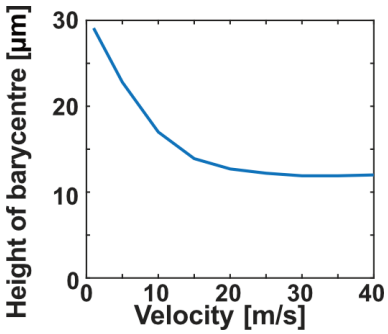

Fig. 2.7: Height of barycenter of the sample at velocities ranging from 1 to 40 m/s.

As velocity is a quite important parameter which affects hydrodynamic focusing of particles to the focal plane, I trace the samples at different velocities. Barycenter positions which could be used to evaluate fluid distributions[121] are calculated here to evaluate how samples are focused

to the focal plane. Fig.2.7 shows the height of the barycenter of the sample at different velocities. The barycenter of the sample is located in 30 μm height area near the bottom of the microchannel at 1 m/s, and becomes closer to channel bottom as velocity increases. Since velocity reaches 15 m/s, the height of barycenter keeps about 12 μm. This result indicates that sample fluid can be focused to the bottom of channel with a 12 μm wide distribution, which is similar to the cell size.

2.3.2. Investigation of flow velocity effects on vertical hydrodynamic focusing

Reynolds number (Re) is one of the essential dimensionless parameters to explain fluid mechanisms in previous studies. Since the density, the viscosity of the fluid, and the dimensions of the channels are constant in all experiments of my research, I directly employed flow velocity as the main indicator to describe my results instead of Reynolds number. In hydrodynamic focusing, velocity and the ratio of sample and sheath are two important parameters. However, in conditions of high velocity, a low ratio of sample and sheath can cause the sample to focus towards the corners, thereby weakening the vertical focusing effect. To mitigate this issue and ensure effective vertical focusing, I have set the ratio of sample and sheath as 1:4 (specifically, 1:2:2 for the sample and two sheath fluids) to avoid corner focusing under high-velocity conditions. Although the Reynolds number (about 4,000) is much larger than 2,000 at high velocity, but the turbulence is not occurred; the flow situation may between the laminar flow and turbulence.

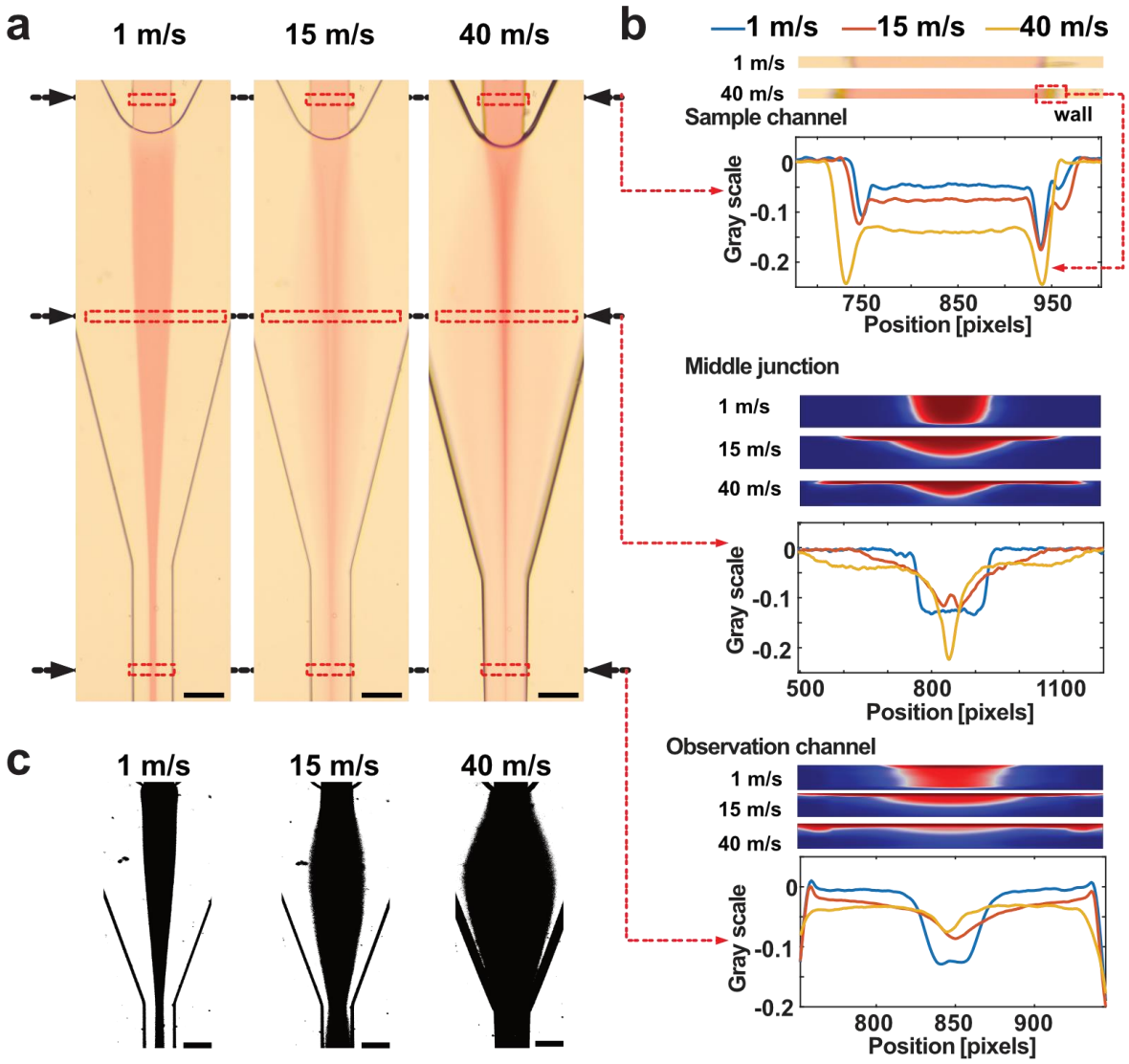

Figure 2.8: The analysis of sample distribution in hydrodynamic focusing. (a) Photos of the junction of channel at different velocities of 1 m/s, 15 m/s, and 40 m/s from left to right, scale bar represents 100 μm; (b) Grayscale of red ink at three positions of sample channel (up), middle junction (middle), and end observation channel (down), the obvious drops of grayscale in sample channel represent the channel wall, and some results of simulation mentioned in section 2.3.1 are added here for compare; (c) The binarization of the middle junction at the velocities of 1 m/s, 15 m/s and 40 m/s from left to right, scale bar represents 100 μm;

We performed experiments to investigate the effects of flow velocity on vertical hydrodynamic focusing. To trace the sample flow in hydrodynamic focusing, red ink is the most cost-efficiency method. As shown in Fig.2.8a, red ink trace from the sample channel is first pinched, focused and

pressed to a relatively thin stream and finally moved to the bottom side of the observation channel. The ink distribution and the color depth in Fig.2.8b are well matched to the simulation results shown in Fig.2.6c. The ink shows different color depths along the flow direction at different velocities. To evaluate the sample distributions along channel height, I convert the images in Fig.2.8a into grayscale images (Fig.2.8c). The conversion can help to reveal the distribution of sample (ink)[67], with the grayscale value relating to the height of distribution. Fig.2.8b shows the grayscale at three positions: sample channel, middle junction, and observation channel, at three different velocities of 1 m/s, 15 m/s, and 40 m/s.

In the sample channel, the grayscale is the lowest at a velocity of 40 m/s, which represents in the deepest red colour. Since the concentration of ink was not changed during all experiments, the grayscale of sample channel keep constant in all flow velocity conditions. Thus, the difference in grayscale was caused by channel deformation under high pressure at a high velocity (i.e., 40 m/s). Ink at 40 m/s has the lowest grayscale in the middle junction and end of the observation channel, and the grayscale became the largest in the observation channel. It indicated that most samples may be pressed to the bottom of the channel by sheath fluid when flowing into the junction. On the contrary, the grayscale has similar minimum value at all three positions when the velocity is 1 m/s, because the hydrodynamic force compressing the samples is smaller at a lower velocity. Samples pressed to the channel bottom in junction may not be observed clearly by images, but the shape of ink distribution could be observed by binarization of grayscale pictures shown in Fig.2.8c, with threshold grayscale value of -0.015. Fig.2.9 shows the width of pressed samples in junction at different velocities; a higher velocity causes a stronger hydrodynamic effect, which in turn leads to a narrower distribution of the sample. Also, the ink distribution shows a similar tendency in the simulation.

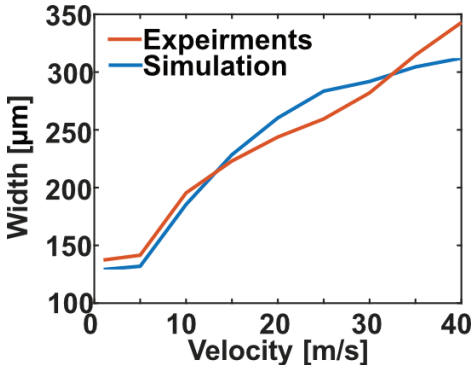

Figure 2.9: The width of compressed sample in junction.

As the grayscale is corelated to the ink distribution, the results indicated that hydrodynamic focusing only has a low efficiency in channel height dimension (weak vertical focusing) at a low velocity, which is not suitable for an optical imaging method having limited depth of focus. On the other hand, the sample could be focused close to the bottom of the channel at a higher velocity, allowing better optical imaging performance.

However, higher velocity always means a larger pressure in the channel, and pressure acts on channel wall and cause the deformation. In the grayscale of sample channel and red ink in Fig.2.8a, the grayscale of sample and wall at 40 m/s is lower than 1 m/s, one reason is probably due to the deformation of the sample wall under high pressure. Fig.2.10 shows the minimum grayscale along the flow direction in experiments and simulation, as the red dot line marked; the tendencies of 1 m/s and of experiments are similar to simulation; but since the flow velocity increases to 40 m/s, the tendencies were abnormal. This is mainly caused by the deformation of sample channel at high velocity; the grayscale of sample channel shows that the sample of red ink is thicker at 40 m/s than 1 m/s, relating to the lower grayscale. But the thicker sample at 40 m/s is compressed to lower height and finally focused to the bottom of the observation channel.

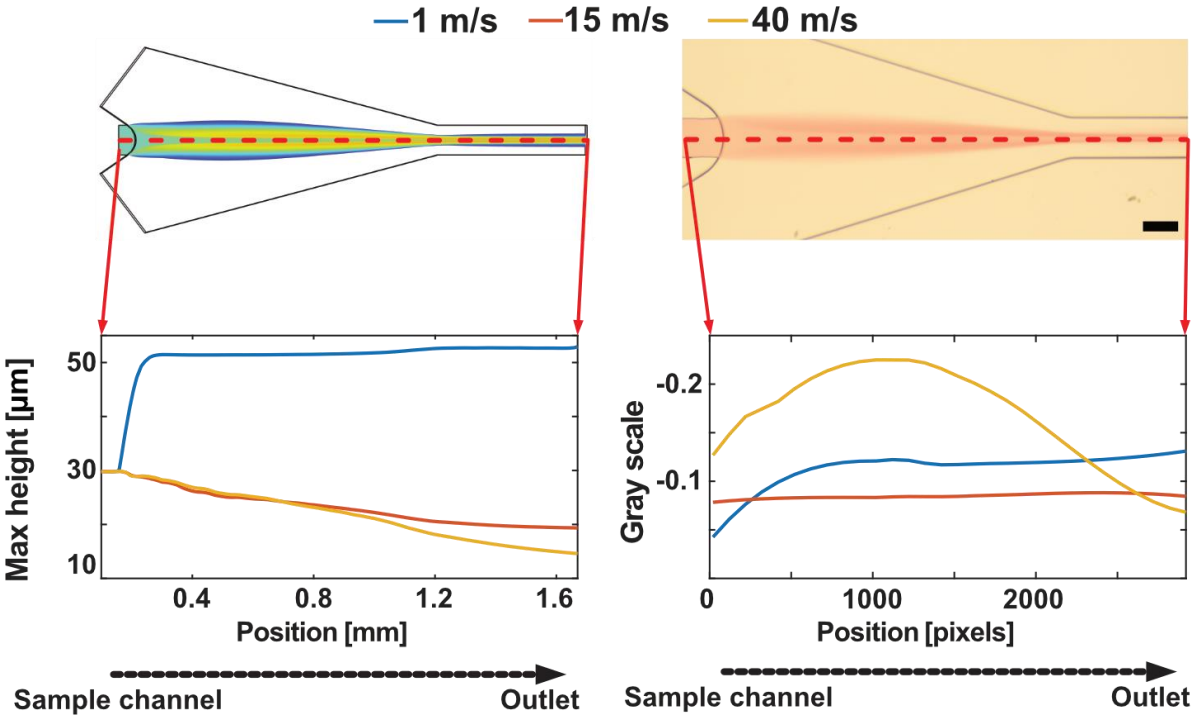

Figure 2.10: Maximum height of sample in simulation (left) and minimum grayscale of red ink (right) in flow direction; the position of pixels on right graph comes from the pixel location of photo; the zero values of simulation and experiments starts from the geometry of sample channel in simulation and the first column of the photo, respectively.

The relation between ink distribution and velocity clearly shows that the sample can be focused to a wide stream for obtaining more target objects in the FOV, and concentrated within a narrow stream in observation channel to direct target objects closer to similar optical focal plane.

2.3.3. Wall deformation analysis at high velocity

As the material (PDMS) of microfluidic chip is soft, the deformation of microchannels at high pressure caused by high velocity is unavoidable. The large deformation can extend the area of the cross-section of channel, and reduce the practical velocity in channel based on the setting flow rates. The experiments of red ink and simulation indicate that the effect of channel deformation on distribution of the sample is low; but for OTS microscopy, velocity is one of the most important

parameters to create blur-free images. Fortunately, the observation channel is directly linked with the outlet, where the pressure is small to the environment, the atmospheric pressure. This makes the end of the observation channel have a lower pressure and less deformation than other channels such as junction and sample channel, enabling a stable velocity.

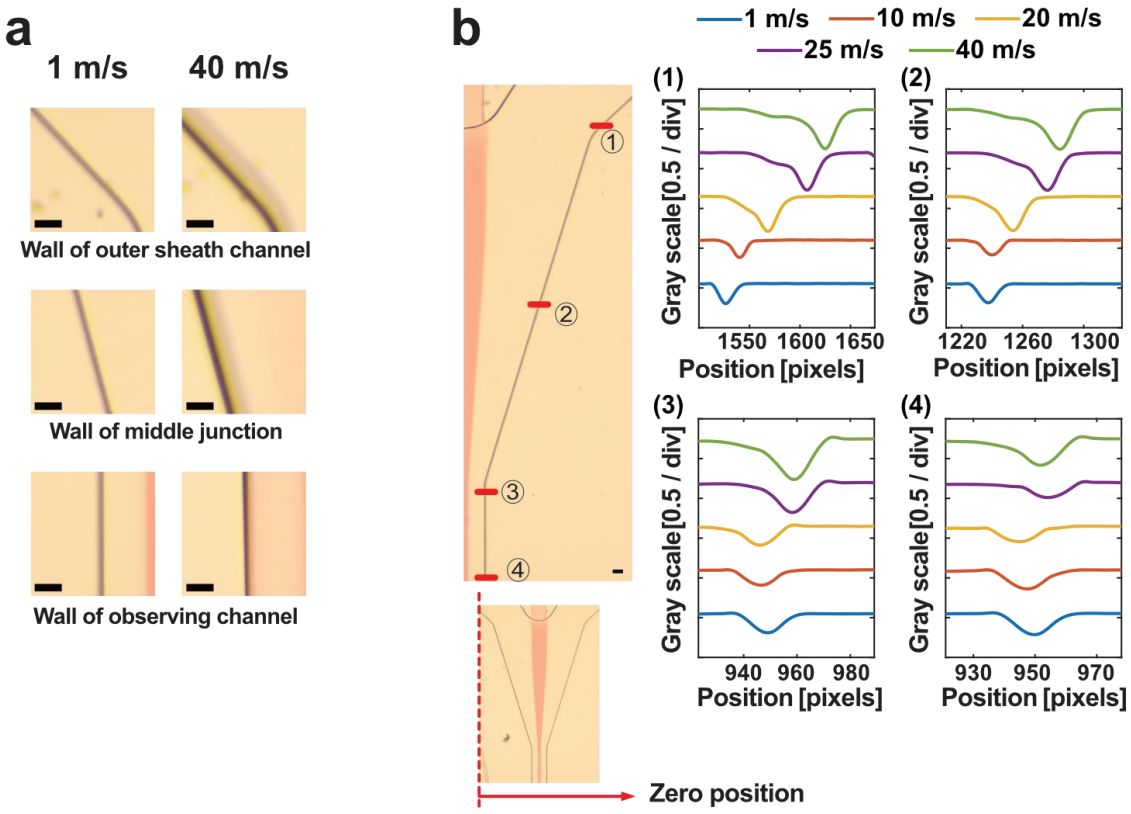

Figure 2.11: Wall deformation at different velocities. (a) Differences of channel walls at 1 m/s and 40 m/s (left), four positions of the wall used for observation and comparison (right), scale bar 25 µm; (b) Grayscale of channel walls of four positions at different velocities of 1 m/s, 10 m/s, 20 m/s, 25 m/s, and 40 m/s, the position is also from the photos, the left side is the zero position.

Fig.2.11a resents the images of the channel walls, including walls at three positions with velocities of 1 m/s and 40 m/s. It is clear that the width and grayscale of the wall is wider and lower, respectively, at 40 m/s than at 1 m/s, which reflects large expansion of walls at a high velocity. One probable reason of the grayscale at high velocity is the deformed wall have the arc shape which extending the wall projection and the liquid in this area cause the light scatter. The

grayscale of walls in images are picked out to investigate the effect of velocity on wall deformation. As shown in Fig.2.11b, four positions of the wall are concerned, from the sample channel (high pressure) to the observation channel (low pressure). The four small graphs represent the waveforms of walls at different velocities at four locations shown in Fig.2.11a and marked in Fig.2.11b. Walls of sheath outer channel and junction have a tendency to move far from channel, due to the expansion of the channel at high velocity, and the grayscale of wall is low at high velocity. But this pheromone is not too clear for the wall of observation channel. Fig.2.12 shows the evaluation of wall deformation using three parameters, width expansion rate of wall, the distance extension of a pair of walls, and the grayscale of wall. When velocity increases to 20 m/s, the width extension rate and distance extension of sheath channel and junction increase rapidly, and the grayscale of the wall decreases. Meanwhile, the observation channel shows a small difference between the beginning and the end. This is mainly due to the pressure distribution at high velocity; the observation channel is directly linked with the output chamber, and the local pressure is as low as the external environment. The high velocity in the narrow observation channel requires extremely high pressure at the beginning of the observation channel, which causes the high pressure in sheath channel and junction, resulting in large deformation of walls in these places.

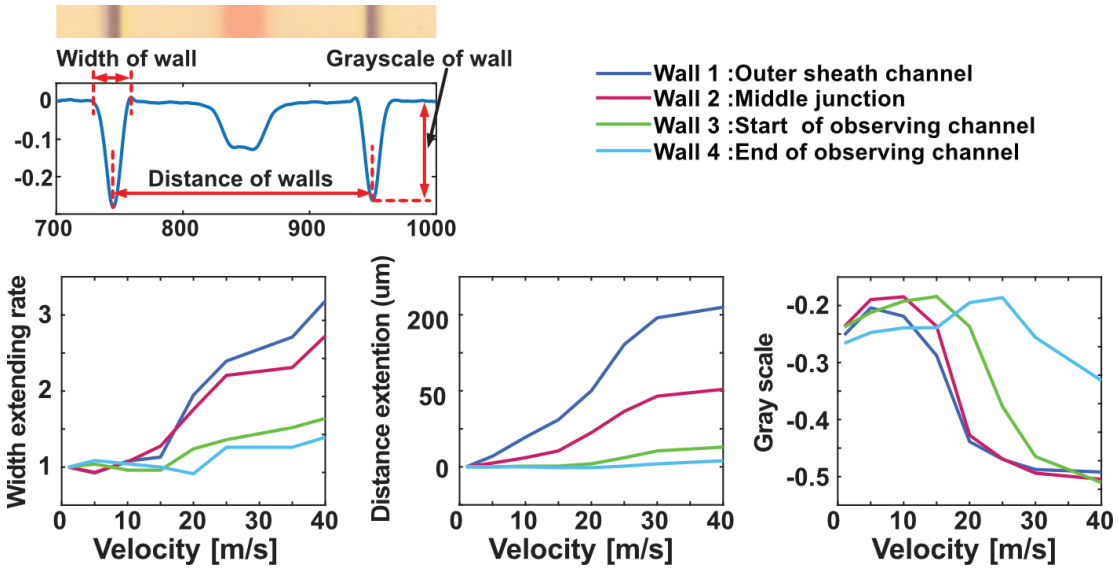

Figure 2.12: The evaluation on wall deformation, the extension of the waveform of the wall, distance of a pair of walls, and the grayscale of the waveform of wall over a range of velocities

The deformation of the observation channel wall is quite low, especially on the end side (wall 4 in Fig.2.12), because the three indexes of observing channel shown in Fig.2.12 have less changing as the velocity increase from 1 m/s to 40 m/s, comparing to the other places of wall (wall 1, 2 and 3); which means the velocity is quite similar to the expected value, which is related to the flow rate and channel cross-section. Then the imaged cells can reach the high expected velocity.

2.4. The OTS images of cells at extreme high velocity

2.4.1. OTS images of signal cell

The horizontally connecting microfluidic chip I made is quite rigid, and the shorten channels shown in Fig.2.4c can significantly reduce flow resistance; these make it quite easy to reach an extremely high velocity, up to 40 m/s by common syringe pump. Concerning the large load of pumps at high velocities, three independent syringe pumps are used to drive two sheath and one sample fluids. The ratio of flow rates of sheath and sample was still set as 2:2:1, and velocity of 1

m/s for total flow rates of 0.42 mL/min. By using the three pumps, cells can be driven into the channel and imaged at a velocity of 40 m/s; total flow rates were set as 16.8 mL/min, 6.72 mL/min for sheath fluids, and 3.36 mL/min of sample fluid. It should be noticed that, 40 m/s is not the limit of proposed PDMS device; the bottleneck of the system is the common syringe pumps I used which have the maximum load of 75 lbs (33.75 kg). When I set total flow rates larger than 16.8 mL/min, one of three pump stop to work with alert of over load, while no leakage or damage occurred to my chip. Meanwhile, large push force can easily break the barrel flange of the syringe, causing velocity loss. Theoretically, the velocity directly relates to the flow rates, but for better accuracy, the beads will be used as the reference to check the velocity before cell imaging.

In OTS imaging, the two-dimension images are composited with many one-dimension waveforms; dispersive laser pulses irradiate cells, making pulses contain space information of cells (light intensity difference). Therefore, the two dimensions of composite images from OTS imaging are the space dimension and the time dimension. Fig.2.13 shows the typical images of polystyrene beads from the OTS imaging; both the width and length of the images are 40 μm. The optical path determines the width, which is space dimensional; time dimensional length is determined by the velocity and repetition rate of the laser (80 MHz). Pulses irradiate on target objects like particles and cells, the higher velocity of objects mean fewer pulses scanned during the imaging process.

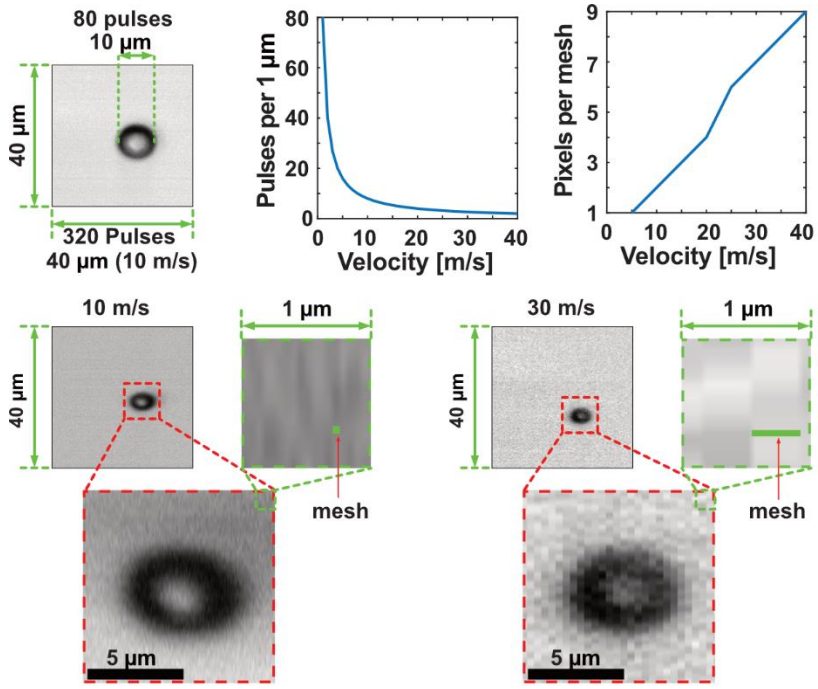

Figure 2.13: The quality of the OTS images relates to the velocity of objects; OTS images of polystyrene beads, higher velocity means fewer pulses and longer meshes for image composition; images of 5 µm beads at 10 m/s and 30 m/s show a great difference in quality.

For example, 10 µm cells moving at a speed of 1 m/s, 10 microseconds are required for cells from the beginning to end; 10 microseconds include 800 pulses due to the repetition frequency. Pulses number (n) for images could be calculated by velocity and laser frequency: ***n=(f*L)/u***; ***f*** means the repetition frequency of laser, ***L*** is the length of the image I want, e.g., 40 µm in Fig.2.13a, and ***u*** is the velocity of objects. It is evident that the number of pulses and velocities has an inverse relation. Low pulses at high velocity can significantly decrease image quality, like the two small 10 µm *10 µm graphs of 5 µm particles in Fig.2.13a, quadrilateral meshes could be observed for particles at 30 m/s while he ones at 10 m/s are quite smooth. And from the 1 µm * 1 µm section of the tow graphs, the basic meshes are emerged, the meshes at 30 m/s are wider than the ones 10

m/s, but the height is the same. This is because the graphs at 10 m/s and 30 m/s have the same space resolution due to the same optical path, and the time resolution is different due to the velocity.

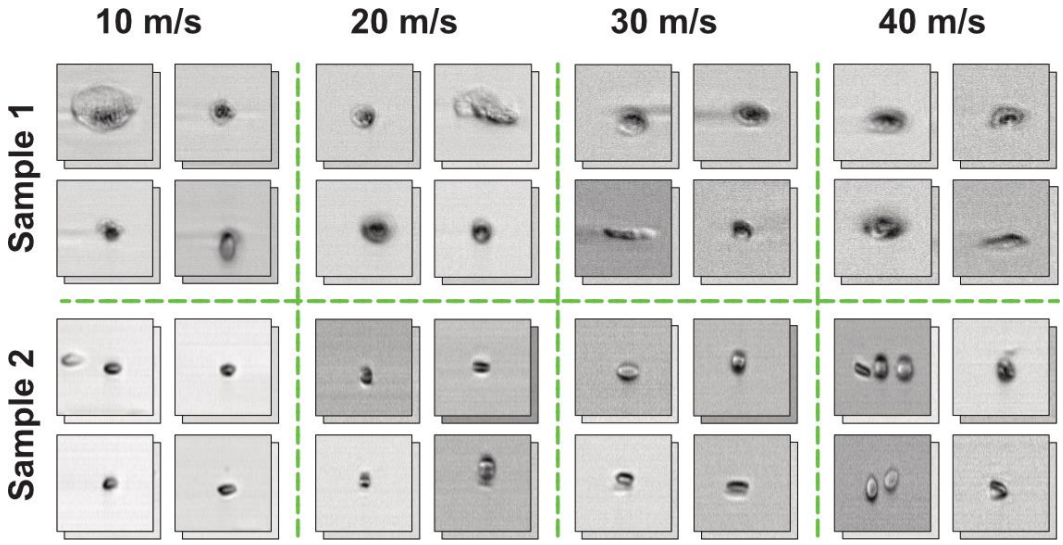

Figure 2.14: Images of cervical cells (sample 1) and whole blood cells (sample 2) at different velocities of 10 m/s, 20 m/s, 30 m/s, and 40 m/s, each image has a size in 40 µm* 40 µm.

Fig. 2.14 shows images of cervical cells (sample 1) and whole blood cells (sample 2) at four different velocities of 10 m/s, 20 m/s, 30 m/s, and 40 m/s, the size of all images are 40 µm* 40 µm. It shows that cells could be clearly observed at 10 m/s and 20 m/s, and the background was also smooth. The surfaces of cells are clear to the background. As velocity increases to 30 m/s, fewer pulses are taken for images, and the interfaces turn slur, especially in the time dimension. The image quality will unavoidably decrease as the flow velocity increases, which can be translated into two reasons. Firstly, as the flow velocity increases, each cell image consists of fewer pixels (pulses) in the flow direction, which will decrease the image quality and has been analyzed and discussed above. The second one is motion blur due to the exposure time which is determined by laser pulse. To minimize photodamage to the cells and reduces the level of spectral distortion of the pulses, the temporal disperser (frequency to time conversion) of the OTS imaging system used for testing is placed before the first spatial disperser. However, this configuration will increase the

exposure time per pulse from the femtosecond magnitude to 5.5 ns of my OTS imaging system so that the head and tail of each pulse will have a longer relative displacement in space while arriving at flowing cell, which will cause uncertainty in the measurement of cell size. As the flow velocity increases from 1m/s to 40m/s, the theoretical relative displacement of each pixel calculates from 5.5 nm to 220 nm. Although the relative displacement accounts for nearly one-third of the theoretical resolution of 780nm at the flow velocity of 40m/s, there seems to be no severe motion blur of the cell images shown in Fig.6b, the outlines and details of the cells can still be resolved. The motion blur phenomenon can be alleviated by placing the temporal disperser (frequency to time conversion) after the second spatial disperser, and the image quality can be further improved at ultra-high flow velocity in theory.

As the resolution on time scale of OTS images is directly related to pulse number per unit length, it should be weight between the throughput and the quality of images. The increase in velocity can result in the low time resolution, but the space resolution has no change. Therefore, laser with a higher repetition rate can be used for high time resolution, allowing a higher velocity, but sacrifice the space resolution. These parameters all can be adjusted to get higher quality of images in my system. For application in single cell analysis, the low-resolution images can be enhanced by deep-learning networks to obtain high resolution[122]. Alternatively, the low-resolution images can also be used to perform analysis on cells with specific features.

2.4.2. Cell focusing and distribution at high velocity

To image and detect as many cells as possible, cells should be focused near focal plane as much as possible. In my design, sample is pressed to the channel bottom by two sheath flows under higher velocity, allowing the focusing of cells close to the optical focal plane in the FOV to image

more cells clearly. In this section, I count the number of cells imaged by OTS microscopy from whole blood sample to test the effect of focusing and the distribution of cells at different velocities. The ratio of sheath and sample fluids is set as 2:2:1.

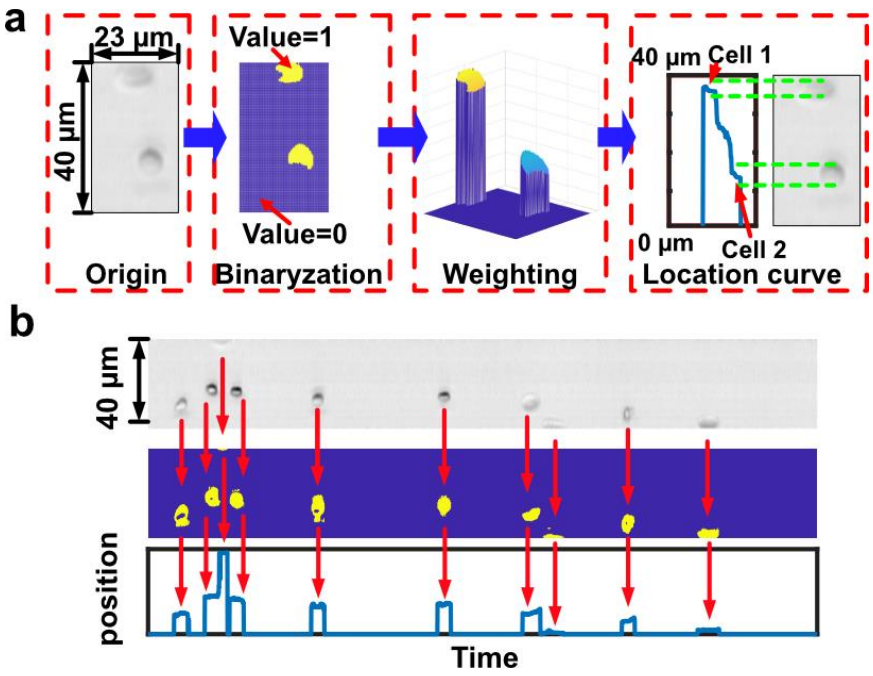

Figure 2.15: The cell position measurement; (a) Processes of cells number and location measurement; (b) Relation of long OTS image, binarization graph and cell position curve;

Beside images of single cell, OTS microscopy can also continuously image with large time window, which correspond to long images containing many cells. As shown in Fig.2.15a, to analysis amount and distribution of cells, OTS image is firstly transfer to binarization graph, value 0 for background and 1 for cell; and then weight value with the location of channel. For example, images showing in Fig.2.15a is 40 μm which is the size of FOV, the up line of matrix will value with 40 while the down line will value with 1. By this way, one OTS image can transfer to a 3D matrix, and the value on z-axil means the location; by calculating all nonzero value at every column, a curve is got which can reveal the number and location of cells in every OTS images. However, this method only works when cells are not too concentrated. Fig.2.15b shows a long OTS image

of blood cells, the binarization picture (threshold value -0.02) and the position curve of binarization picture; each peak of wave represents each cell in image, the amplitude of peak represents the location of cell.

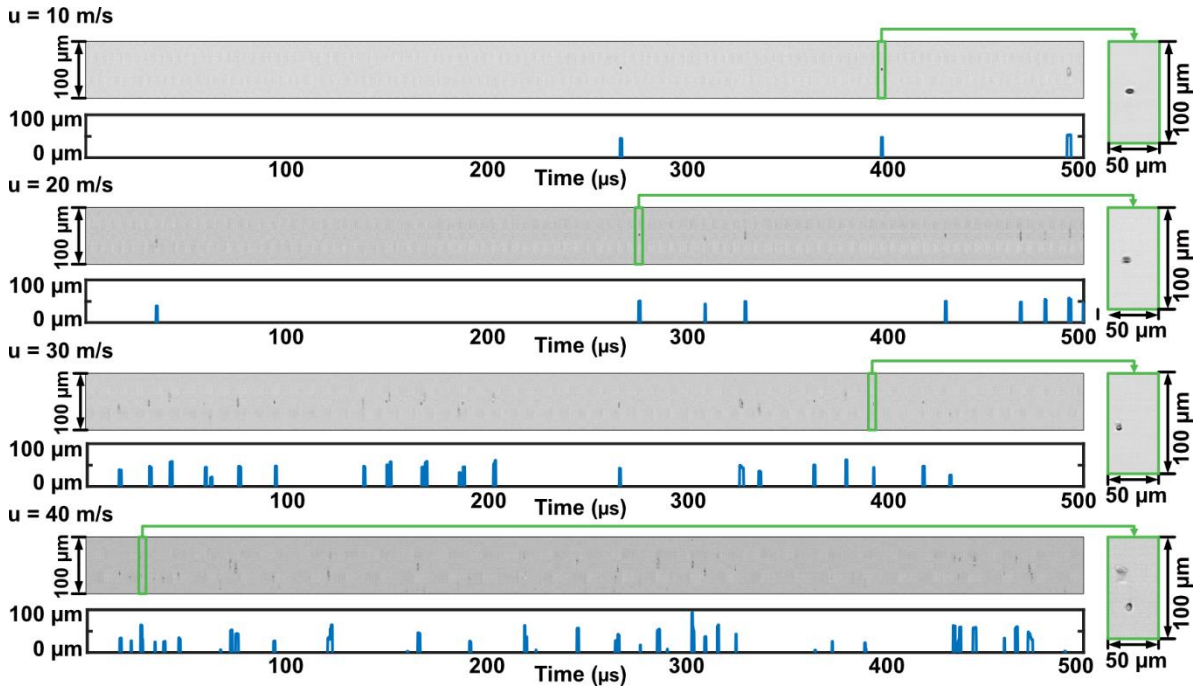

Figure 2.16: Long OTS image and position curve of blood cells at 10 m/s, 20 m/s, 30 m/s and 40 m/s, each OTS image is 100 µm high and 500 µs wide, each OTS image is compressed on wide dimension but cells can be extracted and unfold to real size showing in right;

After changing the groove density of grating to 1200 lines/mm, and setting the sampling rate to 40 GS/s (gigasamples per second), I obtain long-time OTS images with 100 µm FOV at different flow velocity. Fig.2.16 shows the long-time compressed OTS images of 5,000-fold diluted whole blood sample at 10 m/s, 20 m/s, 30 m/s and 40 m/s from OTS microscopy. Each image is 100 µm high in space domain and 500 µs wide in time domain, the real space width is 5,000 µm, 10,000 µm, 15,000 µm and 20,000 µm from 10 m/s to 40 m/s, respectively. Cells in compressed images are not shown in real ratio of height and width in space domain, but every cell image can be extracted and unfolded. Below every long OTS image, position graph represents where cells

located. The position graph of 10 m/s only have 3 peaks with similar amplitude near 50 μm which means 3 cells all flow in the middle of channel; and with velocity increasing, more peaks occurred with various amplitudes. Like graph of 40 m/s contains 35 peaks, and 7 peaks have more than one amplitude, 42 cells in this image; meanwhile, the amplitude of peaks range from 4 μm from 94 μm.

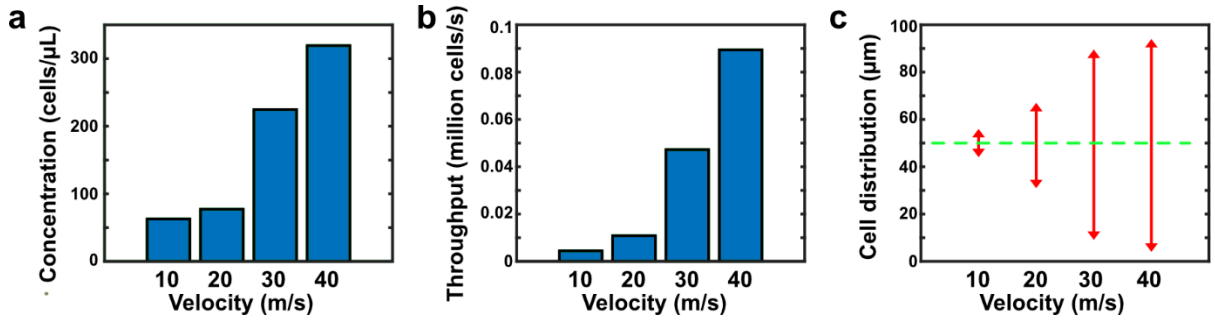

Figure 2.17: Cells counting and distribution at different velocities; (a) Concentration of detected cells at velocities from 10 m/s to 40 m/s; (b) Throughput at velocities from 10 m/s to 40 m/s; (c) Cells distribution on the wide dimension at velocities from 10 m/s to 40 m/s, the green dotted line represents the middle of channel.

Fig.2.17a shows the concentration of detected cell which is calculated based on the counted cell number and flow rate at each velocity, it is cleared that the average concentration of detected cells increases from 62 cells/μL at 10 m/s to 320 cells/μL at 40 m/s; as the cell concentration of sample is never changed, the improvement on concentration of detected cell at high velocity is mainly relating to the good vertical effects at high velocity that make much more cells flow near the optical focal plane, results in more cells imaged successfully. Fig.2.17b shows the throughput, calculated by cell number and duration of each image, throughput of the long images increases from 4,400 cells/s at 10 m/s to 89,400 cells/s at 40 m/s. Fig.2.17c shows the distribution of cells, cells distributed in the middle 12 μm wide range at 10 m/s and 90 μm wide range at 40 m/s.

As section 2.3.2 mentioned, higher velocity can press sample near bottom and disturbed wider. The concentration of detected cells increases 4-fold from 10 m/s to 40 m/s, which means more

cells are imaged at high velocity; which verify the focusing effect on height dimension. For throughput, the improvement of high velocity is much higher, the throughput improves 20-fold at least with velocity increase 4-fold. Velocity can enhance the focusing effect on height dimension, making more cells near one plane; on the other hand, cells distribute wider on wide dimension of channel. Similar results are investigated in section 2.3.1 and 2.3.2, sample focus to middle at low velocity and to bottom at high velocity.

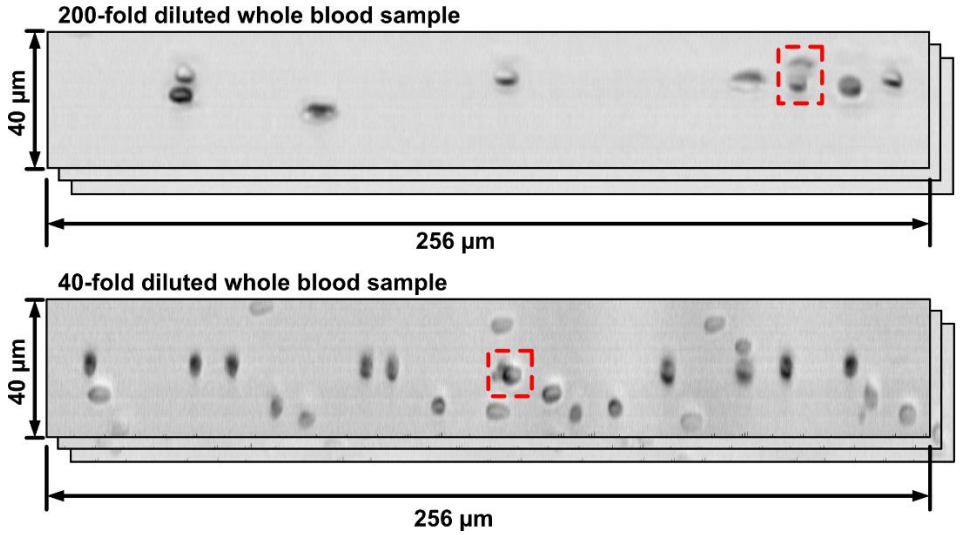

Figure 2.18: Cells counting and distribution at different velocities; (a) Concentration of detected cells at velocities from 10 m/s to 40 m/s; (b) Throughput at velocities from 10 m/s

Beside increasing velocity, wider channel with wider FOV can make also increase more detected cells and throughput[18], [19]. Moreover, in the long OTS images shown in Fig.2.16, most area of image is empty, with no cells. This means, the concentration of detected cells and throughput can be enhanced by directly increasing the cell concentration of sample. Fig.2.18 are the OTS microscopy of 200-fold diluted whole blood sample and 40-fold diluted whole blood sample at the same velocity of 10 m/s, respectively. It is clear that, image of low dilution sample contains more cells. Image of 200-fold whole blood contain 9 cells and 27 cells. However, high concentration of sample is easy to make cells reunite and overlap, like marked in Fig.2.18, causing

blur boundaries of cells in images; which means high concentration can lead cells reunite and even overlap, disturb imaging quality. And the overlapped cells can easily avoid by decrease the sample concentration and shaking longer time of sample before experiments.

2.5. Summary

This chapter aims to achieve a high velocity in PDMS microfluidic device to release the imaging potential of optofluidic time-stretch microscopy which is claimed to have the ability to image objects moving at 60 m/s, and even for all kinds of flow cytometry. To overcome the limitations of common microfluidic devices, I created a new method to fabricate microfluidic chips with horizontal connections. I found that channels could be minimized and designed in this way by shorten the length and part of channels. Based on this glass-PDMS-glass structure with resin reinforcement, the microfluidic chip can have a strong strength to allow higher flow rates and velocity. Also, microchannels with two layers were designed, which has a 30 μm high sample channel and two 70 μm high sheath channels. With this chip, I can realize cell imaging at 40 m/s. To the best of my knowledge, this developed microfluidic device for imaging cytometry can achieve the fastest velocity over the world. As this two-layer microchannel can press sample flow near bottom of channel; which means more cells will flow near the optical plane, making more cells detected. This focusing effect will be more effective at high velocity, like 40 m/s. Meanwhile, I image 5,000-fold diluted whole blood sample to verify the focusing effect, concentration of detected cells and throughput can improve 5-fold and 20-fold from 10 m/s to 40 m/s, respectively.

For precise cell detection and analysis, the imaging quality and stable position of cells may have to be considered simultaneously, micro channels can be optimized and the ratio of flow rates between sample and sheath flows could be optimized for higher suitability on single-cell analysis.

As I have the fastest imaging system and the fastest cell cytometry, the fastest data processing system could be developed in the future to realize the integrated real-time cell analysis system. Due to high performance of my new microfluidic chip, e.g., high velocity and the minimized size, it could be a new way to investigate the high inertial effects in microfluidics for cell sorting, deformation and preparation.

3. Highly sensitive impedance flow cytometry

3.1. The sensitivity of impedance flow cytometry

In terms of single cell detection, the sensitivity of impedance cytometry is quite important which determines the applicable size of single cells/particles. To date, the sensitivity[125] has been shown to be related to channel dimension[124], electrode layout[125], fluid conductivity[126], and electrode dimensions so far. Any tiny changes in electrodes or microchannels would be shown on the magnitude of impedance pulses. Based on this phenomenon, a selective method of improving the detection sensitivity is to wide electrodes or narrow detection channels for a strong electric field[123], as a result of sacrificing signal-to-noise ratio (SNR)[127]. Besides the method to improve sensitivity by enhancing the amplitude of signals, improving the relationships between signal to cell itself, rather than the position of cell, can always help to improve the detection accuracy and sensitivity. Moreover, in some situation, the electrode layout and even the samples can also affect the sensitivity.

In this chapter, three works were carried on how to improve the sensitivity of impedance flow cytometry, to achieve highly accurate detection. The three works include utilizing narrow electrode span, cell focusing by viscoelastic solution, and the investigate of droplet impedance measurement.

3.2. The material and methods

3.2.1. Experiments setup and data process

Fig.3.1a shows the impedance flow cytometry system in my experiments based on circuit of FPGA (field-programmable gate array)[128]. In detection, a 3.3 V voltage signal with two different frequencies was generated by a FPGA-based lock-in amplifier (Diligent Eclypse Z7, USA), and connected the central electrode; the different frequency will apply on different

situations which depends on the conductivity of the solution and objects. Current signals propagated from the central electrode to both detection electrodes through the conductive fluids in the microchannel. When single objects flow through the detection area, the induced current fluctuation on two detection electrodes were detected and converted to voltage signals by I/V converter. A differential amplifier was employed here to compare the signal fluctuation on two electrodes and transmit the results to the lock-in amplifier. In the lock-in amplifier, current signals were deconvoluted to the impedance signals at two frequencies, which were then collected by a data collector (USB-6363 BNC, National Instruments, USA) at a sampling rate of 125 kHz and displayed in NI DAQExpress (National Instruments, USA) on PC in the meantime.

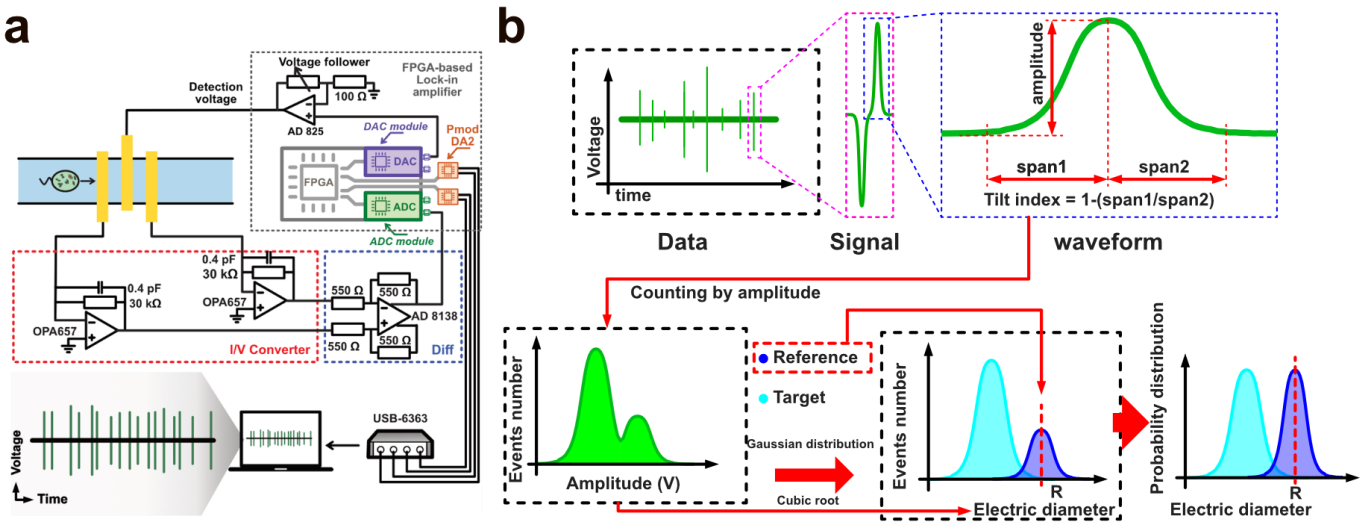

Figure 3.1: The constitution and signal process of FPGA-based impedance flow cytometry system; (a) the structure of FPGA-based impedance flow cytometry; (b) the data-processing of impedance detection.

To analyze the results, recorded data was imported to MATLAB at first, so that to characterize the impedance signals via two dielectric properties, i.e., the electrical diameter and tilt index. All signal processes were performed by lab-made scripts. The data-processing is shown in Fig.3.1b, the signals of particles or cells will be firstly picked out from recorded data base, and then calculate the amplitude and the width of waveform. With counting the number of signals with different

amplitude, signals can be sorted into an amplitude distribution. Besides, the electrical diameter[45] is defined as the cubic root of the impedance amplitude, which has been proved to be linearly correlated with the physical diameter of single objects. The tilt index [32], [129] is defined as the ratio of left-half impedance pulse to the right-half and minus one, which is used to characterize the shape of single objects. By gathering these features of signals, distribution of features can be obtained to reveal morphology and size of the objects. Additionally, the beads are always added into sample as the reference, the reference will act as the anchor of real size for accurate measurement. With Gaussian distributions matching, the distribution can be divided into several groups representing the objects; and the Gaussian distributions can also transfer to the probability distributions if the number of one cluster of objects is too low which makes it unobvious, the probability distribution is calculated based on each independent cluster of amplitude distribution. It is quite important to choose the applicable reference which should have the size different from the range of target.

With electric-based detection, the noise is unavoidable; as the connections between different conductors, the electromagnetic field in environment can all cause the noise. Decreasing the links and use shields can have better improvements on noise.

3.2.2. The simulation method of impedance detection

The simulation of impedance flow cytometry is to investigate the relationship between the amplitude of signals and the trajectory of cell. Thus, the simulation can directly be built by couple the electric field and flow field with solid-like cell. To investigate the impedance detection and sensitivity, numerical models are built by commercial software, COMSOL Multiphysics 6.0 (COMSOL Inc., Burlington, MA, USA). To correspond the simulation to the real situation, the

model will be more accurate to combine the AC (Alternating Current) module and FSI (Fluid-Solid Interaction) module, AC module to describe the electric field while the FSI module to describe the cell movement dragged by flow. However, AC module has only one variate of voltage, while the FSI module has at least five variates (two velocities, pressure, E- modulus and Poisson ratio) which means the FSI module is much more complex than the AC module. There will be much more calculating recourse required if couple with the FSI module to describe the movement of cell. After analysis of the theory of impedance signal generation, I found the flow have no influence on property of solution and the electric field distribution only relates to the materials of cell and solution whether they are moving or flowing. Therefore, to simplify the simulation, I build my model with just with AC module and transfer the dynamic process of cell movement to many static states of cell in different position. In addition, due to the same structure on the dimension of channel width, the simulation can also use the 2D model to improve the calculating efficiency. The simulation can be carried by couple the electric currents equation:

$$\mathbf{J} = \sigma\mathbf{E} + \mathbf{J}_e$$
$$\nabla \cdot \mathbf{J} = 0$$
$$\mathbf{E} = -\nabla V \qquad \text{(Eq.3.1)}$$

where the **J** represent the current density; σ denotes the electrical conductivity; $\mathbf{J}_e$ is the externally generated current density; **E** is the electric field, which is the gradient of voltage V;

Similar to the simulation of cell impedance detection, the model of droplet impedance detection is also built by AC module, the droplet is described just by define the geometry instead of common methods of droplet (Phase-field, Level-set), or define a function of related material parameter. But this is only suitable when there is no deformation occurs on droplet.

The parameters of the 1×PBS solution are 80 of the relative permittivity and 1.4 S/m of the conductivity. For droplet simulation, the oil parameters are set as 2.1 of the relative permittivity and 0.17 of the conductivity. The cell membrane and beads (polystyrene) are quite weak under low frequency alternating voltage, the cell and beads can be simulated as a cavity with shape of circle or sphere.

3.3. Improve the sensitivity by narrow electrode span

In this work, I provided an alternative way to improve the detection sensitivity, through narrowing the electrode span. The electrode span is found to impact the local strength of electric filed in the detection area, which could facilitate the detection of the tiny objects in a large channel.

Typically, the electrodes in impedance cytometry are fabricated by photolithography and lift-off. However, the fabrication of small electrodes or gaps is difficult, and the defects easily occur in developing process in lift-off with the feature size least to 1 μm. To avoid possible defects in photolithography, in this work, femtosecond laser was applied to ablate the electrodes to generate the small gap. As femtosecond laser is widely used in micro-nano fabrication[130] and even cells perforation[131] with high precious and low extra damage to materials, it is quite a potential way in electrodes fabrication.

To verify the sensitivity of electrodes with small gap, some indicator with small difference in size is needed, like yeast cells. Here I choose the yeast Saccharomyces cerevisiae, which is widely used in food industry and biology research[116]. In cell cycle of S. cerevisiae yeast, single cell always turns into budding situation with morphological changes[132], [133], the small difference in cell shape and size make S. cerevisiae yeast become the well indicator for various cell sensors[7], [33], and also my case.

Here, I improve the sensitivity of impedance cytometry by decreasing the gap of electrodes smaller to 1 μm while electrodes have the width of 30 μm. To investigate the effects of gaps on the detection sensitivity, numerical models were built by finite elements methods to express how the smaller gap could enlarge the local strength of electric field to generate higher differential signals when objects pass through electrodes. To verify my idea, experiments were performed on small particles (1 μm and 3 μm beads) and single cells. As a reference, electrodes with 5 μm gaps were also employed in experiments. The gap of 1 μm was fabricated by femtosecond laser ablation on whole electrodes, while 5 μm gap was directly fabricated by normal lift-off technology. In detection of polystyrene particles suspension with diameters at 1 μm and 3 μm, much more 1 μm particles could be detected and distinguished using electrodes with 1 μm gaps. And then, in the detection of yeast cells, the budding yeast cells could be successfully identified by the electrodes with 1 μm gap.

3.3.1. Microfluidic chip

The microfluidic chip in impedance cytometry is assembled with PDMS structure and glass with coplanar electrodes by inversible bonding after plasma treatment. The microchannel is got from casting mixed PDMS (SYLGARD 184, Dow Corning, Midland, MI, USA) on SU8 (MicroChem Corp., Newton, MA) mold by common soft lithograph. The electrodes which conclude two layers, about 70 nm thick chromium (Cr) on glass and 70 nm thick gold (Au) on chromium, are all fabricated by photolithograph and lift-off.

The microchannel in detection area is 12 μm wide and 10 μm high, while three coplanar parallel electrodes are 30 μm wide. In my research, there are two kinds of gaps of designed electrodes, 1 μm and 5 μm which are shown in Fig.3.2. Usually, the electrodes are initial design

on mask and fabricated with lithography and lift-off technology, as the electrodes with 5 µm wide gaps; however, feature size smaller to 1 µm increase the difficult of fabrication. To achieve the 1 µm gap of electrodes, the femtosecond laser is considered as it can be used to ablate some micro-pattern. With the assistance of femtosecond laser, the electrodes with 1 µm wide gap are successfully fabricated by ablate two 1 µm wide gaps in one 92 µm wide whole electrode to separate the one electrode into three independent electrodes. Additionally, by adjust the power of laser, the gaps can be fabricated much smaller, but it may increase the risk of short circuit. Before bonding with PDMS channel, the electrodes will be tested by Avometer to ensure the electrodes are not connected (short circuit).

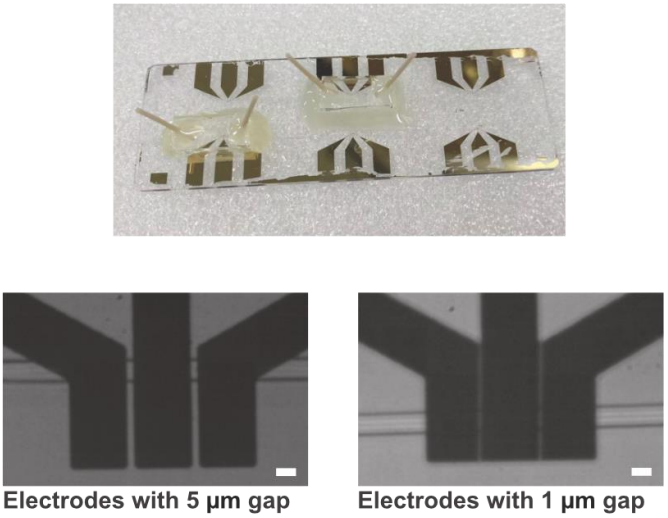

Figure 3.2: Microfluidic chip with two kinds of electrodes which have the gap of 5 µm and 1 µm, the 5 µm gap is direct fabricated by lift-off while the 1 µm gap is generated by FS laser ablation; (scale bar: 10 µm).

3.3.2. Sample preparation

In beads experiments, the mixed beads suspension contained polystyrene particles in diameter of 1 µm and 3 µm. The number ratio of 1 µm and 3 µm polystyrene beads in the suspension was around 9:1.

In single cell detection, S. cerevisiae yeast cells were employed, and all cells were pre-mixed with polystyrene particles in a diameter of 3 μm before experiments. The beads mixed in cells are used as reference. In detail, yeast cells were firstly diluted in 1× PBS solution and then put in a thermostat at 38 ℃ for 3 h for awake. Fig.3.3 shows the photos of particles and yeast cells under a microscope, normal yeast cells have a larger size than 3 um particles, while the budding yeast cells are larger than normal yeast.

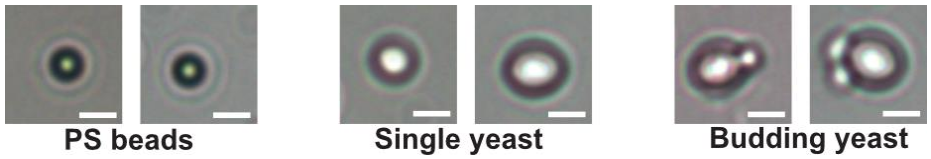

Figure 3.3: PS particles and yeast cells imaged with microscopy (scale bar: 5 μm).

Before experiments, all samples were transferred to a 1× PBS solution with 0.1% Tween 20 solution, to avoid sample aggregation. Sample suspension was loaded into the microchannel using a syringe pump with a flow rate of 10 μL/min.

3.3.3. The simulation of impedance with different electrode span

In the absence of objects in the detection area, the currents detected from two ground electrodes were equal, resulting in no impedance signals. As particles or cells passed the electrode span, the volume of conductive PBS solution above the span was replaced by the nonconductive object, inducing the sudden increase in the system impedance, i.e., impedance pulses. This is because of that the nonconductive objects interfere the current propagation above the electrode span. It is worth noting that the majority of current propagation took place near the electrode span in the fluid. As shown in Fig.3.4, a strong electric field was observed near

electrodes span. The differential current is the difference of the current from the two cathodes; due to the 2D geometry in simulation, the unit of current here is A/m.

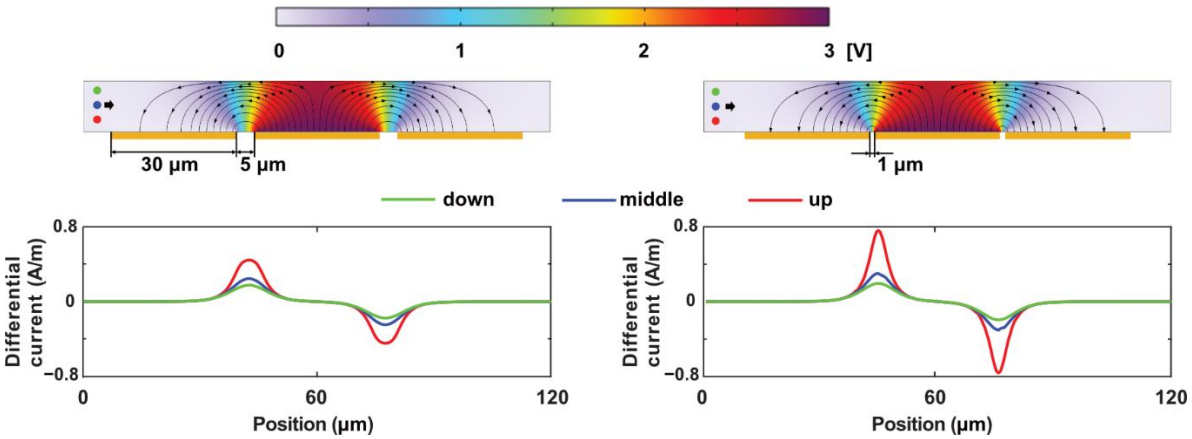

Figure 3.4: The simulation results about distribution of electric filed in the detection area of impedance cytometry (up), color represents the voltage, line with arrows means the current direction. The impedance pulses (down) were obtained when flowing 3 μm particle along three trajectories. The particles at different height in the channel (i.e., 3 μm, 5 μm, 7 μm to channel bottom) were labelled in red, blue and green, respectively.

To date, according to several impedance-related studies[45], [129], the 2D simulation is sufficient to analyze the relationships between impedance signals, single objects, and the detection electrodes. Therefore, in this work, I did not employ other methods (i.e., the analytical solution) to verify the simulation results.

Fig.3.4a shows the 2-D simulation of the impedance cytometry in my research, the gaps of anode and each cathode were 5 μm(left) and 1 μm(right) here. The color corresponded to the voltage distribution that diminishes from the anode to the cathode. When a 3 μm particle moved through the detection area, the impedance magnitude changed according to the different heights of the particle in the channel (i.e., 3 μm, 5 μm, 7 μm to channel bottom). In other words, the impedance signals of single particles are trajectory dependent. As particles get closer to the channel bottom, they induce higher impedance pulses. Due to the nonuniform strength of electric field in

micro-channel, current from anode propagates around the channel bottom. Additionally, when measuring a particle along the same trajectory, the highest impedance magnitude was measured for particles traveling through the 1 μm electrode span.

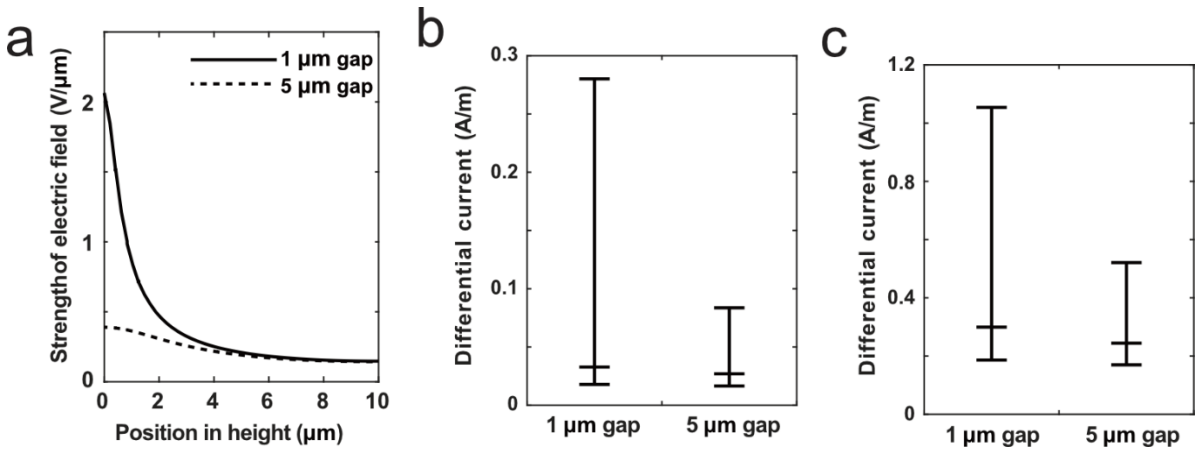

Figure 3.5: (a) Strength of electric field in the case of 1μm gap and 5 μm gap. (b-c) Relationship between the impedance magnitude and the electrode gap, when measuring (b) 1 μm and (c) 3 μm particle. The impedance magnitude increases with decreasing the electrode gap.

Fig.3.5a shows the strength of electric field at different depths at the center of the electrode span, as the strength of electric field is defined as **v**/*d* (**v** represents the voltage, *d* represents the distances between electrodes), by calculation the voltage gradient at every mesh point, the strength of electric field can be got. Compared to 5 μm gap, a 1 μm gap can result in a greater gradient of voltage between the cathode and anode, resulting in a higher strength of electric filed. In other words, there was a concentration of current near the 1 μm electrode span. With distance from the channel bottom, this field strength gradually dims. Interestingly, at a distance of 4 μm from the channel bottom, both types of electrode spans showed similar field strengths. This phenomenon indicates that regardless of the electrode span, both designs show the same sensitivity to single

objects beyond 4 μm from the channel bottom, while the 1 μm electrode span provides a greater sensitivity within 4 μm.

Figs.3.5b-5c illustrates the changes in the impedance magnitudes when measuring 1 μm and 3 μm particle, respectively. In Fig. 3.5c, the impedance magnitudes of 1 μm particles varied between 0.02 and 0.28, in the case of the 1 μm electrode span. By contrast, this value varied between 0.02 and 0.09, in the case of the 5 μm gap. 3 times higher impedance pulse was obtained by the 1 μm gap than by the 5 μm gap. Considering background noise in real experiments, low impedance pulses are difficult to be detected. Therefore, I assume that using the 1 μm electrode gap, the impedance pulses of tiny particles (e.g., 1 μm) could easily be seen instead of being buried in back-ground noise. Additionally, when measuring 3 μm particle, the 1 μm electrode span can also provide the highest impedance magnitude in comparison to the 5 μm electrode span. Notably, the lowest impedance magnitude for both types of electrode spans were the same, which is due to that the field density (> 4 μm from the channel bottom) of both designs were the same (see Fig. 3.5b).

In this 2D simulation, the electric field strength can be increased by reducing the electrode gap, resulting in a stronger impedance pulse of single objects. Objects with strong impedance pulses could be easily detected by the system, for example, a high amplitude makes it easy to distinguish small objects from noise and to detect them accurately.

Notably, the 2D simulation results here only indicated that narrowing the electrodes would improve detection sensitivity. Optimal electrode spans for detecting particles with different sizes require further research. Furthermore, the electrode size is also a key parameter for detection sensitivity that was found to increase with increasing electrode size[123]. In order study the impact of electrode span, all electrodes were designed to be 30 μm wide. Besides, the electrode length in this work was limited by the channel width (12 μm); it is not key parameter for detection sensitivity,

which has been verified in other work[43]. Additionally, in this work, all electrodes were fabricated as traditional coplanar electrodes to eliminate the impact of electrode morphology[134] on the detection sensitivity.

3.3.4. Experiments and discussion

3.3.4.1.Detection of single beads

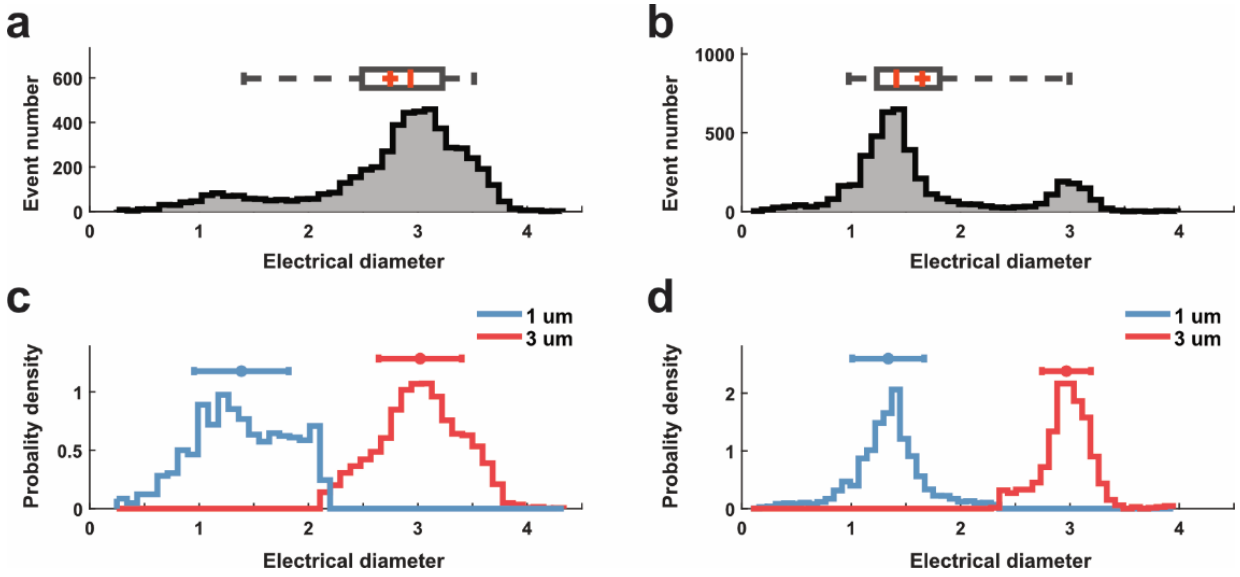

Figure 3.6: Electrical diameter of polystyrene beads when using different electrode spans for measurement (a-b) Distribution of electrical diameter signals of detected beads in suspension when measuring with (a) 5 µm and (b) 1 µm electrode span. (c-d) The discrimination of two sizes of beads using the single-peak gaussian model, based on their electrical diameters obtained with (a) 5 µm and (b) 1 µm electrode span. 1 µm beads were labelled in blue, and 3 µm beads were labelled in red.

To verify the impact of electrode span on the impedance detection, experiments were first performed on the mixture suspension of 1 µm and 3 µm beads. The impedance signals of both beads were calibrated to the electrical diameter which firstly are calculated as the cubic root of amplitude, as shown in Figs.3.6a-3.6b. Fig.3.6a indicates that the 5 µm gap was applicably for the detection of 1 µm and 3 µm beads, while there was an overlay area between both regarding the electrical diameter. Besides, using 5 µm electrode gap was more likely to fail to detect some 1 µm

beads than using 1 μm electrode gap; for example, in Fig.3.6b, there were much more 1 μm beads appeared in the distribution plot when using 1 μm electrode gap than 5 μm gap. In this work, the ratio of 1 μm and 3 μm beads in the suspension was around 9:1. When using a 1 μm gap, the measured electrical diameter was close to the real value, but it did not work with a 5 μm gap. This phenomenon was attributed to that most impedance pulses of 1 μm beads were covered by the noise, as their magnitudes were too small.

Additionally, the electrical diameters of 1 μm and 3 μm beads distributed compactly and did not spread out; this result indicated that the effect of individual particles could be ignored in analysis. When the impedance values were impacted by the particle trajectory, their impedance metrics (i.e., electrical diameter) were distributed widely, and sometime, their electrical diameter was not matched with the real diameter of particles[123], [135]. In this work, the microchannel was designed to be 12 μm wide and 10 μm high, which successfully limit the trajectory variation of single particles and resulting in the compact distribution of electrical diameters.

In Figs.3.6c-3.6d, I employed the single-peak gaussian model (Gaussian distribution fit) to discriminate the 1 μm beads from 3 μm beads based on their electrical diameter. Although it is possible to separate the two sizes of beads in both cases, there would be more overlapped area between two data sets when using 5 μm electrode span (see Fig.3.6c). The distribution of 1 μm beads was not perfectly isolated and spread out. By contrast, the well separation of the two data sets with less overlap could be realized when using 1 μm electrode span for measurement (see Fig.3.6d). Interestingly, when using 1 μm electrode span, the electrical diameter (about 1.3 μm) of 1 μm beads were slightly larger than their physical diameter. This is possibly because of that some beads flowed near electrodes in detection, and their impedance magnitude were enhanced greatly.

After the isolation, the ratio of 1 µm and 3 µm detected beads was about 4.52:1 (Real: 9:1), which means half of 1 µm particles were detected using 1 µm electrode gap. By contrast, the ratio obtained by 5 µm span was about 0.14:1, which was far away from the real ratio (9:1). All beads experimental results could demonstrate that the electrodes with 1 µm gap can improve the detection sensitivity for small particles.

3.3.4.2.Detection of budding yeast

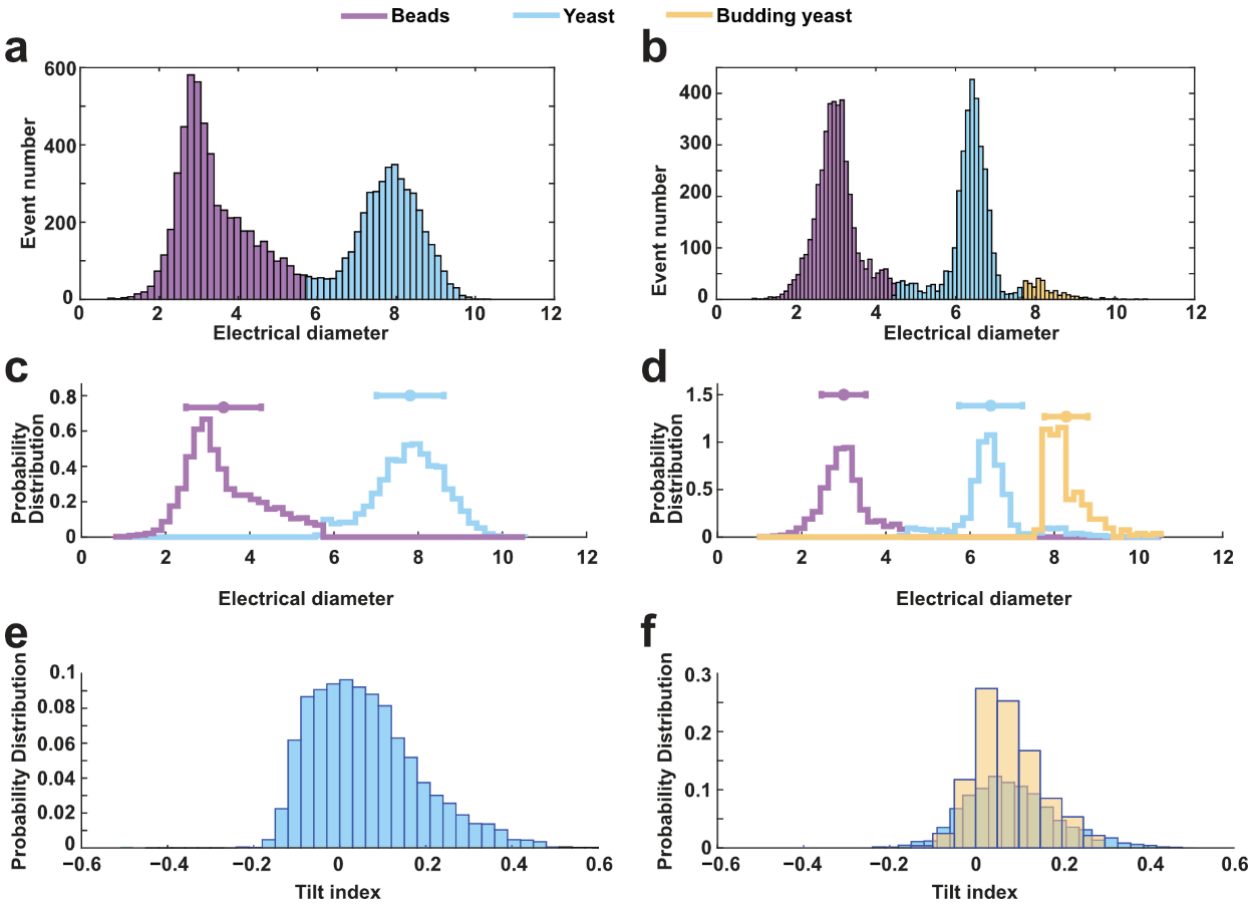

Figure 3.7: Dielectric properties of yeast cells when using different electrode spans for measurement, 3 µm beads were employed as the reference for calibration. (a-b) Distribution of electrical diameter signals of detected beads and cells in suspension when measuring with (a) 5 µm and (b) 1 µm electrode span. (c-d) The discrimination of reference beads and cells using the single-peak gaussian model, based on their electrical diameters obtained with (a) 5 µm and (b) 1 µm electrode span. (e-f)

Probability Distribution of the tilt index of impedance pulses obtained from electrodes with (e) 5 μm gap and (f) 1 μm gap.

The high sensitivity of impedance cytometry with 1 μm electrode span enables the detection of cells with small difference in size. In this work, yest cells were tested here, and 3 μm beads were employed as the reference for the calibration. Similar to most eukaryotic cells, yeast cells appear morphological changes in the cell cycle[34], [132], i.e., the cell budding. During the budding, the mother yeast cell produces a small bud that grows until it reaches a certain size and then separates[34].

In Figs.3.7a-3.7b, impedance signals, collected from 5 μm and 1 μm gap, respectively, were sorted into two data groups following gaussian distribution; one group with smaller electrical diameters represents the 3 μm reference beads, whereas the other group represents yeast cells. Previous research[33] has shown that the budding cells would have bigger electrical diameters than normal yeast cell. Comparing Fig.3.7a and Fig.3.7b, when the gap was set to 1 μm instead of 5 μm, the electrical diameter of 3 μm reference beads is much more centralized. Besides, in Fig. 3.7b, when using 1 μm electrode gap, there was a small cluster of data outside of the yeast cells, indicating the existence of budding yeast cells. By contrast, when using 5 μm electrode gap, the electrical diameter distribution of yeast cells was decentralized in a wide range from 5 μm to 8 μm, in Fig.3.7a. There is no clear difference between normal and budding yeast cells in terms of yeast cells; one probable reason is the low sensitivity of 5 μm gap which cause the wide distribution and the signal of budding is covered by other yeast cells. In terms of detecting the same yeast cell suspension, the electrical diameter of yeast cells in Fig.3.7b could provide more details in the cell

volume. This phenomenon can be attributed to the high sensitivity of impedance detection for the cell volume with 1 μm electrode span.

Figs.3.7c-3.7d show the distribution of the tilt index of impedance pulses when measuring with 5 μm and 1 μm electrode gap. The tilt index was employed to characterize the shape of single objects, which is calculated based on the widths of the two-side half of peak from the maximum value. In theoretic, objects with symmetric shapes, such as spheres, should have a tilt index of around zero; but objects with unsymmetric shapes would have a nonzero tilt index. The tilt index increases with increasing the unsymmetric level of single objects. Typically, yeast cells were not in a perfect symmetric shape as beads, thus, their impedance pulses would be asymmetric in shape, resulting in a tilt index away from the zero. In Fig.3.7(e), the tilt index of thousands of yeast cells was not evenly distributed around zero, which was attributed to their asymmetric shape. In Fig. 3.7(f), I took advantage of the difference in cell size between yeast and budding cells to isolate the tilt index of budding cells from others; the tilt index of yeast cells and budding yeast cells ranged from about -0.2 to 0.4 and -0.1 to 0.3, respectively. There is no clear difference between budding or normal yeast cells regarding the tilt index. The results show that the tilt index might not be sensitivity enough to monitor the morphology change induced by the cell budding in this work. But it is worth mention that the electrode span of 1 μm still performed better for the morphology determination, as the distribution of tilt index was more centralized when using 1 μm electrode

span rather than 5 µm span. The photos of yeast sample in experiments can be found in Fig.3.8, the number of budding yeast cells is lower than normal yeast.

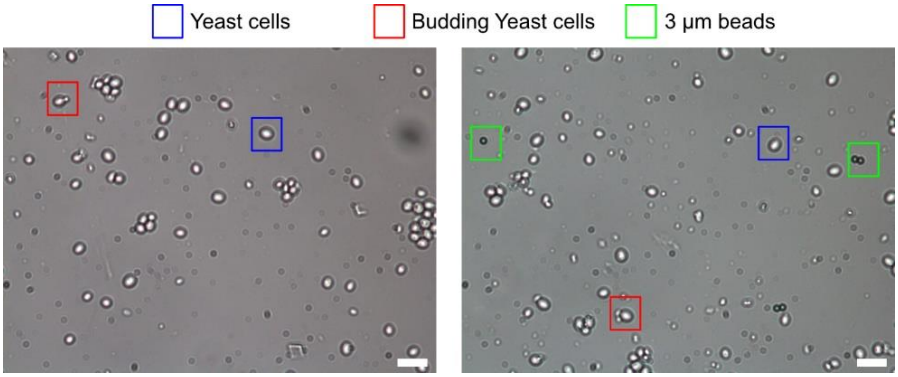

Figure 3.8: The photos of yeast sample in experiments, three kinds of objects are marked in pictures; the number of budding yeasts is lower than normal yeast cells. In the two photos, there are about 7 budding cells and more than 80 yeast cells, the ratio is about 1:10, scale bar: 20 µm.

Fig.3.9 shows the scatter plot of electrical diameter vs tilt index, the data is same as shown in Fig.3.7. In Fig.3.9a, the impedance detection with 5 µm electrode span resulted in there were a large overlayed area between the reference beads and yeast cells. In contrast, Fig.3.9b is the scatter plot of impedance signals measuring from electrodes with 1 µm gap, three groups of points could be clearly distinguished, including 3 µm reference beads, yeast cells and budding yeast cells, respectively. Here, a cluster of cells were found to have a bigger volume than other cells and identified as the buddying cells; this is because the budding cells typically had bigger cell volume, resulting in bigger electrical diameter in impedance detection. Besides, the microscopic images also indicated the existence of buddying cells in the detection suspension (see Fig.3.8). As a result,

it is easy to conclude that the sensitivity of impedance cytometry could be improved through narrowing the electrode span.

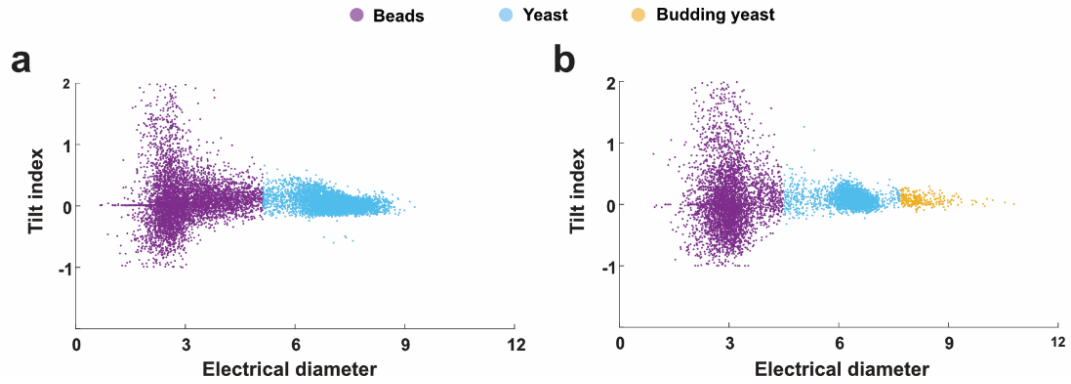

Figure 3.9: Scatter plot (electrical diameter vs tilt index) of single cell detection (a) signals from electrodes with 5 µm gap scatters; (b) signals from electrodes with 5 µm gap scatters.

3.3.5. Summary

In summary, a small electrode gap in impedance cytometry can enlarge the strength of electric field and increase the current density near the channel bottom. Target objects pass through the strengthened electrical field area, allowing to generate larger impedance pulses than normal. This feature could facilitate the detection of small objects (e.g., ~ 1 µm diameter, like bacteria or exosome) via the impedance detection with enhanced sensitivity. The only disadvantage of this method is the difficulty in fabrication, and in this work, the femtosecond laser was employed to fabricate the 1 µm electrode span with high success ratio, and avoid using the expensive and complex instruments and processes of lithography.

The high sensitivity of impedance cytometry enables the discrimination of similar objects with small differences. For example, I employed the enhanced impedance cytometry to discriminate the budding yeast cells from normal ones in my experiments. This work provided a new path to

improve the detection sensitivity of the impedance cytometry and prepare for the application in submicron and nano-scale detection.

3.4. Improve the sensitivity by viscoelastic focusing

The previous research conducted in section 3.3 aimed to enhance the sensitivity of impedance flow cytometry by increasing the strength of the electric field, thereby improving the amplitude of the impedance signal. The simulation results presented in section 3.3.3 and the experimental findings discussed in section 3.3.4 both demonstrated that the height of particles or cells in the channel has a significant impact on the amplitude of the impedance signal. When particles or cells are closer to the electrodes, the amplitude of the signal is higher, while being farther from the electrodes leads to a lower amplitude. This distribution in height results in a wide range of amplitudes, which weakens the sensitivity (revolution) of impedance detection. As the position of objects can affect the amplitude distribution, the focusing of objects can help to diminish the error caused by the position differences. To address this issue, a similar approach used in section 2.3 can be employed, namely hydrodynamic focusing. Hydrodynamic focusing allows for the alignment of cells or particles near the optical focal plane, which in turn helps control their vertical distance from the bottom of the channel. In my impedance flow cytometry setup, where the electrodes are fabricated on the bottom of the channel, implementing vertical focusing of particles or cells can help mitigate the sensitivity problem. Given that the velocity of my impedance flow cytometry experiments is not excessively high (less than 10 m/s), hydrodynamic focusing achieved through a two-layer channel configuration can provide effective vertical focusing. This method ensures that the particles or cells remain in close proximity to the electrodes, optimizing the sensitivity of impedance detection in my experiments. Fortunately, the horizontal connecting

structure can help to carry the viscoelastic focusing to force cells moving at a stable trajectory[136]; with the high pressure tolerance of horizontal connecting chip, the mass concentration can set very high[63].

In this study, viscoelastic fluid is utilized to facilitate the movement of cells and create a conductive environment for impedance detection. A relatively high mass concentration of 5,000 ppm is employed, which is often considered high for most applications involving viscoelastic fluids. The effects of viscoelastic focusing are then investigated at different velocities ranging from 3.7 mm/s to 2.368 m/s.

3.4.1. Experiments preparation

3.4.1.1. Viscoelastic solution (PEO medium) preparation

For further use, I firstly prepare the PEO solution with mass concentration of 10,000 ppm (1 wt%). Dissolve the PEO powder (molecular weight Mw of 600 kDa, 182 028, Sigma-Aldrich, St. Louis, MO) in 1× PBS solution. For better dissolution and avoiding PEO powder aggregates, the tube containing the PEO solution was shaken 12 hours at 23 °C by a triple shaker (NR-80, TAITEC Ltd., Japan) at 150 revolutions per minute (rpm).

Before experiments, the PEO solution with mass concentration of 10,000 ppm will be diluted to 5,000 ppm with 1× PBS solution.

3.4.1.2. Microfluidic chip

As the viscoelastic solution of PEO has the higher viscosity which makes it hard to drive. The chips for viscoelastic focusing are all fabricated with the horizontal connecting structure which is mentioned in section 2.2.3. The microchannel was fabricated by casting mixed PDMS (SYLGARD

184, Dow Corning, Midland, MI, USA) on SU8 (MicroChem Corp., Newton, MA) mold by common soft lithograph. The electrodes which conclude two layers, about 70 nm thick chromium (Cr) on glass and 70 nm thick gold (Au) on chromium, are all fabricated by photolithograph and wet-etching. The chip is assembled with two turns of plasma treated bonding, with resin sealing the PDMS and stainless-steel capillary connections.

The width and height of microchannel is 30 μm and 15 μm, respectively. And the length of microchannel for focusing is just 3 mm. Fig.3.10 shows the electrode and microfluidic chip, the horizontal connecting structure allows chip minimization, electrodes and chip can both designed in a quite small area.

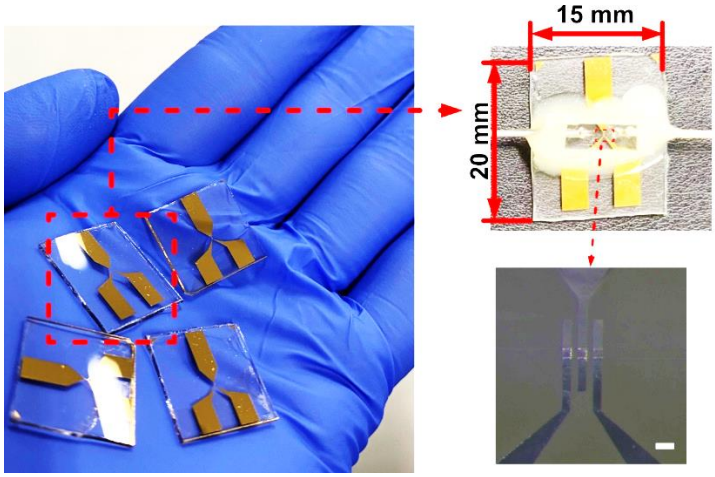

Figure 3.10: The electrodes and microfluidic chip; left: glass with electrodes; right top: the microfluidic chip with the size of 15 mm × 19 mm; the detail of electrodes, scale bar: 60 μm.

3.4.2. The viscoelastic focusing of particle

The inertial focusing is considered as the most simply way to make cell moving in a stable trajectory; however, the efficiency of inertial focusing is low due to the number of equilibrium positions and invalidation under high Re. To improve the focusing effect, replace the Newtonian fluid with viscoelastic fluid can help to decrease the equilibrium positions. Like shown in Fig.3.11a,

there are four equilibrium positions in inertial focusing while only one in viscoelastic focusing for square cross-section[137], which is always mentioned in section 1.2.1; and two equilibrium positions in channel with rectangle cross-section for both focusing. As impedance flow cytometry with coplanar electrodes can achieve better sensitivity and accuracy when cells or particles have the same distance to the electrodes, the viscoelastic focusing can be applied on the channel with cross-section of rectangle. Fig.3.11b shows the viscoelastic focusing effect in channel 40 μm of height and width, the particles with diameter of 10 μm are moving along the same trajectory in the top view. However, as the side view of microchannel is hard to observe, the evaluation of vertical focusing will be carried by impedance flow cytometry.

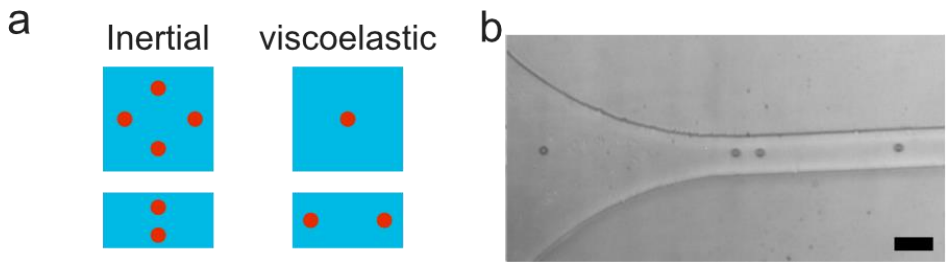

Figure 3.11: Viscoelastic focusing; (a) the difference between inertial focusing and viscoelastic focusing, the blue rectangles and red circles represent the cross-section of channel and the equilibrium positions, respectively; (b) Particles with diameter of 10 μm under viscoelastic focusing in channel, the cross-section of channel is square with 40 μm side, scale bar 40 μm.

3.4.3. The impedance detection of particle with viscoelastic focusing

The viscoelastic focusing technique can theoretically maintain particles at a stable height within a microchannel, with a specific amplitude corresponding to their diameter. In the experiment, a channel with a width of 30 μm and a height of 15 μm is used. This channel geometry allows for the existence of two equilibrium positions located at half the height of the channel, near the two side walls. In this particular experiment, polystyrene (PS) beads with diameters of 6 μm

and 10 µm are mixed in a viscoelastic solution consisting of 1×PBS and 5,000 ppm of polyethylene oxide (PEO).

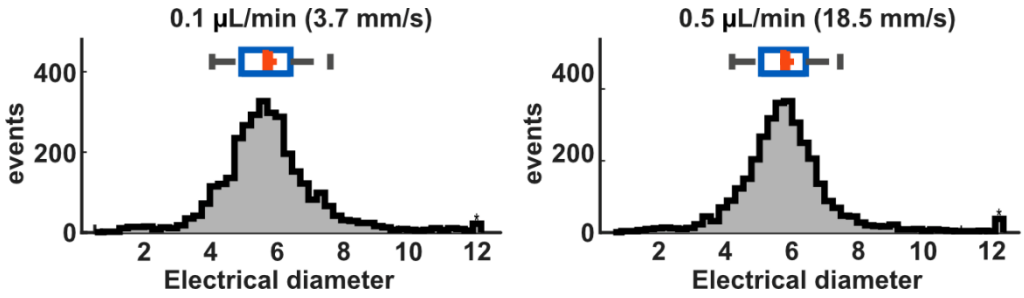

Figure 3.12: Electrical diameter of PS beads with the flow rates of 0.1 µL/min and 0.5 µL/min, respectively.

In Figure 3.12, the impedance detection of particles is illustrated at different flow rates: 0.1 µL/min (velocity of 3.7 mm/s), 0.5 µL/min (velocity of 18.5 mm/s), 2 µL/min (velocity of 7.4 cm/s), and 8 µL/min. At the lowest flow rate of 0.1 µL/min, the majority of the signals correspond to the 6 µm beads, and the distribution of electrical diameter is quite wide, ranging from 4 µm to 8 µm. As the flow rate is increased to 2 µL/min, the distribution of the 10 µm beads becomes more apparent in Figure 3.13. Additionally, the probability distribution of the 6 µm beads becomes more concentrated at this flow rate. At a flow rate of 8 µL/min, the distribution of the 10 µm beads is even more prominent, as shown in Figure 3.13. However, the distribution of the 6 µm beads becomes wide again. These observations highlight the influence of flow rate on the distribution and detection of different bead sizes in impedance flow cytometry. Comparing the distribution with 2 µL/min and 8 µL/min, the distributions of the two beads are similar in general; but the distribution of 10 µm beads is more concentrated at 8 µL/min which can be clear observed by the probability distribution.

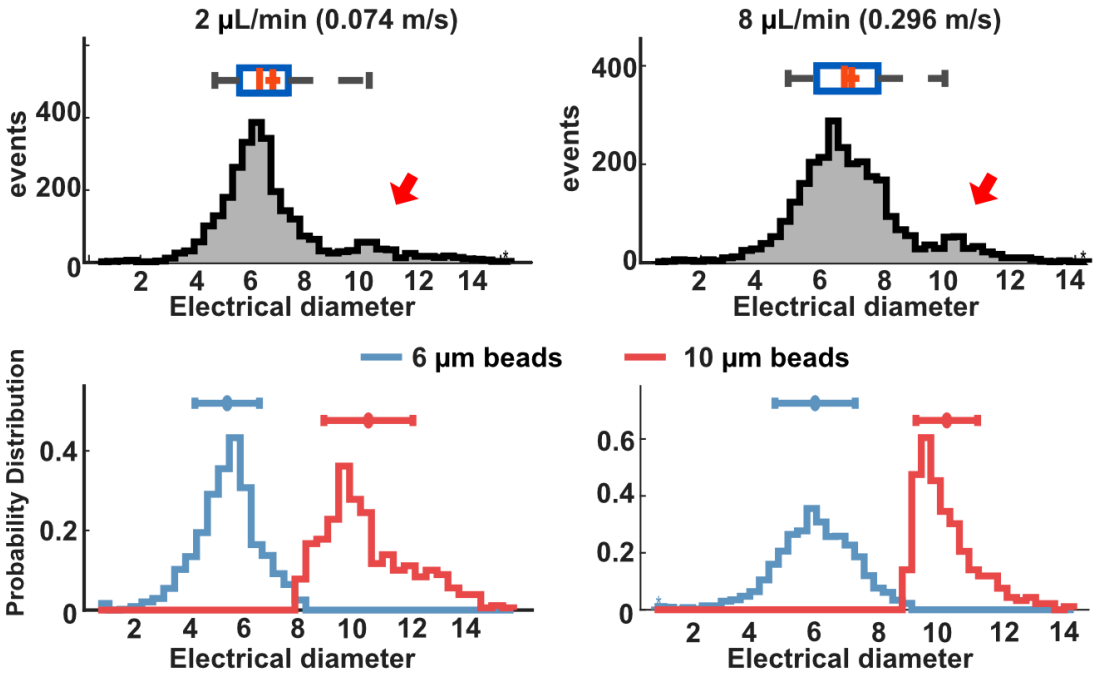

Figure 3.13: Electrical diameter of PS beads with the flow rates of 2 µL/min and 8 µL/min, respectively

As the flow rate continues to increase, some new phenomena emerge in the distribution of electrical diameter. On the left side of the 6 µm beads distribution, there are more signals with small amplitude compared to lower flow rates. When comparing the results in Figure 3.13 and Figure 3.14, the amplitude distribution and probability are quite similar, indicating that the viscoelastic focusing technique does not show improvement under high flow rates or velocities. This observation suggests that at higher flow rates, the performance of viscoelastic focusing may be limited, and other factors or mechanisms may come into play that affect the distribution of electrical diameter in impedance flow cytometry, like channel deformation at high velocity which can make more equilibrium positions.

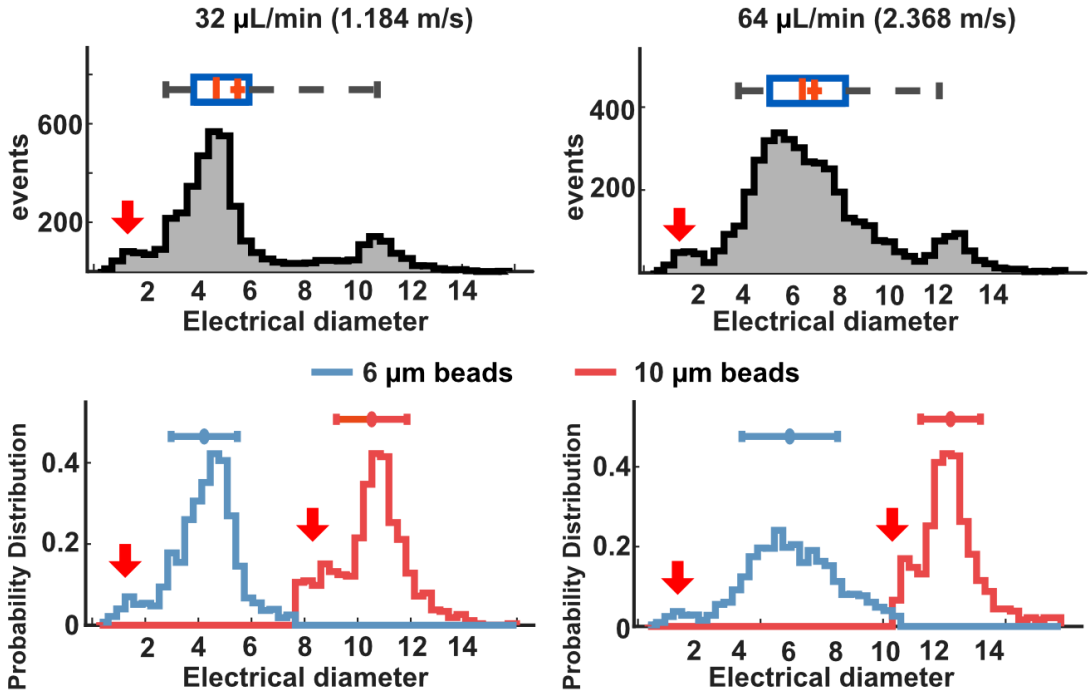

Figure 3.14: Electrical diameter of PS beads with the flow rates of 32 µL/min and 64 µL/min, respectively.

However, the small difference in the low amplitude area indicates that there may be more beads moving far from the electrodes. Considering the high velocity of the flow, the most likely reason for this phenomenon is the deformation of the channel under such high velocities. The deformation causes the originally rectangular cross-section to transform into a more complex shape with an arched top, which introduces an additional equilibrium position for the beads[138].

3.4.4. Summary

In this section, my main focus was on studying the influence of velocity on viscoelastic focusing. I observed that viscoelastic focusing only occurs at sufficiently high flow rates. However, I also encountered the issue of unexpected channel deformation at high flow rates, which disrupts the trajectory of particles. Based on current data, the flow rate ranging from 2 µL/min and 8 µL/min

can divide the distributions of two beads which achieve the purpose to decrease the error from position. Further research is needed to explore the effects of other factors, such as the mass concentration of the viscoelastic fluid, as well as the trajectory of particles in channels of different lengths. By conducting more in-depth investigations, I can gain a better understanding of viscoelastic focusing and optimize its application in microfluidic systems.

3.5. The droplet measurement by impedance flow cytometry

The impedance detection of droplets follows a similar principle to that of single cells. The width of the impedance signal on a timescale can provide information about the length and volume of the droplet[139], [140], Additionally, variations in the waveform can indicate the presence of cells within the droplet[141], [142]. In most cases, droplets are generated in a long-slug shape, while the electrodes used for impedance detection are relatively short compared to the droplet. In this scenario, the commonly used differential signal of impedance cytometry will produce two opposing peaks with a distance that is related to the length of the slug-shaped droplet. To achieve accurate droplet measurement, adjustments to the electrode layouts and the droplet generation process are necessary.

3.5.1. The theory of droplet impedance measurement

In impedance flow cytometry, I use two pairs of positive and negative electrodes, with the positive electrode serving as the shared electrode. The signals from the two negative electrodes are detected. When a droplet passes through the two electrode gaps at different times, there will be a time difference between the two droplet signals. In cell impedance analysis, the signal of interest

is the differential signal, where one cell produces two peaks with inverse amplitudes. Each peak reflects cell information such as volume or shape, and the time difference between the signals from the two electrode gaps is usually ignored. However, in the case of droplets, their larger size compared to cells and even the electrodes make the time difference non-negligible. As shown in Fig.3.15, droplet 1 and droplet 2 pass through the electrodes one after the other with a constant interval, and the peaks of the two signals (V_1 and V_2) also have the same interval. However, in the differential signal (V_1-V_2), if the time difference and the interval are set appropriately so that the peaks in V_2 align with the interval range in V_1, the inverse peaks of a droplet in the differential signal will remain intact and can be analyzed in a similar manner to cells. Theoretically, only one pair of electrodes will have no need to concern about the situations of different size of electrodes and droplets, but the differential signal by two pair of electrodes can which eliminate the system error and output the more accurate relative signal.

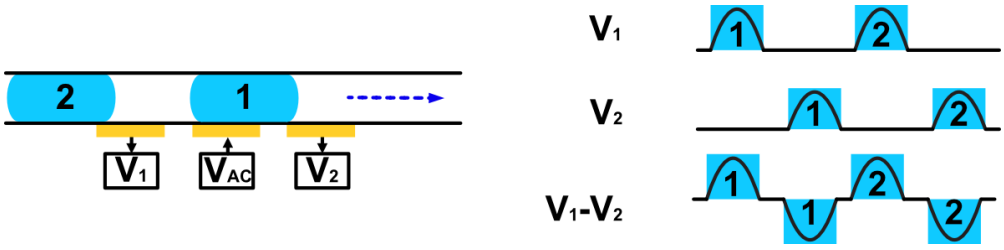

Figure 3.15: Droplets and the relative signals

Obviously, the length of the droplet and the length of the middle electrode (V_{AC} in my experiments) directly influence and determine the resulting signals, leading to four distinct situations. These situations are depicted in Fig.3.16 and are determined by two conditions: the relationship between the length of the droplet (L_D) and the length of the middle electrode (L_E), and the relationship between the interval of the droplets (I_D) and the length of the middle electrode (LE). Regardless of the specific waveform details, the parameters of droplet generation such as L_D

and I_D can still be measured based on the waveforms observed in all four situations. These parameters are indicated on the graphs for reference.

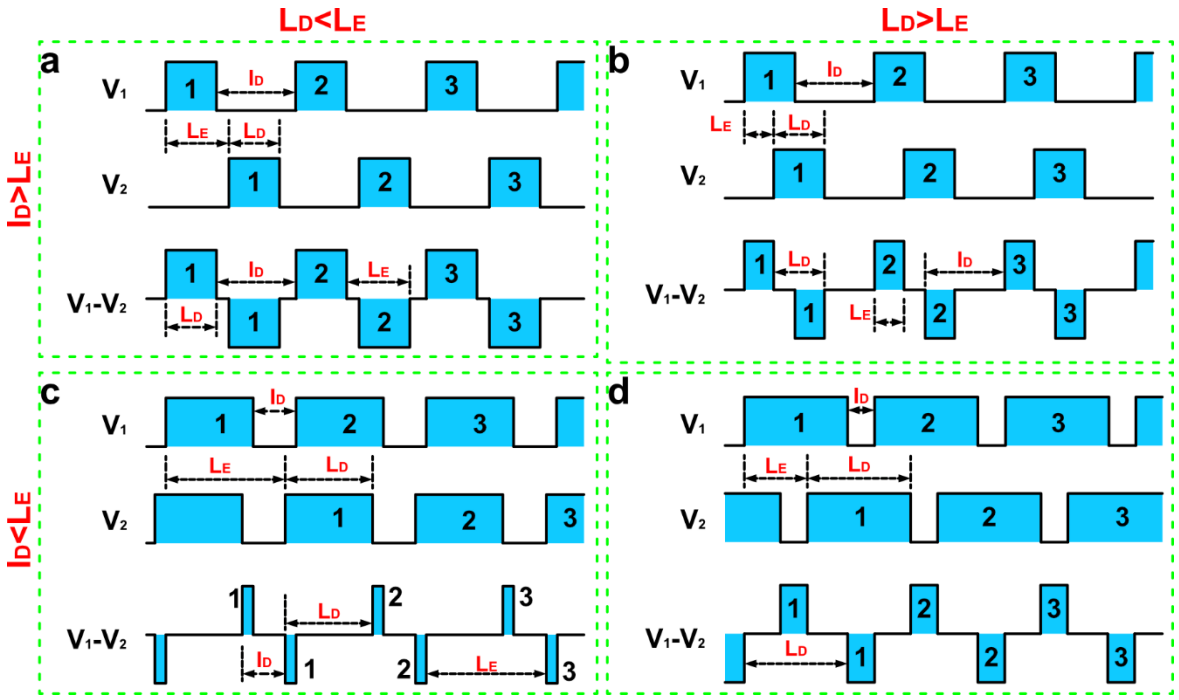

Figure 3.16: The signals of V_1, V_2, and the differential signal (V_1-V_2) correspond to different conditions involving the length of droplet (L_D), length of middle electrode (L_E), and the interval of droplets (I_D); resulting in four situations: (a) $L_D<L_E$, $I_D>L_E$; (b) $L_D>L_E$, $I_D>L_E$; (c) $L_D<L_E$, $I_D<L_E$; (d) $L_D>L_E$, $I_D<L_E$.

3.5.2. Simulation of droplet impedance detections

The droplet in simulation of impedance detection is defined as an undeformed material, not fluid. The displacement of droplet is realized by integrate the results at different position. Fig. 3.17 shows the two methods to describe the droplet, the first is to define the droplet by a function of the material in all field (3.17b); the other is to draw the geometry of droplet (3.17a).

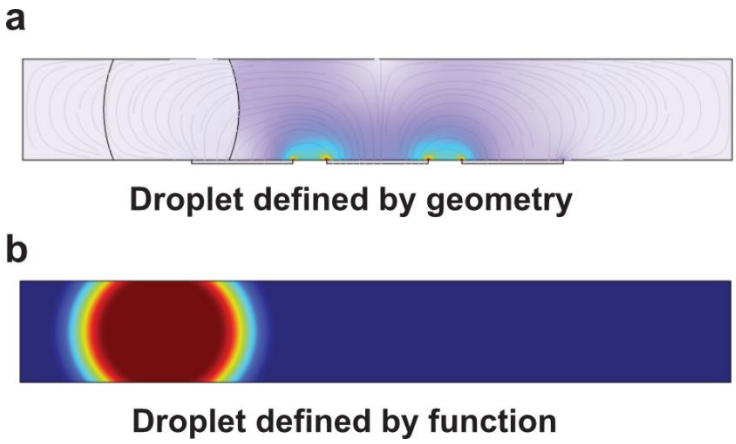

Figure 3.17: The two methods to describe droplet in simulation of impedance detection, (a) the geometry definition, the color represents the current density but no specific meaning in this graph; (b) the material function definition, the red means the water material while the blue means the oil.

The simulation results by these two droplets describe methods are quite similar, only a small difference in details. Fig.3.18 shows the simulation results with the two kinds of droplet descriptions, the three electrodes are all 30 μm wide while the gaps are 10 μm wide. The geometric droplet is clearly displayed on the results; but as the boundary of droplet and the wall of electrodes may be overlapped in one moment, the electrodes in geometric droplet simulation should be define in volume, not boundary. On the other hand, as the interference of function defined droplet should have a thickness to keep continuity in FEM, the simulation results will be a little inaccurate than geometric droplet; as the Fig.3.18b shows, the impedance signal from geometric droplet model can reflect more details.

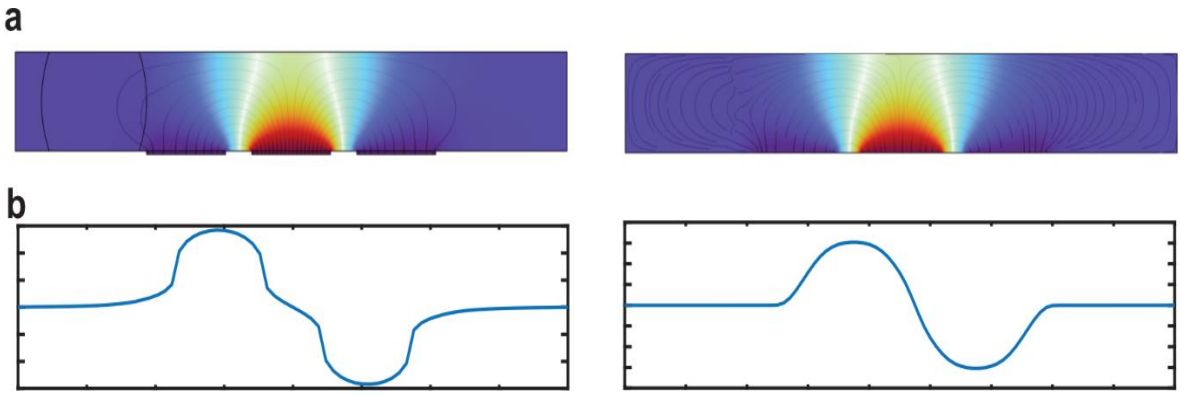

Figure 3.18: The simulation results with two droplet descriptions, (a) electric field distribution, left is geometric droplet while right is function droplet, the color represents the voltage distribution with red and blue means the high voltage and low voltage, respectively; (b) the impedance signal of droplet, left is geometric droplet while right is function droplet.

Based on the geometric droplet methods, the simulations of the four situations are carried:

3.5.2.1. Case one: $L_D<L_E$, $I_D>L_E$

In this situation, the middle electrode is wider than the length of droplet ($L_E > L_D$), while the interval is longer than the droplet ($I_D>L_E$). As Fig.3.19 shows, V_1 and V_2 are the voltage signals from the two ground electrodes, Diff is the differential signals means V_1-V_2; in this situation, as the middle electrode is longer than the droplet ($L_E>L_D$), the two waveforms of the same droplet will have no overlap area on time scale; as the interval is wider enough to cover the droplet signal, there will be no overlap are between two different droplets. Then, the differential signal can directly reflect the intact waveform of every droplet.

In this situation, the width of every peak in the differential signals can directly reflect the length of droplet, and the shape of waveform can also reflect the shape of droplet. No information is missing on the waveforms of droplet, and this is the only way to realize nondestructive detecting of droplet.

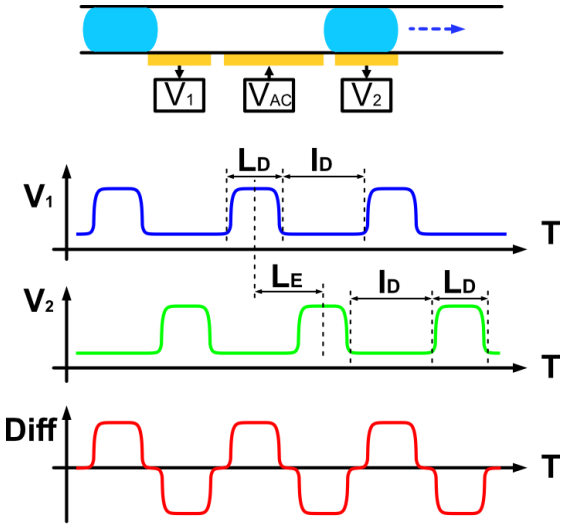

Figure 3.19: Numerical result of impedance signals in situation of $L_D<L_E$, $I_D>L_E$.

3.5.2.2. Case two: $L_D>L_E$, $I_D>L_E$

This situation is the most common situation, small electrodes detect large droplet; As Fig.3.20 shows, the middle electrode is shorter than the droplet ($L_E<L_D$), and the long interval has no effect to separate the waveforms of V_1 and V_2 in this situation. The yellow marked area is the overlapped part of V_1 and V_2, which can hide some information of droplet.

In this situation, as the peaks of droplet are partly dissolved by differential amplifier, the width of every peak cannot reflect the size of droplet.

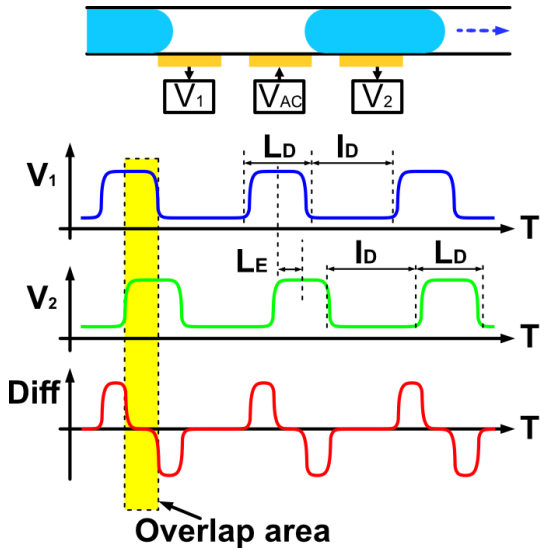

Figure 3.20: Numerical result of impedance signals in situation of $L_D>L_E$, $I_D>L_E$; the yellow marked area represents the signal overlapped part.

3.5.2.3. Case three: $L_D<L_E$, $I_D<L_E$

Once if the interval of two droplets is too small, the distance between peaks will be smaller, causing the differential signal partly dissolved. On contrary with the second situation that the overlap part results by the signals of the same droplet; in this situation, the dissolve part of differential signal is generated by the different droplets; the previous droplet has not totally passed the rear electrode but the following droplet enter the detection area of front electrode.

The short interval makes the signal hard to distinguish which peaks are from the same droplet. But if the interval is smaller than the length of droplet, the results will be similar to situation one, just consider the interval as the droplet.

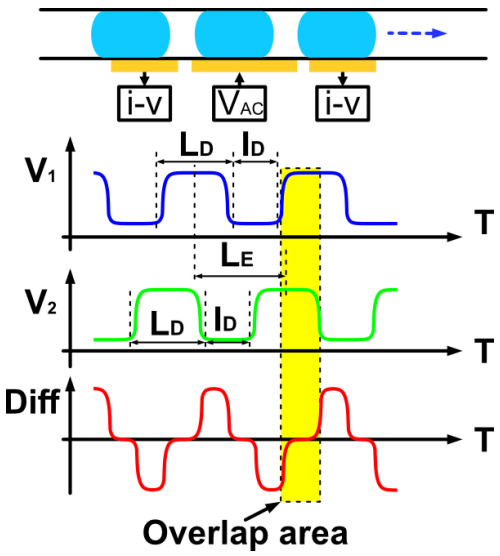

Figure 3.21: Numerical result of impedance signals in situation of small droplet, short interval and long electrode; the yellow marked area represents the signal overlapped part.

3.5.2.4. Case four: $L_D>L_E$, $I_D<L_E$

In this situation, when the interval is the smallest size, like shown in Fig.3.22; this situation can be considered as the contrary situation of situation one; just consider the interval as the droplet

and the droplet as the interval. This situation can be analysis like situation one, but as the part of waveform of droplet is still overlapped, there will still be some information lost.

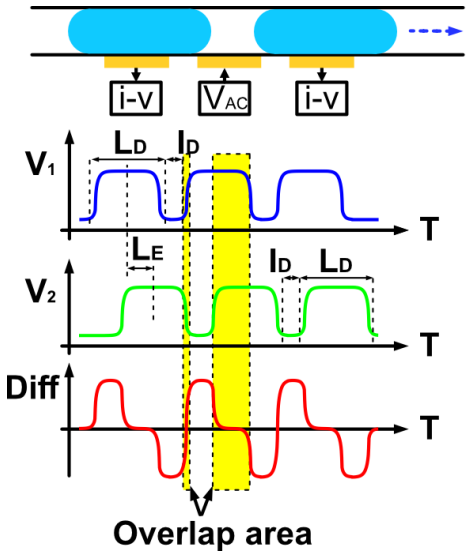

Figure 3.22: Numerical result of impedance signals in situation of large droplet, short interval and short electrode; the yellow marked area represents the signal overlapped part.

3.5.3. Experiments preparation

3.5.3.1. The preparation of continuous phase

The continuous phase in my experiments is the mineral oil (M5904) mixed with the surfactant (Span80, Sigma-Aldrich). The mass concentration is 3 % v/v; as the viscosity of surfactant of Span80 is quite high, there will be a lot of bubbles generated during mixing, the mixed mineral oil should be vacuumed for 30 minutes.

3.5.3.2. Chip fabrication

The microfluidic chip is fabricated with the methods mentioned in section 2.2.3, the horizontal connecting chip for high pressure tolerance; firstly, bonding the channel which is fabricated by casting mixed PDMS (SYLGARD 184, Dow Corning, Midland, MI, USA) on SU8 (MicroChem

Corp., Newton, MA), on the glass with electrodes and then bonding the other surface with glass to seal chamber. The electrodes are fabricated by lift-off technology, which conclude two layers, about 70 nm thick chromium (Cr) on glass and 70 nm thick gold (Au) on chromium.

Comparing to cell detection, droplet has the larger size and the measurement is based on the distance on time scale, so the amplitude of signals of droplet measurement is not as important as cell detection. For the electrodes, two types of electrode groups are designed; the first is the wide middle electrode which is 180 μm wide while the other is 30 μm wide; the gaps of electrodes are both set as 10 μm. As the gap realize the impedance detection in practice, the two side electrodes have no demand in design.

Fig.3.23 shows the microfluidic chip and the electrodes, the main channel is 80 μm wide and 30 μm high, include the droplet generation junction (T-junction) and the impedance detection, the curves of channel is used to maintain the pressure near T-junction for stable droplet generation. In bonding process, the electrodes should set near the outlet where the pressure is low; the low pressure can avoid the potential leakage in channel and prevent the invalid due to the leakage.

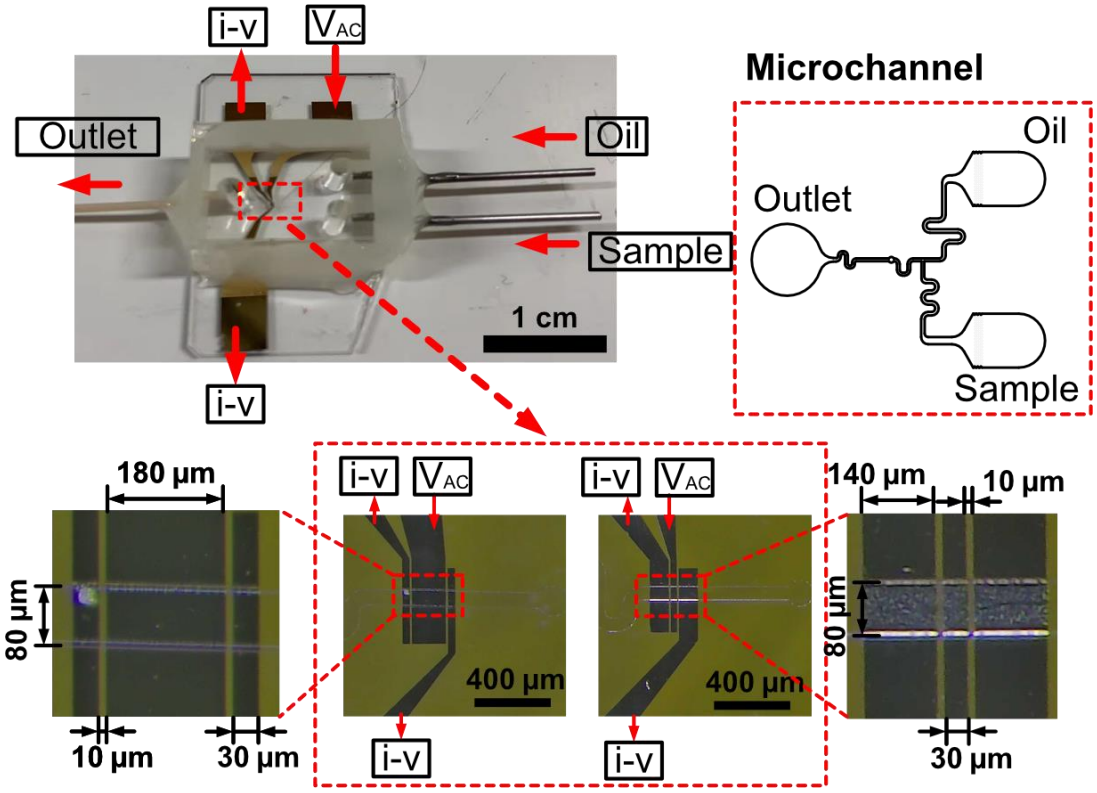

Figure 3.23: The microfluidic chip of impedance flow cytometry with coplanar electrodes for droplet measurement; two kinds of electrodes are fabricated, L_E=180 µm and L_E=30 µm, the gaps are both 10 µm.

3.5.4. Droplet measurement with impedance cytometry

Based on the four previously discussed situations, the measurement of droplets can be accomplished regardless of the specific situation by adjusting the calculation method. For example, the length of the droplet can be measured by calculating the distance between the front of two relative peaks, as shown in Figure 3.16. However, it's important to note that real signals may differ from simulations because the droplet in the actual situation may not completely fill the cross-section of the channel. Due to factors such as surface tension and velocity distribution, the droplet often exhibits a hemisphere head, slug body, and narrowing tail, particularly in the case of long droplets. To demonstrate this, I present measurements of two different situations in Figure 3.24:

one with $L_D<L_E$, $I_D>L_E$ (L_D=122 μm, I_D=415 μm) and the other with $L_D>L_E$, $I_D<L_E$ (L_D=235 μm, I_D=204 μm). The middle electrode has a width of 180 μm, and the gaps are 10 μm wide. The length and interval of the droplets are controlled by adjusting the flow rates of the separation phase and continuous phase. The results of the simulation and detection shown in Figure 3.24a exhibit minor differences, mainly in the details of the waveform. As mentioned earlier, these differences arise from the complexity of the real droplet behavior, which includes factors such as surface tension. However, the general waveforms of the simulation and detection are similar. In both situations, the length of the droplet (L_D) can be obtained by calculating different parts of the waveform. For example, the width of a single peak can reveal the length of the droplet in the $L_D<L_E$, $I_D>L_E$ condition. In the $L_D>L_E$, $I_D<L_E$ condition, the length can be indirectly measured by subtracting the length of the electrodes from the length between the two opposing and contacting peaks. Based on the measurements, the distribution of amplitude and the measured length of the droplets are shown in Figure 3.24. Due to the surface tension which is shown in Fig.3.24c, the surface tension tends to make the curved edge of the droplet, it is difficult for small droplets to completely occupy the channel, resulting in a thicker oil layer surrounding the droplet; while large droplet with slug shape can make more volume and interface connecting with the coplanar electrodes on bottom of channel. This higher resistance and lower amplitude are observed for small droplets. Additionally, the distribution of peak amplitude shows that the smaller droplets are more concentrated compared to the longer droplets.

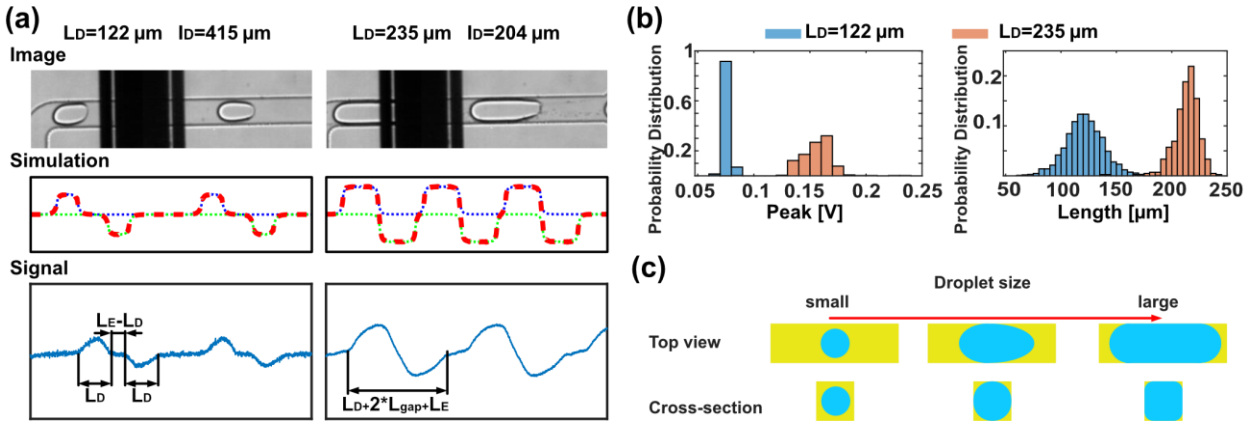

Figure 3.24: Results of simulation and experiments in conditions of $L_D<L_E$, $l_D>L_E$ (left) and $L_D>L_E$, $l_D<L_E$ (right). (a) Signals of simulation and detection; (b) probability density function ((PDF)) of peak amplitude and the length of droplet (L_D); (c) Droplets with different size will have different distribution in cross-section.

The length of the droplets in the recorded signals is determined by the width of a single peak in time. By calculating the total flow rates and the cross-section of the channel, the practical length of the droplet can be obtained. If the length of the droplet (one peak) is smaller than 180 μm, it is considered as the length of the droplet. Otherwise, the real size is calculated using the length of the electrodes and gaps. Figure 3.25 illustrates the measurements of droplets with a constant flow rate of the continuous phase (Q_c=20 μL/h) and different flow rates of the separation phase (Q_s=4 μL/h, 10 μL/h, and 20 μL/h). In the original impedance signals shown in Figure 3.25a (the red dotted box represents the waveform of each individual droplet), it is evident that the small droplet (Q_s=4 μL/h) exhibits two opposite and intact peaks, while the droplets in the Q_s=10 μL/h and Q_s=20 μL/h conditions have a direct slope between the two peaks. This indicates that only the droplet with Q_s=4 μL/h is smaller than the 180 μm wide middle electrodes. Furthermore, the data reveals that the small droplet has the lowest amplitude of the peak. Additionally, the signal noise of the small droplet is more pronounced due to the thicker oil layer, which worsens the signal-to-noise ratio (SNR). The poor SNR can hinder the measurement of small droplets, especially those smaller than the channel width. The probability density function (PDF) of the peak amplitude

shown in Figure 3.25b indicates that some peak amplitudes of the small droplet can even approximate zero, making it challenging to detect the small droplet. Since no reference is added in the detection, the peak amplitude can only reflect the distribution of droplets in the cross-section of the channel and does not reveal any physical parameters, such as cell size in cell impedance analysis. The probability density function of the droplet length (L_D) in Figure 3.25b demonstrates that the lengths of droplets for Q_s=4 µL/h, 10 µL/h, and 20 µL/h are approximately 95 µm, 230 µm, and 350 µm, respectively.

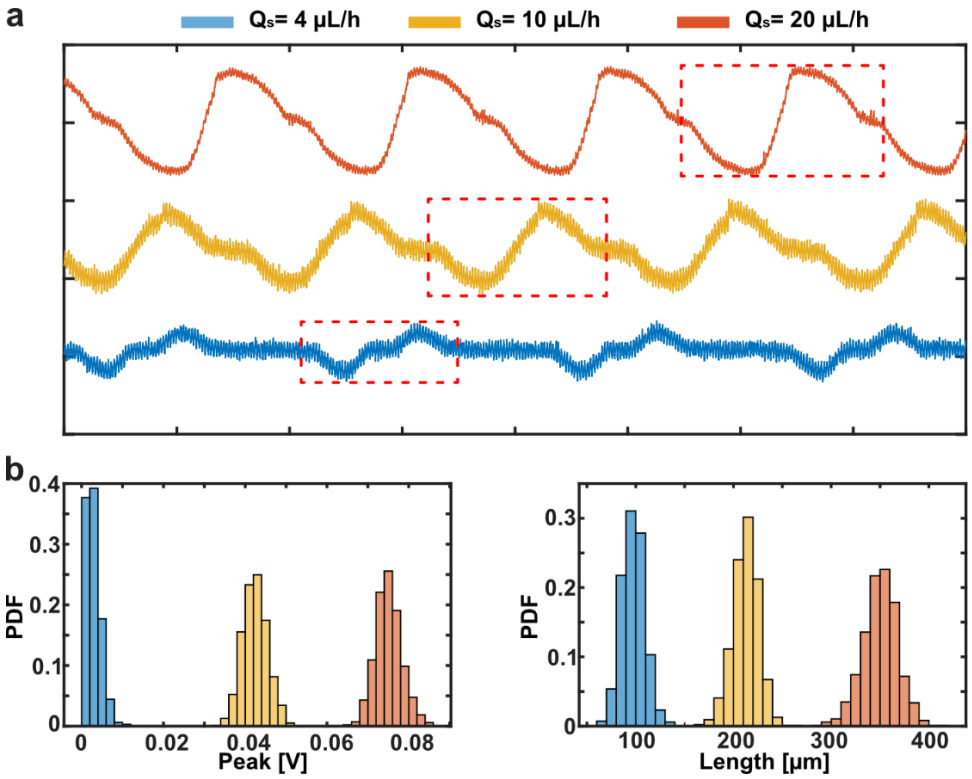

Figure 3.25: Results of droplet measurement with different flow rates of separation phase (Q_s=4 µL/h, 10 µL/h and 20 µL/h) by 180 µm wide middle electrodes and 10 µm gaps; (a) Original signals of droplet impedance, dotted boxes mark the signal of single droplet; (b) Probability density function (PDF) of peak amplitude (left) and probability density function (PDF) of the length of droplet (right).

Although the condition of $L_D<L_E$, $I_D>L_E$ can support intact waveform detection of droplets, the more common condition is $L_D>L_E$, $I_D>L_E$, where the droplet and interval are both longer than

the electrodes. Figure 3.26 illustrates the results of droplet measurement with Q_c=20 µL/h and Q_s=8 µL/h and 20 µL/h using 30 µm wide middle electrodes. When compared with the results obtained from 180 µm wide electrodes, both the peak amplitude and length of the droplet exhibit wider distributions. The measured lengths of the droplets are approximately 220 µm with Q_s=8 µL/h and 350 µm with Q_s=20 µL/h. Although the measurement results from both types of electrodes appear similar, the results from the wider middle electrodes are more accurate due to the concentrated distribution. This is primarily attributed to the shape of the droplet. As mentioned earlier, a slug-like droplet has a hemisphere head, which means the signal from the head of the droplet has lower amplitude and higher noise. If the length of the head is longer than the middle electrodes, the two detected signals will overlap with poor signal-to-noise ratio, which can affect signal analysis. Therefore, the length of the electrodes can be designed to be longer based on the droplet under measurement.

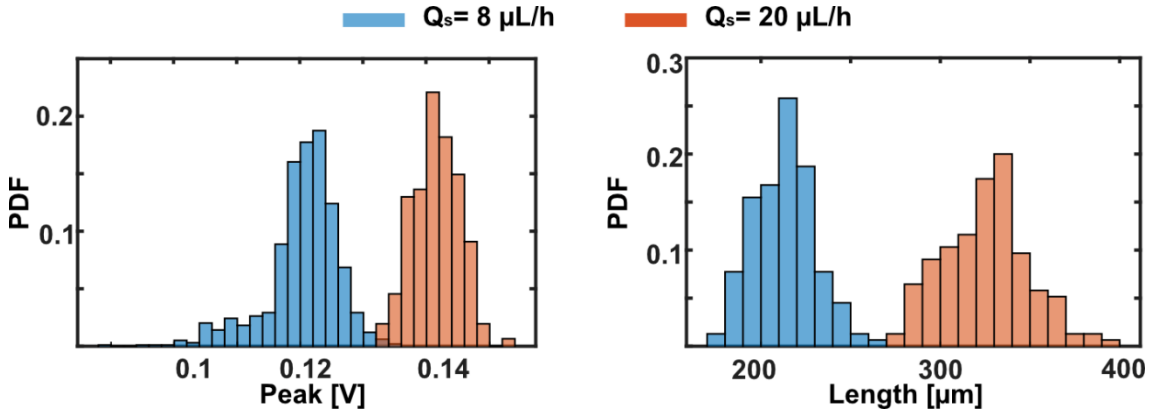

Figure 3.26: Results of droplet measurement with Q_s=8 µL/h and 20 µL/h by 30 µm wide middle electrodes and 10 µm gaps; left: Probability density function of peak amplitude, right: probability density function of the length of droplet.

3.5.5. Droplet impedance by one pair of electrodes

For most cell and droplet impedance detection, differential signal is the most popular way to get the expect signals for analysis of cell or droplet. However, as cells are smaller than electrodes, the waveform of cell is always intact, while droplet is on the contrary; except situation of $L_D<L_E$, some information of droplet will be lost with the differential signal. For example, Fig.3.27 shows the original signals of a droplets with strange shape, which is directly detected by one pair of electrodes. This waveform is quite hard to be observed by differential signals. This signal can well reveal the shape of droplet, as the strange droplet includes the head, body, tail and the end; the waveform shows the amplitude of head raising rapidly and turn plat on body period, for the dwindling tail the amplitude decrease slowly and drop in the end.

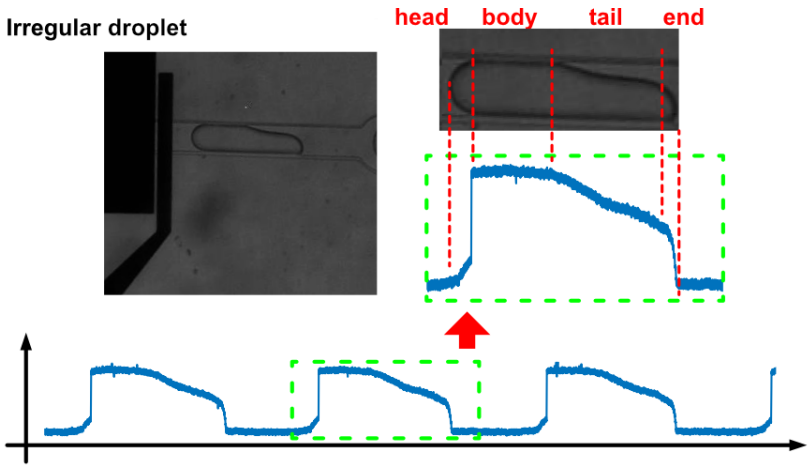

Figure 3.27: The irregular droplet and the related signal.

In addition, this kind of signal also has the potential to reflect the cell or particle in droplets. Like shown in Fig.3.28, the particle in droplet can increase the local resistance in droplet, and there will be a plummet on the waveform of droplet. However, this detection of particle or cell in droplet only works when the droplet is long or big enough to fulfil the cross-section of channel which bring a good SNR; or the signal of particle will be covered by noise or the waveforms of head or end of small droplet.

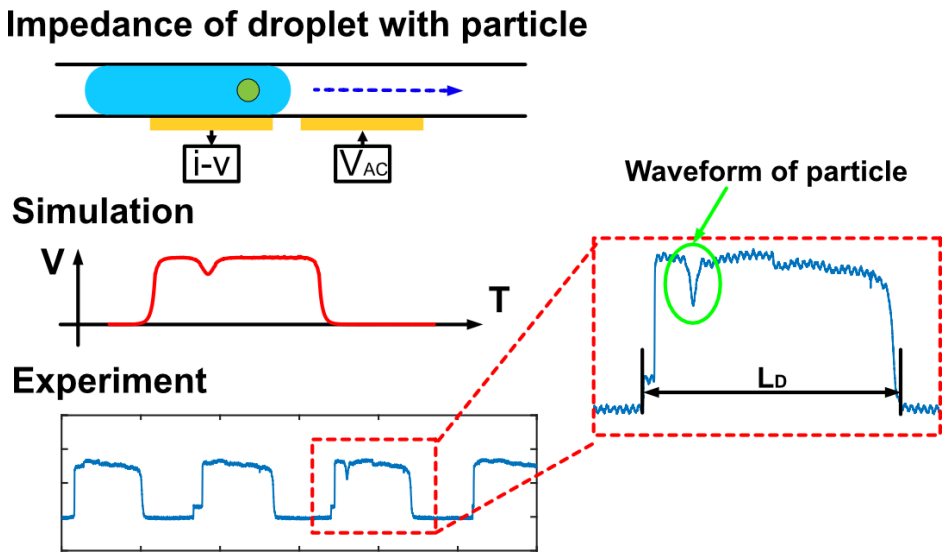

Figure 3.28: The simulation and experiment results of particle in droplet.

3.5.6. Summary

In this section, I conducted simulations to analyze the different scenarios of droplet detection. Based on my estimations of the relationships between three key sizes - the size of the middle electrode (L_E), the size of the droplet (L_D), and the interval between droplets (I_D) - I were able to categorize the findings into four distinct situations. Among these situations, I found that only when L_D is smaller than L_E and I_D is greater than L_E, the waveform of the droplet remains intact without any overlapping areas. This implies that only in this specific situation can the waveform of the droplet be used for further analysis, such as shape characterization or other properties. Furthermore, through simulations and experiments, I discovered that longer middle electrodes offer improved detection accuracy due to the increased space available for distinguishing the signals from the two pairs of electrodes. This enhanced accuracy allows for direct observation of shape changes and the presence of particles or cells within the droplet. If there is a need to preserve these properties during impedance cytometry, a design incorporating long middle electrodes and the utilization of sheath

flow to increase the interval between droplets can satisfy the requirements of nondestructive testing. Additionally, the signal quality relates to the level of cross-section filling with conductive droplet, large droplet will have better SNR, which requires longer distance between two gaps and the droplets.

In summary, this section provides insights into the different scenarios of droplet detection through simulations and concludes that specific conditions, such as $L_D<L_E$ and $I_D>L_E$, yield intact waveform signals that are suitable for analyzing the shape and other characteristics of the droplets. Additionally, the use of longer middle electrodes enhances detection accuracy, enabling the direct observation of shape changes and the presence of particles or cells within droplets, based on the resistance difference solution and beads or cells.

4. The size-based passive sorting of droplets

4.1. The droplet-based cell sorting system

For cell sorting, methods are always classified into two kinds, passive methods and active methods. The passive methods always sort cells by physical properties like size[143]–[145], shape[146], [147] and density, which means the sorting efficiency relies on the uniformity of cells. Active sorting always needs much information to identify cells to trigger the sorting system to manipulate the target cells[148], [149], which means the active sorting will be quite complex and inefficient, and sometimes even need to mark cells. Moreover, it will be more changeable when sort small cells, due to the small tolerance for precious activation of acting force[150]. To realize precious sorting of small cells, researchers use large droplet to carry cells and manipulate the droplet, instead direct cell manipulation[151]–[153]. In active droplet manipulation, the dielectrophoretic (DEP) force is the most popular method[154]. Additionally, droplet can supply a closed culture environment which means cell sorting can be carried after grow cell for a time[155]. However, similar with cell active sorting system, the throughput will be limit by the active manipulate system. Therefore, combine the advantages of the passive and active sorting system could help to realize a high-throughput active droplet-based cell sorting.

Fig.4.1 shows the principle of my active droplet-burst and passive droplet-sorting system. This system contains four parts: droplet generation, cell detection, droplet burst and passive droplet separation.

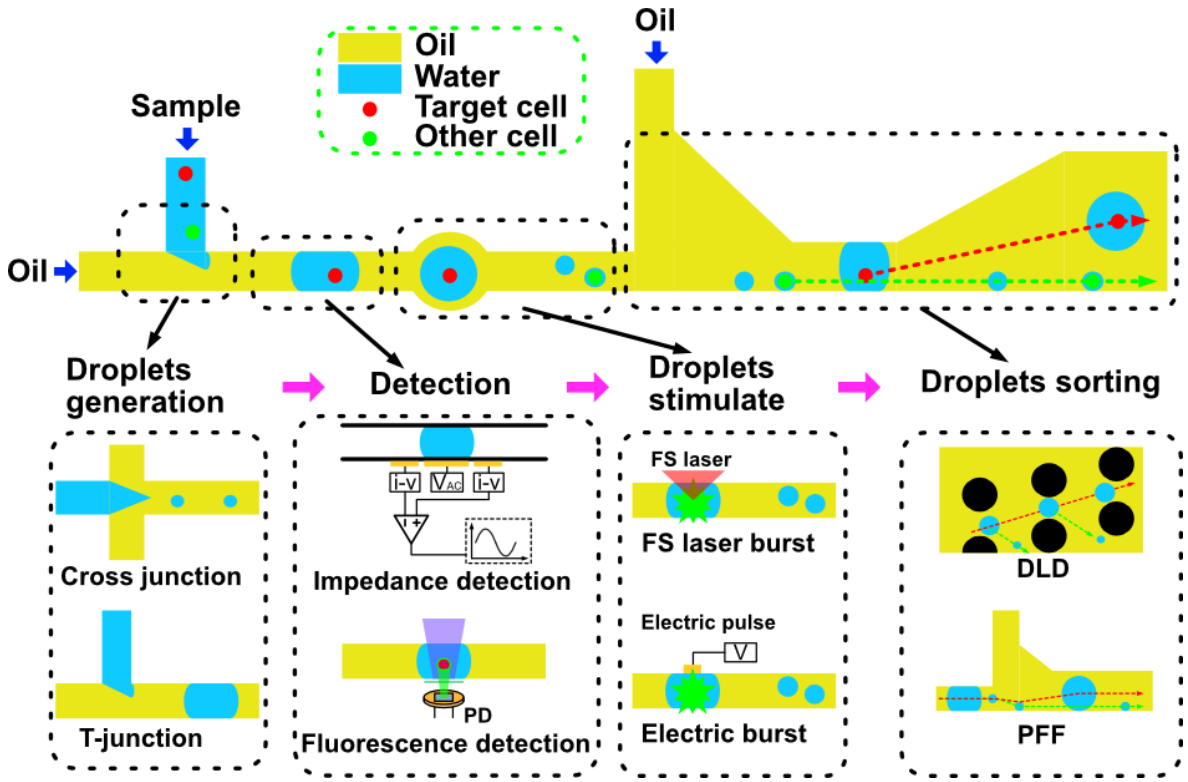

Figure 4.1: The basic construction of droplet-based cell sorting system.

The droplet generation is quite developed[156], the common passive structure will cross junction[157], [158] and T-junction[159]–[161] can all generate droplets efficiently. The detection of cell in droplet can use the impedance signal[162] or optical signal[153], these detection methods are well applied for triggering the active manipulation. The droplet burst process is mainly expected to break the droplet without target into small droplet for passive separation; femtosecond laser was verified feasible to evaporate water and generate bubble[150], [163], which can be applied to burst the droplet. As droplet can be burst to small size, the passive droplet sorting structure only need to separate droplet by size. The passive sorting structure can relate to the size-

based cell passive sorting structure like deterministic lateral displacement (DLD)[164]–[166] or pinched flow fractionation[167], [168].

To make the sorting system more feasible, it will be better if the passive droplet sorting can separate two droplets will small difference in size.

4.2. Theory and methods

4.2.1. Principle of pinched flow fractionation (PFF)

The principle of pinched flow fractionation is based on the properties of laminar flow. In laminar flow, streamlines move in the same direction and maintain their position within the cross-section of the channel. When particles of different sizes enter an extended channel after being arranged along the sidewall of a narrow channel, they become separated in the wider channel[169]. Since larger particles occupy a greater width within the channel, laminar flow causes them to move towards the centerline of the channel, while smaller particles follow the sidewall[170].

The principle can also be applied to size-based droplet sorting. Although droplets lack the stiffness to prevent deformation under the compression of the sheath flow, the surface tension within the droplets helps them regain their spherical or circular shape when not subjected to acceleration. Even if the droplets do not maintain a perfect circular shape during flow, they can still be separated based on differences in the distances from their barycenter to the channel wall.

The key factor in droplet separation is to amplify the difference in barycenter position between droplets. Figure 4.2b illustrates how the location of a droplet in a wide channel is influenced by its size and initial position in a narrow channel. In the narrow channel, two crucial sizes are the distance from the barycenter to the wall (D_n) and the channel width (W_n). Similarly, in the wide channel, the corresponding sizes are the distance from the barycenter to the wall (D_w) and the

channel width (W_w). It is observed that the ratio of D_n/W_n is related to the ratio of D_w/W_w[171]; indicating that particles or fluid that are close to the wall in the narrow channel will also tend to be close to the wall in the wide channel. For particles or droplets with a circular shape, the values of D_n and D_w correspond to the radii. However, for particles or droplets with non-circular shapes, the barycenter becomes the reference point. As depicted in Figure 4.2b, even if a large droplet has a unique shape but the same distance from the barycenter to the wall as a small droplet, it can still reach the same D_w in the wide channel.

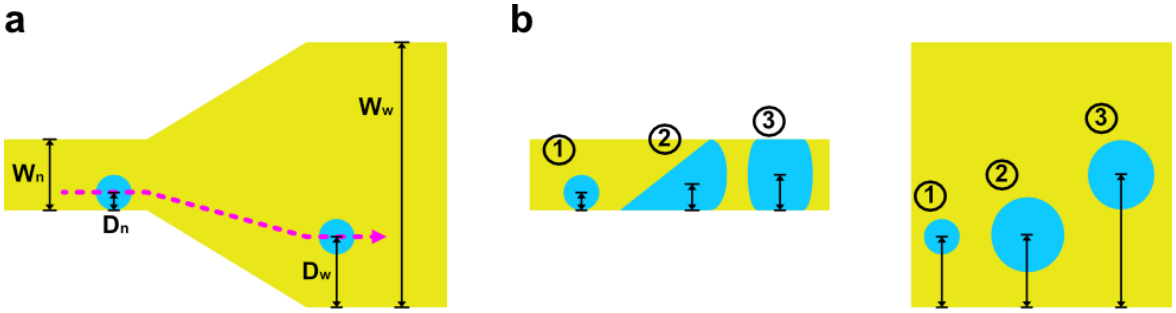

Figure 4.2: The principle of droplet pinched flow fractionation; (a) The related parameters of droplet pinched flow fractionation; (b) The initial position of different droplets and their separated locations.

4.2.2. Theoretical model

The droplet advection in microchannel can be considered as a two-phase flow with the commercial finite element software, COMSOL Multiphysics 6.0 (COMSOL Inc., Burlington, MA, USA). The two-phase flow is governed by coupling system of Navier–Stokes equations and the Cahn–Hilliard equations[121]:

$$\rho\left(\frac{\partial \mathbf{u}}{\partial t}+\mathbf{u}\cdot\nabla\mathbf{u}\right)=\nabla\cdot\left[-\mathrm{p}\mathbf{I}+\mu\left(\nabla\mathbf{u}+\nabla\mathbf{u}^{\mathrm{T}}\right)\right]+\psi\nabla\phi \qquad \text{(Eq.4.1)}$$

$$\frac{\partial \phi}{\partial t} + \mathbf{u} \cdot \nabla \phi = \nabla \cdot (M \nabla \psi)$$

$$\psi = -\nabla \cdot (\lambda \nabla \phi) + \frac{\lambda}{\varepsilon^2} \phi(\phi^2 - 1)$$

where t denotes time; ρ is the fluid density; μ is the dynamic viscosity of the fluid; **u** is the fluid velocity; p is the pressure; **I** is the unitary tensor; λ is the mixing energy density, determined according to the relation between the mixing energy density and surface tension $\sigma = \frac{2\sqrt{2}}{3}\frac{\lambda}{\varepsilon}$; ε is the capillary width, chosen based on the element size; M is the mobility or Onsager coefficient; ϕ is the phase-field variable, with ϕ = ±1 in the two bulk phases and ϕ = 0 on the two-phase interface; ψ is the chemical potential; $\psi\nabla\phi$ is the capillary force[172]. The density and dynamic viscosity are functions of the phase-field variable:

$$\rho = \rho_1 \left(\frac{1-\phi}{2}\right) + \rho_2 \left(\frac{1+\phi}{2}\right)$$

$$\mu = \mu_1 \left(\frac{1-\phi}{2}\right) + \mu_2 \left(\frac{1+\phi}{2}\right) \qquad \text{(Eq.4.2)}$$

where ρ_1 and ρ_2 are the densities of the two fluids, respectively; μ_1 and μ_2 are the dynamic viscosities of the two fluids, respectively. In my simulation, the densities of water (ρ_1) and oil (ρ_2) are set as 1000 kg/m^3 and 820 kg/m^3, while the viscosities of water (μ_1) and oil (μ_2) are 0.001 Pa·s and 0.05 Pa·s.

4.2.3. Chip fabrication

The chip fabrication is based on the new method mentioned in section 2.2.3, the horizontal connecting structure. The fabrication is similar as distribution in section 3.5.3.2. Fig.4.3a shows the microfluidic chip for droplet sorting.

Fig.4.3b shows the layout of the channel, the channel includes two main parts, the droplet generation and the droplet separation. The droplet generation use the T-junction to generate the slug like droplet. When droplet move into the separation channel, it will be firstly pressed to wall by the sheath. After flowing through a narrow channel, droplet will move in to a wider channel, and the separation will happen here. The droplet moving along one side of the narrow channel will generate the different distance between the barycenters of droplets to the wall, and the distance will be extended in the wider wall, leading to the separation.

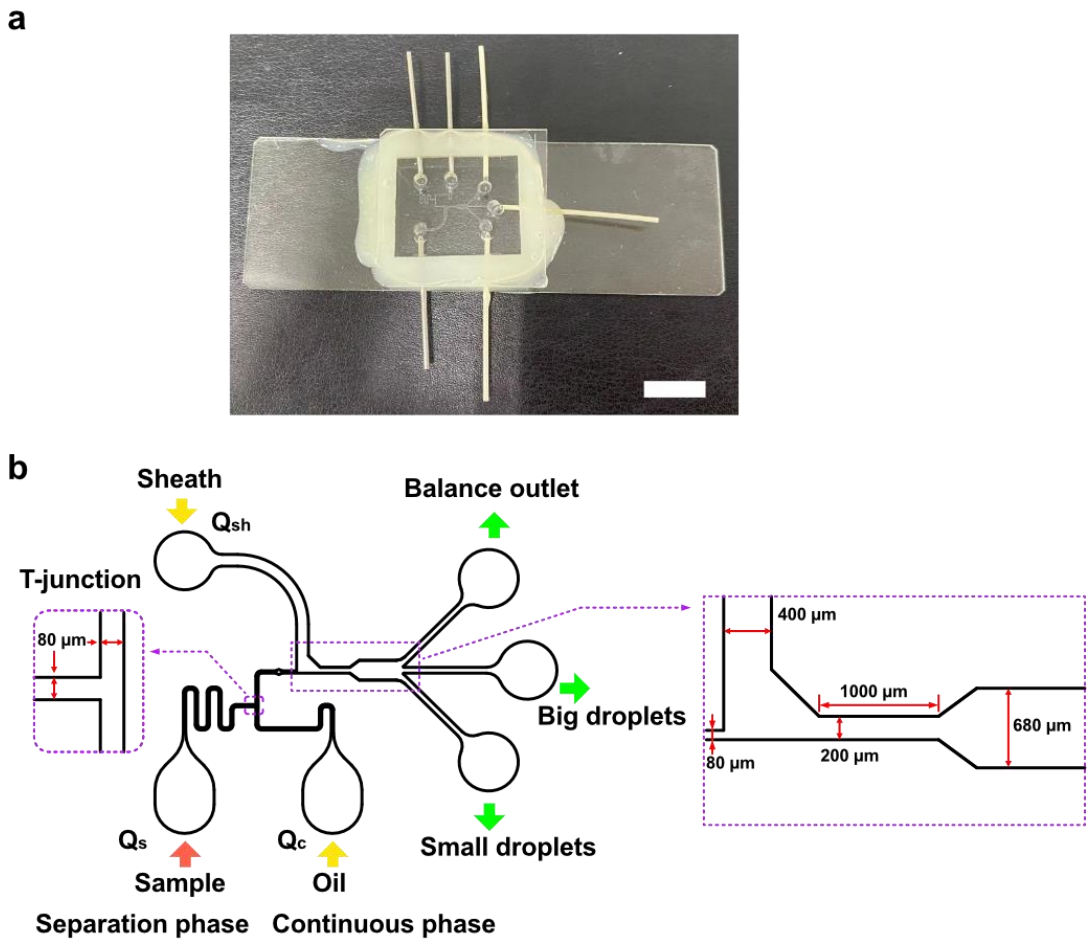

Figure 4.3: The microfluidic device for droplet sorting; (a) the microfluidic chip, scale bar: 1 cm; (b) the layout of microfluidic channel; Q_c, Q_s and Q_{sh} represent the flow rate of continuous phase (oil), separation phase (water) and the sheath (oil), repectively.

4.3. Results and discussion

4.3.1. Simulation of droplet pinched flow fractionation

The simulation mainly investigates the effects of two parameters, the size of droplet and the location of droplet in narrow channel. Like Fig.4.4 shows, the droplet moving along the center line of channel (offset = 0), will keep along the center line of wide channel regardless of the size of droplet; but when the initial position of droplet in narrow channel is not in the center of channel, but have an offset, the droplet will move far from center as moving to wide channel. Fig.4.4 shows droplets with radius of 60 μm and 40 μm and 5 μm from the wall in the narrow channel, as moving into wide channel, droplet will also drift to wall; as large droplet is closer to center, the final location in wide channel will also closer to center too.

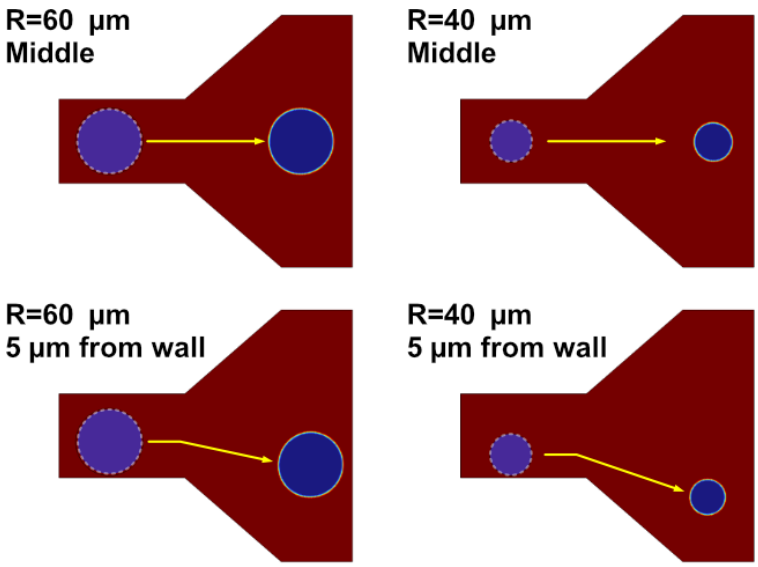

Figure 4.4: The droplet trajectories with different radius (R) or position, the two graphs in the bottom are the droplets start in the location with 5 μm from wall.

Based on the property of laminar flow, the distribution of streamline in narrow channel will be similar to the streamline in the wide channel; the bias mass of droplet in narrow channel can also result in bias mass in wide channel. For example, Fig.4.5 shows the trajectories of droplet with

radius of 60 µm at different initial positions in narrow channel, the initial position is the location of droplet`s barycenter, y=0 represent the middle line of channel. With the same radius, the effect of the initial position directly determines the final position in wide channel, and the relationship is direct ratio. The function of PFF is to enlarge the barycenter distance of different droplet from narrow channel to wide channel.

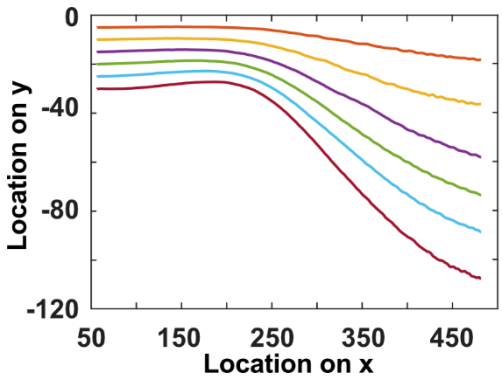

Figure 4.5: The droplet trajectories of droplets with radius of 60 µm at different initial position in narrow channel, (distance between barycenter to middle line ranging from 5 µm to 30 µm).

4.3.2. The droplet PFF experiments and the results

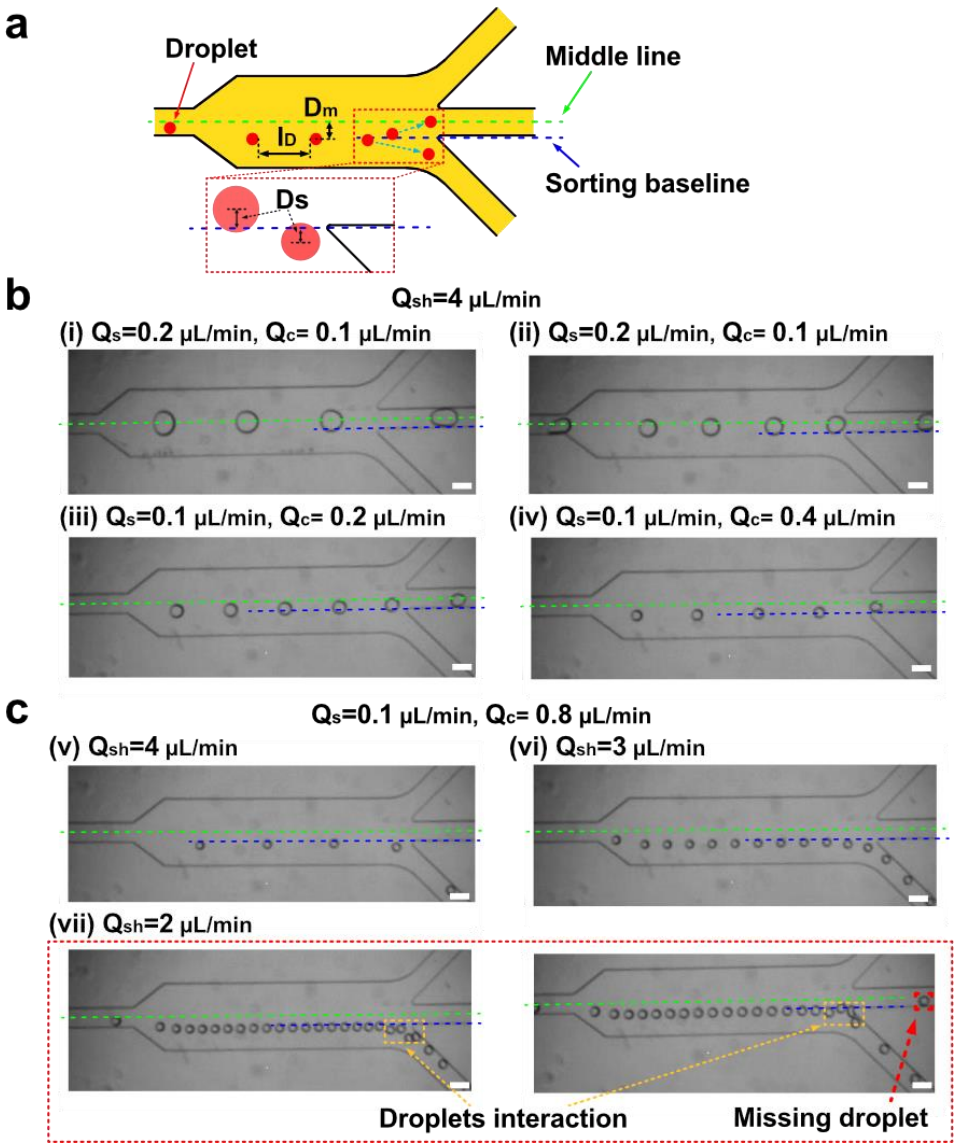

Figure 4.6: The droplet trajectories in experiments; (a) the parameters which affect the trajectories; (b) situations when droplets move to middle outlet, scale bar: 200 μm; (c) situations when droplets move to bottom outlet, scale bar: 200 μm.

In my droplet pinched flow fractionation experiments, I have three controllable parameters: the flow rates of the separation phase (Q_s) and continuous phase (Q_c), which determine the droplet generation, and the flow rate of the sheath flow (Q_{sh}), which controls the interval between droplets. However, these parameters are not directly responsible for determining the sorting result. The droplet pinched flow fractionation process consists of two steps: first, enlarging the distance

between the barycenters of droplets, and then guiding the droplets to different outlets based on their respective positions. These two steps are crucial for achieving successful droplet sorting.

To evaluate the position of droplets, I utilize two reference lines in my analysis. Firstly, I define the distance between the barycenter of the droplet and the middle line of the channel (green dotted line in Figure 4.6a) as D_m. In the case of a sufficiently large droplet moving as a slug in the narrow channel, the barycenter aligns with the middle line, resulting in $D_m = 0$. Larger values of D_m indicate that the droplet is positioned further away from the middle line. Additionally, I introduce the side wall of the middle channel as another significant reference (blue dotted line in Figure 4.6a), referred to as the sorting baseline. If the barycenter of the droplet is located between the middle line and the sorting baseline, the droplet will be directed towards the middle channel. Conversely, if the barycenter of the droplet is positioned on one side of the sorting baseline, closer to the wall, the droplet will be guided towards the side channel. The distance between the droplet and the sorting baseline is defined as D_s.

Figure 4.6b (i-iv) depicts the behavior of droplets with different radius (120 µm, 100 µm, 72 µm, and 60 µm) in the sorting channel, under the same sheath flow rate of 4 µL/min. All droplets move towards the middle channel, and it is evident that the barycenters of these droplets are positioned along the side of the sorting baseline, closer to the middle channel. However, for the droplet with a radius of 50 µm (Fig. 4.6c), its barycenter is located on the opposite side of the sorting baseline, resulting in the droplet being guided towards the side outlet. Based on the observations from Figure 4.6b (i-v), where the interval between droplets is wide enough to accommodate additional droplets, I reduced the sheath flow rate to 3 µL/min and 2 µL/min (total flow rate changes from 3.9 µL/min to 2.9 µL/min) in order to increase the droplet concentration within the sorting channel. This change in flow rate is demonstrated in Figure 4.6b (vi-vii).

In most researches on PFF, the ratio of droplet radius and channel width is used as the evaluation parameters[171], [173]; but as droplet is easily deformed, I just use the diameter of droplet in wide channel as the parameter. Table 5.1 shows the experiment results, the flow rates of the three inlets (Q_s, Q_c and Q_{sh}) cause the various droplet radius (R) and interval (I_D); but the trajectory of droplet is only determined by the radius (R) and width of narrow channel, as when the radius of droplet is larger than half of the width of narrow channel, the droplet directly move along the middle line, then the distance of droplet barycenter to middle line (D_m) is zero, and the distance of barycenter to sorting baseline (D_s) is 100 μm, half width of outlet in my experiments. The key parameter for sorting is D_s, droplet move to middle outlet when $D_s>0$ and move to down outlet when $D_s<0$; to achieve the expected D_s, the radius of droplet should be adjusted based on the width of narrow channel and the outlet channel; like droplet with radius of 50 μm in 200 μm wide narrow channel move to wide channel with 125 μm from middle line (D_m) and 215 μm from wall, but as the outlet channel is also 200 μm wide, the D_m is large than half of the width of outlet channel.

Table 4.1: Experiment results

Q_s (μL/min)	Q_c (μL/min)	Q_{sh} (μL/min)	R (μm)	I_D (μm)	D_m (μm)	D_s (μm)	Outlet
0.4	0.1	4	150	400	0	100	middle
0.2	0.1	4	120	660	0	100	middle
0.2	0.2	4	100	480	40	60	middle
0.1	0.2	4	72	450	70	30	middle
0.1	0.4	4	60	520	85	15	middle
0.1	0.8	4	50	600	125	-25	down
0.1	0.8	3	50	150	125	-25	down
0.1	0.8	2	50	40	125	-25	invalid

However, the small interval can lead the interaction or collision between droplets, like shown in Fig.4.6b(vii); before the outlets, the droplets contact disturbs the trajectory and some droplet may run off, making the PFF unstable. This will be investigated in the next section.

4.3.3. The invalidation of droplet PFF

The droplet PFF works when droplets are moving along a trajectory; however, if droplets can be to closed when moving, the stable trajectory of droplet will be disturbed and lead invalid situations. To keep PFF working, the interference between droplets should be avoided.

When droplet enter the wide channel, the flow velocity will decrease here due to the larger cross-section. The following droplet will catch the front one and causing the interference, the near droplets can disturb the location with each other. Like Fig.4.7a shows, the droplets will generate two trajectories, when the sheath flow is just 1 or 2 μL/min while separation phase and continuous phase are 1 μL/min and 2 μL/min, respectively; in this situation, droplets will move to two outlets along the two trajectories. When increase the sheath to 4 μL/min, the two trajectories combine to one, but the small interval between droplets still disturb the trajectory, causing droplet breaking to two parts and flowing to two outlets. The invalid situations for PFF are mainly caused by low flow rates of sheath.

As the sheath increasing to 16 μL/min, the droplets are divided with interval of 220 μm, like shown in Fig.4.7b; droplet with diameter of 110 μm will flow to the middle outlet in this situation. When increase the continuous phase to 4 μL/min, the diameter of droplets decreases to 90 μm and droplet flow toward to the bottom outlet. Then, the separation of droplets is achieved.

Enough interval of droplets is one of the key points for droplet PFF, as the width of channel for droplet separation is much smaller than the wide separation channel, the interval of droplets is mainly controlled by the sheath flow. Therefore, the flow rate of sheath should be high enough for effective separation.

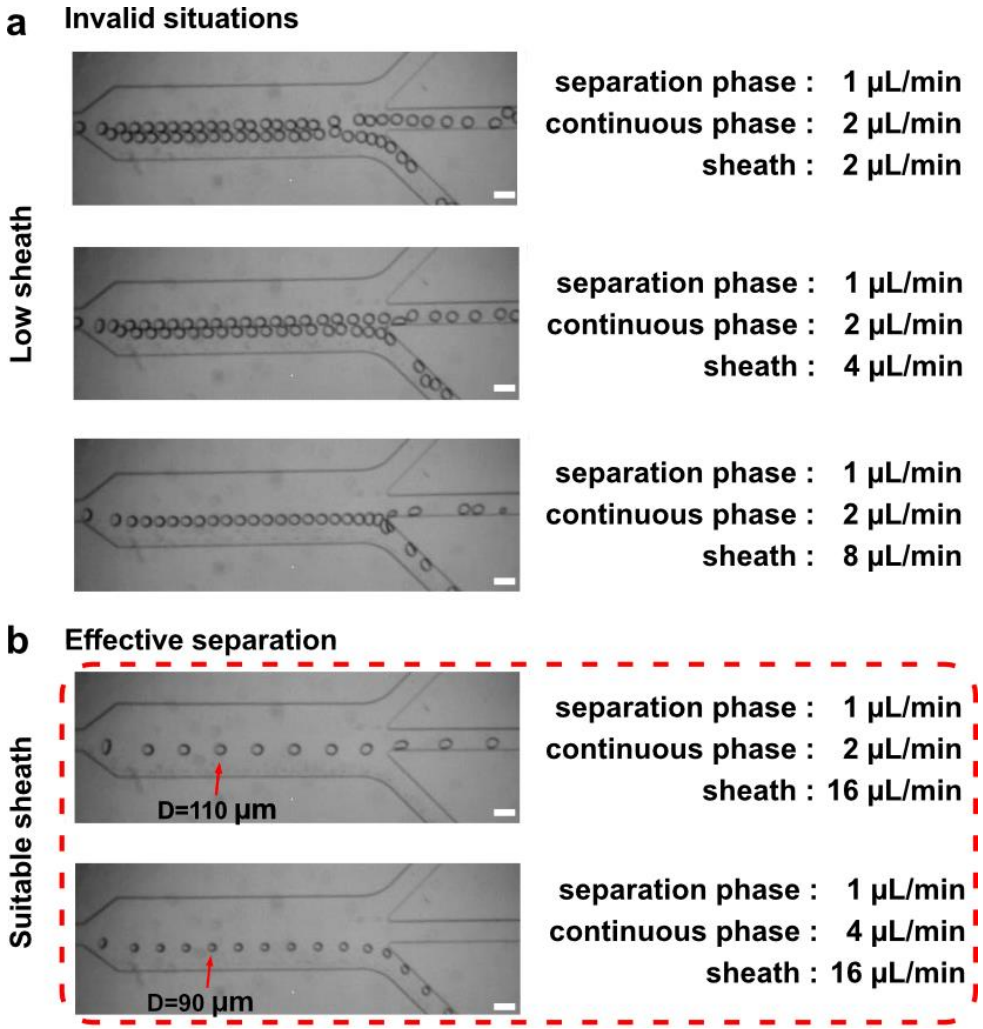

Figure 4.7: Conditions of invalid and working; (a) invalid situations with flow rates ranging from 2 μL/min to 8 μL/min, scale bar: 200 μm; (b) effective separation realized when sheath flow raising to 16 μL/min, droplets with 110 μm and 90 μm can be separated successfully, scale bar: 200 μm.

4.4. Summary

In conclusion, the passive droplet pinched flow fractionation (PFF) method, as a part of my droplet-based cell sorting system, offers an effective and accurate sorting technique for droplets of different sizes. Numerical models were developed to investigate the trajectory of droplets, particularly focusing on the process of enlarging the initial distance between the droplet and the channel wall as it transitions from a narrow channel to a wider channel. Through experimental validation, I discovered that the relative position between the droplet and the sorting baseline directly determines the final sorting outcome. Additionally, it was found that maintaining a sufficiently high sheath flow rate is crucial to ensure proper interval spacing between droplets, preventing interactions that may disrupt trajectory stability and sorting accuracy. By optimizing the sheath flow rate, the device successfully sorts droplets with diameters larger than 110 μm and smaller than 100 μm into separate outlets, which shows the high accuracy toward droplets with small difference. With the theory and principle in my research, droplet separation with all sizes can be designed, more experiments on mixed sample and channel design will be carried in the future.

Importantly, the principles and findings of my research can also be applied to the sorting of particles with various sizes or even shapes. By adjusting the relative position between the barycenter and the sorting baseline, the pinched flow fractionation technique can be easily implemented for efficient sorting of particles in different applications.

5. Conclusion

This dissertation primarily focuses on enhancing the throughput and sensitivity of flow cytometry through the utilization of microfluidic devices. To improve the throughput, I developed a novel structure for a PDMS-based microfluidic chip. This involved horizontally connecting the microfluidic channels and sealing the chip with two glass layers bonded together and resin sealing. This innovative microfluidic chip design, specifically tailored for OTS microscopy, allows for a velocity of 40 m/s, setting a new world record in terms of imaging flow cytometry. The throughput was significantly increased to a minimum of 2,700,000 cells/s. Importantly, this structural concept can be extended to other microfluidic applications, such as impedance flow cytometry, droplet-based assays, and cell hydroporation, providing improved performance across a wide range of techniques.

As very few microfluidic studies have reached such high velocities, certain phenomena in traditional microfluidics may exhibit notable differences. For instance, in my research, I designed a two-layer channel to achieve vertical focusing of cells, thereby enhancing both the throughput and sensitivity of OTS microscopy. Interestingly, I observed distinct focusing effects depending on the flow velocity. At low velocities (<5 m/s), horizontal focusing (focusing to middle) was predominant. However, at high velocities (>20 m/s), vertical focusing (focusing to bottom) became more prominent. Moreover, the effects of high velocity in microfluidic will be developed continuously, shedding light on the intricate behavior of microfluidics at extreme velocities.

In order to enhance the sensitivity of impedance flow cytometry, several optimizations were conducted. These optimizations included minimizing the span of electrodes to increase the amplitude of the signal, implementing viscoelastic focusing for stable particle trajectories and concentrated distributions, and adjusting the electrode configuration for specific objects like

droplets. To achieve a higher amplitude of the signal, femtosecond laser ablation was employed to create 1 μm gaps in the electrodes. This narrower span enhanced the electric field strength, resulting in higher differential voltages and amplitude. As a result, budding yeast cells were successfully recognized in the yeast sample. Similar to the sensitivity improvements in imaging flow cytometry, the position or trajectory of particles or cells has a significant impact on impedance detection accuracy. By developing a horizontal connecting chip capable of withstanding high pressures and driving fluids at high velocities or viscosities, viscoelastic focusing was applied in impedance cytometry. The flow rates ranged from 0.1 μL/min to 64 μL/min, with the focusing effect becoming apparent at flow rates of 2 μL/min. It was also observed that higher velocities could weaken the focusing effect by introducing equilibrium positions. While impedance flow cytometry allows for the detection of cells, it can also be utilized for droplet analysis. However, in many cases, droplet impedance measurements simply utilize the same electrodes used for cell detection, leading to the loss of valuable information in the final differential signal. To address this, numerical investigations of droplet impedance detection were conducted, resulting in the identification of four distinct situations. Through experimental and simulation analyses, it was determined that the optimal configuration for accurate droplet measurement occurs when the slug-shaped droplet is smaller than the middle electrode and the interval between droplets is greater than the middle electrode. The signals recorded by these specific electrode configurations provide concentrated and accurate results for droplet analysis.

The last work is to develop a droplet-based cell sorting system that utilizes a pulse laser to burst selected droplets and employs a passive mechanism for separating droplets based on their size. To achieve effective droplet separation with a smaller difference in diameter, a passive droplet sorting structure was designed. To accomplish this, pinched flow fractionation, a well-researched

technique for cell sorting, was explored for droplet sorting. Simulations and experiments were conducted on pinched flow fractionation, leading to the observation that droplets behave differently compared to cells or particles, as they tend to maintain a consistent shape. This insight served as the basis for the design of the sorting structure, which took into account the location of the droplet's barycenter. Through experimental validation, it was confirmed that droplets with diameters smaller than 100 μm and larger than 110 μm could be successfully separated using the proposed sorting structure.

During my research, I feel the importance of the theorical research on the basic principle. Experiments or simulations can also supply the direct results by failed to reveal some unobvious points which may have some effects beyond thought. In the development of high-throughput microfluidic chip, I spend a lot of time to optimize the channel design to minimize the flow resistance; since I think the question, why the channel should be designed with such long size, the solution flash out that there is no need for the quite long channel. Then, the purpose turns from minish the flow resistance to how to avoid the interference of microfluidic chip with optical components. Finally, with the quite simple design, the high throughput and velocity can be achieved and even become the best. Moreover, with this strong structure, my researches on impedance flow cytometry and droplet application all adopted the horizontal connecting structure for the good leakage-proof and high-pressure tolerance. And I believe, there will be more researches on high inertial effects can be carried with this chip.

Reference

[1] H. R. Safford and H. N. Bischel, “Flow cytometry applications in water treatment, distribution, and reuse: A review,” *Water Res.*, vol. 151, pp. 110–133, 2019, doi: 10.1016/j.watres.2018.12.016.

[2] M. Li, H. Liu, S. Zhuang, and K. Goda, “Droplet flow cytometry for single-cell analysis,” *RSC Adv.*, vol. 11, no. 34, pp. 20944–20960, 2021, doi: 10.1039/d1ra02636d.

[3] A. Vembadi, A. Menachery, and M. A. Qasaimeh, “Cell Cytometry: Review and Perspective on Biotechnological Advances,” *Front. Bioeng. Biotechnol.*, vol. 7, no. JUN, 2019, doi: 10.3389/fbioe.2019.00147.

[4] Y. Guo, S. Baumgart, H. J. Stärk, H. Harms, and S. Müller, “Mass cytometry for detection of silver at the bacterial single cell level,” *Front. Microbiol.*, vol. 8, no. JUL, pp. 1–9, 2017, doi: 10.3389/fmicb.2017.01326.

[5] A. Binek *et al.*, “Flow Cytometry Has a Significant Impact on the Cellular Metabolome,” *J. Proteome Res.*, vol. 18, no. 1, pp. 169–181, 2019, doi: 10.1021/acs.jproteome.8b00472.

[6] Y. Han, Y. Gu, A. C. Zhang, and Y. H. Lo, “Review: Imaging technologies for flow cytometry,” *Lab Chip*, vol. 16, no. 24, pp. 4639–4647, 2016, doi: 10.1039/c6lc01063f.

[7] H. Mikami *et al.*, “Virtual-freezing fluorescence imaging flow cytometry,” *Nat. Commun.*, vol. 11, no. 1, pp. 1–11, 2020, doi: 10.1038/s41467-020-14929-2.

[8] H. Matsumura *et al.*, “Virtual-freezing fluorescence imaging flow cytometry with 5-aminolevulinic acid stimulation and antibody labeling for detecting all forms of circulating tumor cells,” *Lab Chip*, vol. 23, no. 6, pp. 1561–1575, 2023, doi: 10.1039/d2lc00856d.

[9] Y. Suzuki *et al.*, “Label-free chemical imaging flow cytometry by high-speed multicolor stimulated Raman scattering,” *Proc. Natl. Acad. Sci. U. S. A.*, vol. 116, no. 32, pp. 15842–15848, 2019, doi: 10.1073/pnas.1902322116.

[10] A. Kleiber, D. Kraus, T. Henkel, and W. Fritzsche, “Review: Tomographic imaging flow cytometry,” *Lab Chip*, vol. 21, no. 19, pp. 3655–3666, 2021, doi: 10.1039/d1lc00533b.

[11] J. Son, B. Mandracchia, A. D. Silva Trenkle, G. A. Kwong, and S. Jia, “Portable light-sheet optofluidic microscopy for 3D fluorescence imaging flow cytometry,” *Lab Chip*, vol. 23, no. 4, pp. 624–630, 2023, doi: 10.1039/d2lc01024k.

[12] M. Ugawa and S. Ota, “High-Throughput Parallel Optofluidic 3D-Imaging Flow Cytometry,” *Small Sci.*, vol. 2, no. 7, p. 2100126, 2022, doi: 10.1002/smsc.202100126.

[13] T. Tang *et al.*, “Rotation of Biological Cells: Fundamentals and Applications,” *Engineering*, vol. 10, pp. 110–126, 2022, doi: 10.1016/j.eng.2020.07.031.

[14] C. Lei, N. Nitta, Y. Ozeki, and K. Goda, “Optofluidic time-stretch microscopy: recent advances,” *Opt. Rev.*, 2018.

[15] K. Goda and B. Jalali, “Dispersive Fourier transformation for fast continuous single-shot

measurements," *Nat. Photonics*, vol. 7, no. 2, pp. 102–112, 2013, doi: 10.1038/nphoton.2012.359.

[16] Y. Han and Y. H. Lo, "Imaging Cells in Flow Cytometer Using Spatial-Temporal Transformation," *Sci. Rep.*, vol. 5, pp. 1–10, 2015, doi: 10.1038/srep13267.

[17] S. C. Hur, H. T. K. Tse, and D. Di Carlo, "Sheathless inertial cell ordering for extreme throughput flow cytometry," *Lab Chip*, vol. 10, no. 3, pp. 274–280, 2010, doi: 10.1039/b919495a.

[18] G. Holzner, Y. Du, X. Cao, J. Choo, A. J. Demello, and S. Stavrakis, "An optofluidic system with integrated microlens arrays for parallel imaging flow cytometry," *Lab Chip*, vol. 18, no. 23, pp. 3631–3637, 2018, doi: 10.1039/c8lc00593a.

[19] G. Holzner *et al.*, "High-throughput multiparametric imaging flow cytometry: toward diffraction-limited sub-cellular detection and monitoring of sub-cellular processes," *Cell Rep.*, vol. 34, no. 10, p. 108824, 2021, doi: 10.1016/j.celrep.2021.108824.

[20] B. T. Bosworth and M. A. Foster, "High-speed ultrawideband compressed sensing of sparse radio frequency signals," *Conf. Lasers Electro-Optics Eur. - Tech. Dig.*, vol. 2014-Janua, no. 22, pp. 4892–4895, 2014.

[21] R. Li *et al.*, "All-Optical Fourier-Domain-Compressed Time-Stretch Imaging with Low-Pass Filtering," *ACS Photonics*, 2022, doi: 10.1021/acsphotonics.2c01708.

[22] S. Stavrakis, G. Holzner, J. Choo, and A. deMello, "High-throughput microfluidic imaging flow cytometry," *Curr. Opin. Biotechnol.*, vol. 55, pp. 36–43, 2019, doi: 10.1016/j.copbio.2018.08.002.

[23] H. T. Ngoc Le, J. Kim, J. Park, and S. Cho, "A Review of Electrical Impedance Characterization of Cells for Label-Free and Real-Time Assays," *Biochip J.*, vol. 13, no. 4, pp. 295–305, 2019, doi: 10.1007/s13206-019-3401-6.

[24] Z. Zhang, X. Huang, K. Liu, T. Lan, Z. Wang, and Z. Zhu, "Recent advances in electrical impedance sensing technology for single-cell analysis," *Biosensors*, vol. 11, no. 11, 2021, doi: 10.3390/bios11110470.

[25] A. Abdullah *et al.*, "Microfluidic based impedance biosensor for pathogens detection in food products," *Electrophoresis*, vol. 40, no. 4, pp. 508–520, 2019, doi: 10.1002/elps.201800405.

[26] J. Mok, M. N. Mindrinos, R. W. Davis, and M. Javanmard, "Digital microfluidic assay for protein detection," *Proc. Natl. Acad. Sci. U. S. A.*, vol. 111, no. 6, pp. 2110–2115, 2014, doi: 10.1073/pnas.1323998111.

[27] D. C. Spencer, T. F. Paton, K. T. Mulroney, T. J. J. Inglis, J. M. Sutton, and H. Morgan, "A fast impedance-based antimicrobial susceptibility test," *Nat. Commun.*, vol. 11, no. 1, 2020, doi: 10.1038/s41467-020-18902-x.

[28] Y. Feng, L. Huang, P. Zhao, F. Liang, and W. Wang, "A Microfluidic Device Integrating Impedance Flow Cytometry and Electric Impedance Spectroscopy for High-Efficiency Single-Cell Electrical Property Measurement," *Anal. Chem.*, vol. 91, no. 23, pp. 15204–15212, 2019, doi: 10.1021/acs.analchem.9b04083.

[29] K. Mahesh, M. Varma, and P. Sen, "Double-peak signal features in microfluidic impedance flow

cytometry enable sensitive measurement of cell membrane capacitance," *Lab Chip*, vol. 20, no. 22, pp. 4296–4309, 2020, doi: 10.1039/d0lc00744g.

[30] R. Rodriguez-Trujillo, O. Castillo-Fernandez, M. Garrido, M. Arundell, A. Valencia, and G. Gomila, "High-speed particle detection in a micro-Coulter counter with two-dimensional adjustable aperture," *Biosens. Bioelectron.*, vol. 24, no. 2, pp. 290–296, 2008, doi: 10.1016/j.bios.2008.04.005.

[31] R. Reale, A. De Ninno, L. Businaro, P. Bisegna, and F. Caselli, "High-throughput electrical position detection of single flowing particles/cells with non-spherical shape," *Lab Chip*, vol. 19, no. 10, pp. 1818–1827, 2019, doi: 10.1039/c9lc00071b.

[32] T. Tang *et al.*, "Microscopic impedance cytometry for quantifying single cell shape," *Biosens. Bioelectron.*, vol. 193, no. May, p. 113521, 2021, doi: 10.1016/j.bios.2021.113521.

[33] N. Haandbæk, S. C. Bürgel, F. Rudolf, F. Heer, and A. Hierlemann, "Characterization of Single Yeast Cell Phenotypes Using Microfluidic Impedance Cytometry and Optical Imaging," *ACS Sensors*, vol. 1, no. 8, pp. 1020–1027, 2016, doi: 10.1021/acssensors.6b00286.

[34] H. Daguerre, M. Solsona, J. Cottet, M. Gauthier, P. Renaud, and A. Bolopion, "Positional dependence of particles and cells in microfluidic electrical impedance flow cytometry: Origin, challenges and opportunities," *Lab Chip*, vol. 20, no. 20, pp. 3665–3689, 2020, doi: 10.1039/d0lc00616e.

[35] H. Wang, N. Sobahi, and A. Han, "Impedance spectroscopy-based cell/particle position detection in microfluidic systems," *Lab Chip*, vol. 17, no. 7, pp. 1264–1269, 2017, doi: 10.1039/C6LC01223J.

[36] J. Zhong, D. Yang, Y. Zhou, M. Liang, and Y. Ai, "Multi-frequency single cell electrical impedance measurement for label-free cell viability analysis," *Analyst*, vol. 146, no. 6, pp. 1848–1858, 2021, doi: 10.1039/d0an02476g.

[37] T. Tang *et al.*, "Assessment of the electrical penetration of cell membranes using four-frequency impedance cytometry," *Microsystems Nanoeng.*, vol. 8, no. 1, p. 68, Dec. 2022, doi: 10.1038/s41378-022-00405-y.

[38] T. Tang *et al.*, "Impedance-based tracking of the loss of intracellular components in microalgae cells," *Sensors Actuators B Chem.*, vol. 358, no. February, p. 131514, 2022, doi: 10.1016/j.snb.2022.131514.

[39] T. Tang *et al.*, "Machine learning-based impedance system for real-time recognition of antibiotic-susceptible bacteria with parallel cytometry," *Sensors Actuators B Chem.*, vol. 374, no. June 2022, p. 132698, 2023, doi: 10.1016/j.snb.2022.132698.

[40] J. Zhong, M. Liang, and Y. Ai, "Submicron-precision particle characterization in microfluidic impedance cytometry with double differential electrodes," *Lab Chip*, vol. 21, no. 15, pp. 2869–2880, 2021, doi: 10.1039/d1lc00481f.

[41] T. Tang *et al.*, "Parallel Impedance Cytometry for Real-Time Screening of Bacterial Single Cells from Nano- to Microscale," *ACS Sensors*, vol. 7, no. 12, pp. 3700–3709, Oct. 2022, doi: 10.1021/acssensors.2c01351.

[42] C. Petchakup *et al.*, “Microfluidic Impedance-Deformability Cytometry for Label-Free Single Neutrophil Mechanophenotyping,” *Small*, vol. 18, no. 18, 2022, doi: 10.1002/smll.202104822.

[43] D. T. Bacheschi *et al.*, “Overcoming the sensitivity vs. throughput tradeoff in Coulter counters: A novel side counter design,” *Biosens. Bioelectron.*, vol. 168, no. May, p. 112507, 2020, doi: 10.1016/j.bios.2020.112507.

[44] B. K. Ashley, J. Sui, M. Javanmard, and U. Hassan, “Antibody-functionalized aluminum oxide-coated particles targeting neutrophil receptors in a multifrequency microfluidic impedance cytometer,” *Lab Chip*, vol. 22, no. 16, pp. 3055–3066, 2022, doi: 10.1039/d2lc00563h.

[45] F. Caselli, A. De Ninno, R. Reale, L. Businaro, and P. Bisegna, “A novel wiring scheme for standard chips enabling high-accuracy impedance cytometry,” *Sensors Actuators, B Chem.*, vol. 256, pp. 580–589, 2018, doi: 10.1016/j.snb.2017.10.113.

[46] W. Tang, D. Tang, Z. Ni, N. Xiang, and H. Yi, “Microfluidic Impedance Cytometer with Inertial Focusing and Liquid Electrodes for High-Throughput Cell Counting and Discrimination,” *Anal. Chem.*, vol. 89, no. 5, pp. 3154–3161, 2017, doi: 10.1021/acs.analchem.6b04959.

[47] S. Yan and D. Yuan, “Continuous microfluidic 3D focusing enabling microflow cytometry for single-cell analysis,” *Talanta*, vol. 221, p. 121401, 2021, doi: 10.1016/j.talanta.2020.121401.

[48] Y. Gou, Y. Jia, P. Wang, and C. Sun, “Progress of inertial microfluidics in principle and application,” *Sensors (Switzerland)*, vol. 18, no. 6, 2018, doi: 10.3390/s18061762.

[49] R. Rodriguez-Trujillo, C. A. Mills, J. Samitier, and G. Gomila, “Low cost micro-Coulter counter with hydrodynamic focusing,” *Microfluid. Nanofluidics*, vol. 3, no. 2, pp. 171–176, 2007, doi: 10.1007/s10404-006-0113-8.

[50] X. Xuan, J. Zhu, and C. Church, “Particle focusing in microfluidic devices,” *Microfluid. Nanofluidics*, vol. 9, no. 1, pp. 1–16, 2010, doi: 10.1007/s10404-010-0602-7.

[51] J. Hansson, J. M. Karlsson, T. Haraldsson, H. Brismar, W. Van Der Wijngaart, and A. Russom, “Inertial microfluidics in parallel channels for high-throughput applications,” *Lab Chip*, vol. 12, no. 22, pp. 4644–4650, 2012, doi: 10.1039/c2lc40241f.

[52] C. Liu, G. Hu, X. Jiang, and J. Sun, “Inertial focusing of spherical particles in rectangular microchannels over a wide range of Reynolds numbers,” *Lab Chip*, vol. 15, no. 4, pp. 1168–1177, 2015, doi: 10.1039/c4lc01216j.

[53] D. Di Carlo, “Inertial microfluidics,” *Lab Chip*, vol. 9, no. 21, pp. 3038–3046, 2009, doi: 10.1039/b912547g.

[54] H. Amini, W. Lee, and D. Di Carlo, “Inertial microfluidic physics,” *Lab Chip*, vol. 14, no. 15, pp. 2739–2761, 2014, doi: 10.1039/c4lc00128a.

[55] X. Wang, H. Gao, N. Dindic, N. Kaval, and I. Papautsky, “A low-cost, plug-and-play inertial microfluidic helical capillary device for high-throughput flow cytometry,” *Biomicrofluidics*, vol. 11, no. 1, 2017, doi: 10.1063/1.4974903.

[56] A. J. Chung, D. R. Gossett, and D. Di Carlo, “Three dimensional, sheathless, and high-throughput

microparticle inertial focusing through geometry-induced secondary flows," *Small*, vol. 9, no. 5, pp. 685–690, 2013, doi: 10.1002/smll.201202413.

[57] M. Li *et al.*, "Inertial focusing of ellipsoidal: Euglena gracilis cells in a stepped microchannel," *Lab Chip*, vol. 16, no. 22, pp. 4458–4465, 2016, doi: 10.1039/c6lc01118g.

[58] C. Ni, Z. Zhou, Z. Zhu, D. Jiang, and N. Xiang, "Controllable Size-Independent Three-Dimensional Inertial Focusing in High-Aspect-Ratio Asymmetric Serpentine Microchannels," *Anal. Chem.*, Oct. 2022, doi: 10.1021/acs.analchem.2c02361.

[59] E. Pedrol, J. Massons, F. Díaz, and M. Aguiló, "Study of local inertial focusing conditions for spherical particles in asymmetric serpentines," *Fluids*, vol. 5, no. 1, 2020, doi: 10.3390/fluids5010001.

[60] J. Zhang *et al.*, "Fundamentals of differential particle inertial focusing in symmetric sinusoidal microchannels," *Anal. Chem.*, vol. 91, no. 6, pp. 4077–4084, 2019, doi: 10.1021/acs.analchem.8b05712.

[61] S. Yang, J. Y. Kim, S. J. Lee, S. S. Lee, and J. M. Kim, "Sheathless elasto-inertial particle focusing and continuous separation in a straight rectangular microchannel," *Lab Chip*, vol. 11, no. 2, pp. 266–273, 2011, doi: 10.1039/c0lc00102c.

[62] G. Romeo, G. D'Avino, F. Greco, P. A. Netti, and P. L. Maffettone, "Viscoelastic flow-focusing in microchannels: Scaling properties of the particle radial distributions," *Lab Chip*, vol. 13, no. 14, pp. 2802–2807, 2013, doi: 10.1039/c3lc50257k.

[63] M. Serhatlioglu *et al.*, "Viscoelastic Capillary Flow Cytometry," *Adv. NanoBiomed Res.*, vol. 3, no. 2, p. 2200137, Dec. 2023, doi: 10.1002/anbr.202200137.

[64] J. Zhou and I. Papautsky, "Viscoelastic microfluidics: progress and challanges," *Microsystems Nanoeng.*, vol. 6, no. 1, 2020, doi: 10.1038/s41378-020-00218-x.

[65] H. Feng, J. J. Magda, and B. K. Gale, "Viscoelastic second normal stress difference dominated multiple-stream particle focusing in microfluidic channels," *Appl. Phys. Lett.*, vol. 115, no. 26, 2019, doi: 10.1063/1.5129281.

[66] E. Keinan, E. Ezra, and Y. Nahmias, "Opposing shear-induced forces dominate inertial focusing in curved channels and high Reynolds numbers," *Appl. Phys. Lett.*, vol. 107, no. 19, p. 193507, 2015, doi: 10.1063/1.4935466.

[67] S. Tripathi, A. Kumar, Y. V. Bala Varun Kumar, and A. Agrawal, "Three-dimensional hydrodynamic flow focusing of dye, particles and cells in a microfluidic device by employing two bends of opposite curvature," *Microfluid. Nanofluidics*, vol. 20, no. 2, pp. 1–14, 2016, doi: 10.1007/s10404-015-1673-2.

[68] S. C. Lin, P. W. Yen, C. C. Peng, and Y. C. Tung, "Single channel layer, single sheath-flow inlet microfluidic flow cytometer with three-dimensional hydrodynamic focusing," *Lab Chip*, vol. 12, no. 17, pp. 3135–3141, 2012, doi: 10.1039/c2lc40246g.

[69] M. Nasir, D. A. Ateya, D. Burk, J. P. Golden, and F. S. Ligler, "Hydrodynamic focusing of conducting fluids for conductivity-based biosensors," *Biosens. Bioelectron.*, vol. 25, no. 6, pp.

1363–1369, 2010, doi: 10.1016/j.bios.2009.10.033.

[70] G. A. Justin, A. K. Denisin, M. Nasir, L. C. Shriver-Lake, J. P. Golden, and F. S. Ligler, "Hydrodynamic focusing for impedance-based detection of specifically bound microparticles and cells: Implications of fluid dynamics on tunable sensitivity," *Sensors Actuators, B Chem.*, vol. 166–167, pp. 386–393, 2012, doi: 10.1016/j.snb.2012.02.077.

[71] H. Kobayashi *et al.*, "Intelligent whole-blood imaging flow cytometry for simple, rapid, and cost-effective drug-susceptibility testing of leukemia," *Lab Chip*, vol. 19, no. 16, pp. 2688–2698, 2019, doi: 10.1039/c8lc01370e.

[72] A. Malekanfard, S. Beladi-Behbahani, T. R. Tzeng, H. Zhao, and X. Xuan, "AC Insulator-Based Dielectrophoretic Focusing of Particles and Cells in an 'infinite' Microchannel," *Anal. Chem.*, vol. 93, no. 14, pp. 5947–5953, 2021, doi: 10.1021/acs.analchem.1c00697.

[73] Z. Dong, D. Fernandez Rivas, and S. Kuhn, "Acoustophoretic focusing effects on particle synthesis and clogging in microreactors," *Lab Chip*, vol. 19, no. 2, pp. 316–327, 2019, doi: 10.1039/C8LC00675J.

[74] C. Grenvall, C. Antfolk, C. Z. Bisgaard, and T. Laurell, "Two-dimensional acoustic particle focusing enables sheathless chip Coulter counter with planar electrode configuration," *Lab Chip*, vol. 14, no. 24, pp. 4629–4637, 2014, doi: 10.1039/c4lc00982g.

[75] S. H. Kim, M. Antfolk, M. Kobayashi, S. Kaneda, T. Laurell, and T. Fujii, "Highly efficient single cell arraying by integrating acoustophoretic cell pre-concentration and dielectrophoretic cell trapping," *Lab Chip*, vol. 15, no. 22, pp. 4356–4363, 2015, doi: 10.1039/c5lc01065a.

[76] I. Leibacher, P. Reichert, and J. Dual, "Microfluidic droplet handling by bulk acoustic wave (BAW) acoustophoresis," *Lab Chip*, vol. 15, no. 13, pp. 2896–2905, 2015, doi: 10.1039/c5lc00083a.

[77] M. Wu *et al.*, "High-throughput cell focusing and separation: Via acoustofluidic tweezers," *Lab Chip*, vol. 18, no. 19, pp. 3003–3010, 2018, doi: 10.1039/c8lc00434j.

[78] S. Sart, G. Ronteix, S. Jain, G. Amselem, and C. N. Baroud, "Cell Culture in Microfluidic Droplets," *Chemical Reviews*, vol. 122, no. 7. pp. 7061–7096, 2022. doi: 10.1021/acs.chemrev.1c00666.

[79] O. J. Dressler, R. M. Maceiczyk, S. I. Chang, and A. J. Demello, "Droplet-based microfluidics: Enabling impact on drug discovery," *J. Biomol. Screen.*, vol. 19, no. 4, pp. 483–496, 2014, doi: 10.1177/1087057113510401.

[80] T. E. De Groot, K. S. Veserat, E. Berthier, D. J. Beebe, and A. B. Theberge, "Surface-tension driven open microfluidic platform for hanging droplet culture," *Lab Chip*, vol. 16, no. 2, pp. 334–344, 2016, doi: 10.1039/c5lc01353d.

[81] L. Mahler *et al.*, "Highly parallelized droplet cultivation and prioritization on antibiotic producers from natural microbial communities," *Elife*, vol. 10, pp. 1–23, 2021, doi: 10.7554/eLife.64774.

[82] J. M. Lee *et al.*, "Generation of tumor spheroids using a droplet-based microfluidic device for photothermal therapy," *Microsystems Nanoeng.*, vol. 6, no. 1, pp. 0–9, 2020, doi: 10.1038/s41378-

020-0167-x.

[83] A. C. Sun, D. J. Steyer, A. R. Allen, E. M. Payne, R. T. Kennedy, and C. R. J. Stephenson, "A droplet microfluidic platform for high-throughput photochemical reaction discovery," *Nat. Commun.*, vol. 11, no. 1, pp. 1–6, 2020, doi: 10.1038/s41467-020-19926-z.

[84] F. Lussier, O. Staufer, I. Platzman, and J. P. Spatz, "Can Bottom-Up Synthetic Biology Generate Advanced Drug-Delivery Systems?," *Trends Biotechnol.*, vol. 39, no. 5, pp. 445–459, 2021, doi: 10.1016/j.tibtech.2020.08.002.

[85] D. V. Voronin *et al.*, "Detection of rare objects by flow cytometry: Imaging, cell sorting, and deep learning approaches," *Int. J. Mol. Sci.*, vol. 21, no. 7, 2020, doi: 10.3390/ijms21072323.

[86] B. Joo, J. Hur, G. B. Kim, S. G. Yun, and A. J. Chung, "Highly Efficient Transfection of Human Primary T Lymphocytes Using Droplet-Enabled Mechanoporation," *ACS Nano*, vol. 15, no. 8, pp. 12888–12898, 2021, doi: 10.1021/acsnano.0c10473.

[87] A. Jalili, M. Bagheri, A. Shamloo, and A. H. Kazemipour Ashkezari, "A plasmonic gold nanofilm-based microfluidic chip for rapid and inexpensive droplet-based photonic PCR," *Sci. Rep.*, vol. 11, no. 1, pp. 1–13, 2021, doi: 10.1038/s41598-021-02535-1.

[88] F. Schuler *et al.*, "Digital droplet PCR on disk," *Lab Chip*, vol. 16, no. 1, pp. 208–216, 2016, doi: 10.1039/c5lc01068c.

[89] C. Lei, B. Guo, Z. Cheng, and K. Goda, "Optical time-stretch imaging: Principles and applications," *Appl. Phys. Rev.*, vol. 3, no. 1, p. 11102, 2016.

[90] A. K. S. Lau, H. C. Shum, K. K. Y. Wong, and K. K. Tsia, "Optofluidic time-stretch imaging-an emerging tool for high-throughput imaging flow cytometry," *Lab Chip*, vol. 16, no. 10, pp. 1743–1756, 2016, doi: 10.1039/c5lc01458a.

[91] Y. Yalikun *et al.*, "Effects of Flow-Induced Microfluidic Chip Wall Deformation on Imaging Flow Cytometry," *Cytom. Part A*, vol. 97, no. 9, pp. 909–920, 2020, doi: 10.1002/cyto.a.23944.

[92] X. Liu *et al.*, "An optimized PDMS microfluidic device for ultra-fast and high-throughput imaging flow cytometry," *Lab Chip*, p., 2023, doi: 10.1039/d3lc00237c.

[93] X. Liu *et al.*, "Identification of Single Yeast Budding Using Impedance Cytometry with a Narrow Electrode Span," *Sensors*, vol. 22, no. 20, p. 7743, Oct. 2022, doi: 10.3390/s22207743.

[94] C. Lei *et al.*, "High-throughput imaging flow cytometry by optofluidic time-stretch microscopy," *Nat. Protoc.*, vol. 13, no. 7, pp. 1603–1631, 2018, doi: 10.1038/s41596-018-0008-7.

[95] Y. Jiang *et al.*, "Label-free detection of aggregated platelets in blood by machine-learning-aided optofluidic time-stretch microscopy," *Lab Chip*, vol. 17, no. 14, pp. 2426–2434, 2017, doi: 10.1039/c7lc00396j.

[96] M. Ugawa *et al.*, "High-throughput optofluidic particle profiling with morphological and chemical specificity," *Opt. Lett.*, vol. 40, no. 20, p. 4803, 2015, doi: 10.1364/ol.40.004803.

[97] H. Kobayashi *et al.*, "Intelligent whole-blood imaging flow cytometry for simple, rapid, and cost-

effective drug-susceptibility testing of leukemia," *Lab Chip*, vol. 19, no. 16, pp. 2688–2698, 2019, doi: 10.1039/c8lc01370e.

[98] S. Melzig, J. H. Finke, C. Schilde, A. Vierheller, A. Dietzel, and A. Kwade, "Fluid mechanics and process design of high-pressure antisolvent precipitation of fenofibrate nanoparticles using a customized microsystem," *Chem. Eng. J.*, vol. 371, pp. 554–564, 2019, doi: 10.1016/j.cej.2019.04.051.

[99] C. Richter *et al.*, "Innovative process chain for the development of wear resistant 3D metal microsystems," *Microelectron. Eng.*, vol. 110, pp. 392–397, 2013, doi: 10.1016/j.mee.2013.02.078.

[100] Z. B. Qi *et al.*, "Disposable silicon-glass microfluidic devices: Precise, robust and cheap," *Lab Chip*, vol. 18, no. 24, pp. 3872–3880, 2018, doi: 10.1039/c8lc01109e.

[101] Y. Yuan, Y. Yalikun, S. Amaya, Y. Aishan, Y. Shen, and Y. Tanaka, "Fabrication of ultra-thin glass sheet by weight-controlled load-assisted precise thermal stretching," *Sensors Actuators, A Phys.*, vol. 321, p. 112604, 2021, doi: 10.1016/j.sna.2021.112604.

[102] Y. Yalikun, Y. Hosokawa, T. Iino, and Y. Tanaka, "An all-glass 12 μm ultra-thin and flexible micro-fluidic chip fabricated by femtosecond laser processing," *Lab Chip*, vol. 16, no. 13, pp. 2427–2433, 2016, doi: 10.1039/c6lc00132g.

[103] Y. Han, Z. Jiao, J. Zhao, Z. Chao, and Z. You, "A simple approach to fabricate multi-layer glass microfluidic chips based on laser processing and thermocompression bonding," *Microfluid. Nanofluidics*, vol. 25, no. 9, pp. 1–11, 2021, doi: 10.1007/s10404-021-02479-y.

[104] S. Yadavali, H. H. Jeong, D. Lee, and D. Issadore, "Silicon and glass very large scale microfluidic droplet integration for terascale generation of polymer microparticles," *Nat. Commun.*, vol. 9, no. 1, p. 1222, Dec. 2018, doi: 10.1038/s41467-018-03515-2.

[105] T. Tang, Y. Yuan, Y. Yalikun, Y. Hosokawa, M. Li, and Y. Tanaka, "Glass based micro total analysis systems: Materials, fabrication methods, and applications," *Sensors Actuators, B Chem.*, vol. 339, p. 129859, 2021, doi: 10.1016/j.snb.2021.129859.

[106] M. Asgharighajari, N. Amziah, N. Sulaiman, and S. A. Sodeinde, "Design of Microfluidic Sensing and Transport Device," *J. Biomed. Eng. Technol.*, vol. 3, no. 1, pp. 15–20, 2015, [Online]. Available: http://pubs.sciepub.com/jbet/3/1/3

[107] H. S. Damiri and H. K. Bardaweel, "Numerical design and optimization of hydraulic resistance and wall shear stress inside pressure-driven microfluidic networks," *Lab Chip*, vol. 15, no. 21, pp. 4187–4196, 2015, doi: 10.1039/c5lc00578g.

[108] S. Blonski, D. Zaremba, M. Jachimek, S. Jakiela, T. Wacławczyk, and P. M. Korczyk, "Impact of inertia and channel angles on flow distribution in microfluidic junctions," *Microfluid. Nanofluidics*, vol. 24, no. 2, p. 14, 2020, doi: 10.1007/s10404-020-2319-6.

[109] Y. Yalikun, N. Ota, D. Ma, and Y. Tanaka, "Horizontal connection method for glass microfluidic devices," *Micro Nano Lett.*, vol. 15, no. 5, pp. 333–338, 2020, doi: 10.1049/mnl.2019.0603.

[110] Y. Weng *et al.*, "Typing of acute leukemia by intelligent optical time-stretch imaging flow

cytometry on a chip," *Lab Chip*, vol. 23, no. 6, pp. 1703–1712, 2023, doi: 10.1039/d2lc01048h.

[111] M. Frankowski *et al.*, "Microflow cytometers with integrated hydrodynamic focusing," *Sensors (Switzerland)*, vol. 13, no. 4, pp. 4674–4693, 2013, doi: 10.3390/s130404674.

[112] Y. Zhao, Q. Li, and X. Hu, "Universally applicable three-dimensional hydrodynamic focusing in a single-layer channel for single cell analysis," *Anal. Methods*, vol. 10, no. 28, pp. 3489–3497, 2018, doi: 10.1039/c8ay01017j.

[113] Y. J. Chiu, S. H. Cho, Z. Mei, V. Lien, T. F. Wu, and Y. H. Lo, "Universally applicable three-dimensional hydrodynamic microfluidic flow focusing," *Lab Chip*, vol. 13, no. 9, pp. 1803–1809, 2013, doi: 10.1039/c3lc41202d.

[114] Y. M. Patel, S. Jain, A. K. Singh, K. Khare, S. Ahlawat, and S. S. Bahga, "An inexpensive microfluidic device for three-dimensional hydrodynamic focusing in imaging flow cytometry," *Biomicrofluidics*, vol. 14, no. 6, p. 64110, 2020, doi: 10.1063/5.0033291.

[115] M. Li, M. Van Zee, K. Goda, and D. Di Carlo, "Size-based sorting of hydrogel droplets using inertial microfluidics," *Lab Chip*, vol. 18, no. 17, pp. 2575–2582, 2018, doi: 10.1039/c8lc00568k.

[116] P. Liu, H. Liu, D. Yuan, D. Jang, S. Yan, and M. Li, "Separation and enrichment of yeast Saccharomyces cerevisiae by shape using viscoelastic microfluidics," *Anal. Chem.*, vol. 93, no. 3, pp. 1586–1595, 2021, doi: 10.1021/acs.analchem.0c03990.

[117] E. Sollier, C. Murray, P. Maoddi, and D. Di Carlo, "Rapid prototyping polymers for microfluidic devices and high pressure injections," *Lab Chip*, vol. 11, no. 22, pp. 3752–3765, 2011, doi: 10.1039/c1lc20514e.

[118] G. Aspenes, S. Høiland, T. Barth, J. M. Askvik, R. A. Kini, and R. Larsen, "Petroleum hydrate deposition mechanisms: The influence of pipeline wettability," *Proc. ofthe 6th Int. Conf. Gas Hydrates*, no. August, 2008.

[119] H. Yu *et al.*, "Atmospheric and Vacuum Plasma Treatments of Polymer Surfaces for Enhanced Adhesion in Microelectronics Packaging," *Adhes. Microelectron.*, vol. 9781118831, pp. 137–172, 2014, doi: 10.1002/9781118831373.ch4.

[120] T. Zhang *et al.*, "Focusing of sub-micrometer particles in microfluidic devices," *Lab Chip*, vol. 20, no. 1, pp. 35–53, 2020, doi: 10.1039/c9lc00785g.

[121] X. Liu, Y. Ji, Y. Deng, and Y. Wu, "Advection of droplet collision in centrifugal microfluidics," *Phys. Fluids*, vol. 31, no. 3, p. 032003, Mar. 2019, doi: 10.1063/1.5082218.

[122] K. Huang *et al.*, "Deep imaging flow cytometry," *Lab Chip*, vol. 22, no. 5, pp. 876–889, 2022, doi: 10.1039/d1lc01043c.

[123] X. Xie *et al.*, "Optimization of an electrical impedance flow cytometry system and analysis of submicron particles and bacteria," *Sensors Actuators B Chem.*, vol. 360, no. June 2021, p. 131432, 2022, doi: 10.1016/j.snb.2022.131432.

[124] I. Bilican, M. T. Guler, M. Serhatlioglu, T. Kirindi, and C. Elbuken, "Focusing-free impedimetric differentiation of red blood cells and leukemia cells: A system optimization," *Sensors Actuators, B*

Chem., vol. 307, no. August 2019, 2020, doi: 10.1016/j.snb.2019.127531.

[125] D. A. Koutsouras *et al.*, "Probing the Impedance of a Biological Tissue with PEDOT:PSS-Coated Metal Electrodes: Effect of Electrode Size on Sensing Efficiency," *Adv. Healthc. Mater.*, vol. 8, no. 23, 2019, doi: 10.1002/adhm.201901215.

[126] M. T. Guler and I. Bilican, "Capacitive detection of single bacterium from drinking water with a detailed investigation of electrical flow cytometry," *Sensors Actuators, A Phys.*, vol. 269, pp. 454–463, 2018, doi: 10.1016/j.sna.2017.12.008.

[127] J. Cottet, A. Kehren, H. van Lintel, F. Buret, M. Frénéa-Robin, and P. Renaud, "How to improve the sensitivity of coplanar electrodes and micro channel design in electrical impedance flow cytometry: a study," *Microfluid. Nanofluidics*, vol. 23, no. 1, p. 11, Jan. 2019, doi: 10.1007/s10404-018-2178-6.

[128] T. Tang, "FPGA-based system development for high-throughput single-cell detection and sorting from micro to nanoscale," 2022.

[129] T. Tang *et al.*, "Dual-frequency impedance assays for intracellular components in microalgal cells," *Lab Chip*, vol. 22, no. 3, pp. 550–559, 2022, doi: 10.1039/d1lc00721a.

[130] T. Zhang *et al.*, "Focusing of particles in a microchannel with laser engraved groove arrays," *Biosensors*, vol. 11, no. 8, 2021, doi: 10.3390/bios11080263.

[131] T. I. Rukmana *et al.*, "Photoinjection of fluorescent nanoparticles into intact plant cells using femtosecond laser amplifier," *APL Photonics*, vol. 5, no. 6, p. 066104, Jun. 2020, doi: 10.1063/5.0001687.

[132] D. P. Ercan, F. Chrétien, P. Chakravarty, H. R. Flynn, A. P. Snijders, and F. Uhlmann, "Budding yeast relies on G1 cyclin specificity to couple cell cycle progression with morphogenetic development," *Sci. Adv.*, vol. 7, no. 23, pp. 1–14, 2021, doi: 10.1126/sciadv.abg0007.

[133] J. Jiménez, S. Bru, M. P. C. Ribeiro, and J. Clotet, "Live fast, die soon: Cell cycle progression and lifespan in yeast cells," *Microb. Cell*, vol. 2, no. 3, pp. 62–67, 2015, doi: 10.15698/mic2015.03.191.

[134] S. V. Puttaswamy, S. J. Fishlock, D. Steele, Q. Shi, C. Lee, and J. McLaughlin, "Versatile microfluidic platform embedded with sidewall three-dimensional electrodes for cell manipulation," *Biomed. Phys. Eng. Express*, vol. 5, no. 5, p. 055003, Aug. 2019, doi: 10.1088/2057-1976/ab268e.

[135] L. Gong *et al.*, "Direct and Label-Free Cell Status Monitoring of Spheroids and Microcarriers Using Microfluidic Impedance Cytometry," *Small*, vol. 17, no. 21, 2021, doi: 10.1002/smll.202007500.

[136] B. Kim and J. M. Kim, "Elasto-inertial particle focusing under the viscoelastic flow of DNA solution in a square channel," *Biomicrofluidics*, vol. 10, no. 2, 2016, doi: 10.1063/1.4944628.

[137] D. Yuan *et al.*, "Recent progress of particle migration in viscoelastic fluids," *Lab Chip*, vol. 18, no. 4, pp. 551–567, 2018, doi: 10.1039/c7lc01076a.

[138] Me. and numerical study of elasto-inertial focusing in straight channelsohammad A. Raoufi, A. Mashhadian, H. Niazmand, M. Asadnia, A. Razmjou, and M. E. Warkiani, "Experimental and numerical study of elasto-inertial focusing in straight channels," *Biomicrofluidics*, vol. 13, no. 3, 2019, doi: 10.1063/1.5093345.

[139] A. Saateh, A. Kalantarifard, O. T. Celik, M. Asghari, M. Serhatlioglu, and C. Elbuken, "Real-time impedimetric droplet measurement (iDM)," *Lab Chip*, vol. 19, no. 22, pp. 3815–3824, 2019, doi: 10.1039/c9lc00641a.

[140] N. E. Yakdi, F. Huet, and K. Ngo, "Detection and sizing of single droplets flowing in a lab-on-a-chip device by measuring impedance fluctuations," *Sensors Actuators, B Chem.*, vol. 236, pp. 794–804, 2016, doi: 10.1016/j.snb.2016.05.123.

[141] M. Marcali and C. Elbuken, "Impedimetric detection and lumped element modelling of a hemagglutination assay in microdroplets," *Lab Chip*, vol. 16, no. 13, pp. 2494–2503, 2016, doi: 10.1039/c6lc00623j.

[142] J. Panwar and R. Roy, "Integrated Field's metal microelectrodes based microfluidic impedance cytometry for cell-in-droplet quantification," *Microelectron. Eng.*, vol. 215, no. March, p. 111010, 2019, doi: 10.1016/j.mee.2019.111010.

[143] N. Tottori and T. Nisisako, "Particle/cell separation using sheath-free deterministic lateral displacement arrays with inertially focused single straight input," *Lab Chip*, vol. 20, no. 11, pp. 1999–2008, 2020, doi: 10.1039/d0lc00354a.

[144] F. Tian *et al.*, "Microfluidic co-flow of Newtonian and viscoelastic fluids for high-resolution separation of microparticles," *Lab Chip*, vol. 17, no. 18, pp. 3078–3085, 2017, doi: 10.1039/c7lc00671c.

[145] F. Tian *et al.*, "Label-free isolation of rare tumor cells from untreated whole blood by interfacial viscoelastic microfluidics," *Lab Chip*, vol. 18, no. 22, pp. 3436–3445, 2018, doi: 10.1039/c8lc00700d.

[146] J. Nam *et al.*, "Sheathless shape-based separation of candida albicans using a viscoelastic non-newtonian fluid," *Micromachines*, vol. 10, no. 12, pp. 1–14, 2019, doi: 10.3390/mi10120817.

[147] T. Zhang *et al.*, "Shape-based separation of drug-treated Escherichia coli using viscoelastic microfluidics," *Lab Chip*, vol. 22, no. 15, pp. 2801–2809, 2022, doi: 10.1039/d2lc00339b.

[148] Z. Ma, Y. Zhou, D. J. Collins, and Y. Ai, "Fluorescence activated cell sorting: Via a focused traveling surface acoustic beam," *Lab Chip*, vol. 17, no. 18, pp. 3176–3185, 2017, doi: 10.1039/c7lc00678k.

[149] N. Nitta *et al.*, "Intelligent Image-Activated Cell Sorting," *Cell*, vol. 175, no. 1, pp. 266-276.e13, 2018, doi: 10.1016/j.cell.2018.08.028.

[150] Z. Y. Hong, K. Okano, D. Di Carlo, Y. Tanaka, Y. Yalikun, and Y. Hosokawa, "High-speed micro-particle manipulation in a microfluidic chip by directional femtosecond laser impulse," *Sensors Actuators, A Phys.*, vol. 297, p. 111566, 2019, doi: 10.1016/j.sna.2019.111566.

[151] M. Tenje, A. Fornell, M. Ohlin, and J. Nilsson, "Particle Manipulation Methods in Droplet

Microfluidics," *Anal. Chem.*, vol. 90, no. 3, pp. 1434–1443, 2018, doi: 10.1021/acs.analchem.7b01333.

[152] M. Chabert and J. L. Viovy, "Microfluidic high-throughput encapsulation and hydrodynamic self-sorting of single cells," *Proc. Natl. Acad. Sci. U. S. A.*, vol. 105, no. 9, pp. 3191–3196, 2008, doi: 10.1073/pnas.0708321105.

[153] A. Isozaki *et al.*, "Sequentially addressable dielectrophoretic array for high-throughput sorting of large-volume biological compartments," *Sci. Adv.*, vol. 6, no. 22, pp. 1–12, 2020, doi: 10.1126/sciadv.aba6712.

[154] H. Zhang *et al.*, "FIDELITY: A quality control system for droplet microfluidics," *Sci. Adv.*, vol. 8, no. 27, pp. 1–12, 2022, doi: 10.1126/sciadv.abc9108.

[155] H. Huang, Y. Yu, Y. Hu, X. He, O. Berk Usta, and M. L. Yarmush, "Generation and manipulation of hydrogel microcapsules by droplet-based microfluidics for mammalian cell culture," *Lab Chip*, vol. 17, no. 11, pp. 1913–1932, 2017, doi: 10.1039/c7lc00262a.

[156] P. Zhu and L. Wang, "Passive and active droplet generation with microfluidics: a review," *Lab Chip*, vol. 17, no. 1, pp. 34–75, 2017, doi: 10.1039/C6LC01018K.

[157] O. Sartipzadeh, S. M. Naghib, A. Seyfoori, M. Rahmanian, and F. S. Fateminia, "Controllable size and form of droplets in microfluidic-assisted devices: Effects of channel geometry and fluid velocity on droplet size," *Mater. Sci. Eng. C*, vol. 109, no. August 2019, 2020, doi: 10.1016/j.msec.2019.110606.

[158] S. van Loo, S. Stoukatch, M. Kraft, and T. Gilet, "Droplet formation by squeezing in a microfluidic cross-junction," *Microfluid. Nanofluidics*, vol. 20, no. 10, pp. 1–12, 2016, doi: 10.1007/s10404-016-1807-1.

[159] P. Garstecki, M. J. Fuerstman, H. A. Stone, and G. M. Whitesides, "Formation of droplets and bubbles in a microfluidic T-junction - Scaling and mechanism of break-up," *Lab Chip*, vol. 6, no. 3, pp. 437–446, 2006, doi: 10.1039/b510841a.

[160] S. Malekzadeh and E. Roohi, "Investigation of Different Droplet Formation Regimes in a T-junction Microchannel Using the VOF Technique in OpenFOAM," *Microgravity Sci. Technol.*, vol. 27, no. 3, pp. 231–243, 2015, doi: 10.1007/s12217-015-9440-2.

[161] A. Venkateshwarlu and R. P. Bharti, "Effects of capillary number and flow rates on the hydrodynamics of droplet generation in two-phase cross-flow microfluidic systems: Hydrodynamics of droplet generation in two-phase cross-flow microfluidic systems," *J. Taiwan Inst. Chem. Eng.*, vol. 129, pp. 64–79, 2021, doi: 10.1016/j.jtice.2021.07.045.

[162] F. Ahmadi, K. Samlali, P. Q. N. Vo, and S. C. C. Shih, "An integrated droplet-digital microfluidic system for on-demand droplet creation, mixing, incubation, and sorting," *Lab Chip*, vol. 19, no. 3, pp. 524–535, 2019, doi: 10.1039/c8lc01170b.

[163] É. Boulais, R. Lachaine, and M. Meunier, "Plasma mediated off-resonance plasmonic enhanced ultrafast laser-induced nanocavitation," *Nano Lett.*, vol. 12, no. 9, pp. 4763–4769, 2012, doi: 10.1021/nl302200w.

[164] J. McGrath, M. Jimenez, and H. Bridle, “Deterministic lateral displacement for particle separation: A review,” *Lab Chip*, vol. 14, no. 21, pp. 4139–4158, 2014, doi: 10.1039/c4lc00939h.

[165] T. Murakami, K. Koiwai, and H. Suzuki, “Applying deterministic lateral displacement cell separation on immune cells of Marine shrimp,” *Sensors Actuators B Chem.*, vol. 347, no. August, p. 130587, 2021, doi: 10.1016/j.snb.2021.130587.

[166] T. Salafi, Y. Zhang, and Y. Zhang, *A Review on Deterministic Lateral Displacement for Particle Separation and Detection*, vol. 11, no. 1. Springer Singapore, 2019. doi: 10.1007/s40820-019-0308-7.

[167] X. Lu and X. Xuan, “Elasto-Inertial Pinched Flow Fractionation for Continuous Shape-Based Particle Separation,” *Anal. Chem.*, vol. 87, no. 22, pp. 11523–11530, 2015, doi: 10.1021/acs.analchem.5b03321.

[168] M. Pødenphant, R. Marie, T. Olesen, M. Matteucci, and A. Kristensen, “Injection molded pinched flow fractionation device for enrichment of somatic cells in cow milk,” *Microelectron. Eng.*, vol. 124, pp. 53–57, 2014, doi: 10.1016/j.mee.2014.04.018.

[169] M. Yamada, M. Nakashima, and M. Seki, “Pinched flow fractionation: Continuous size separation of particles utilizing a laminar flow profile in a pinched microchannel,” *Anal. Chem.*, vol. 76, no. 18, pp. 5465–5471, 2004, doi: 10.1021/ac049863r.

[170] J. Takagi, M. Yamada, M. Yasuda, and M. Seki, “Continuous particle separation in a microchannel having asymmetrically arranged multiple branches,” *Lab Chip*, vol. 5, no. 7, pp. 778–784, 2005, doi: 10.1039/b501885d.

[171] M. P. Kok, T. Segers, and M. Versluis, “Bubble sorting in pinched microchannels for ultrasound contrast agent enrichment,” *Lab Chip*, vol. 15, no. 18, pp. 3716–3722, 2015, doi: 10.1039/c5lc00370a.

[172] P. Yue, C. Zhou, J. J. Feng, C. F. Ollivier-Gooch, and H. H. Hu, “Phase-field simulations of interfacial dynamics in viscoelastic fluids using finite elements with adaptive meshing,” *J. Comput. Phys.*, vol. 219, no. 1, pp. 47–67, 2006, doi: 10.1016/j.jcp.2006.03.016.

[173] K. B. Andersen, S. Levinsen, W. E. Svendsen, and F. Okkels, “A generalized theoretical model for ‘continuous particle separation in a microchannel having asymmetrically arranged multiple branches,’” *Lab Chip*, vol. 9, no. 11, pp. 1638–1639, 2009, doi: 10.1039/b822959g.

Achievements

1. First author Journal articles

[1] **Xun Liu**[#], Jiehua Zhou[#], Ruopeng Yan, Tao Tang, Shubin Wei, Rubing Li, Dan Hou, Yueyun Weng, Du Wang, Hui Shen, Fuling Zhou, Yo Tanaka, Ming Li, Yoichiroh Hosokawa, Yaxiaer Yalikun[*], and Cheng Lei[*], "An optimized PDMS microfluidic device for ultra-fast and high-throughput imaging flow cytometry", **Lab on a chip**. (2023), https://doi.org/10.1039/D3LC00237C. (Impact factor: 6.1)

[2] **Xun Liu**, Tao Tang, Po-Wei Yi, Yapeng Yuan, Cheng Lei, Ming Li, Yo Tanaka, Yoichiroh Hosokawa and Yaxiaer Yalikun[*], "Identification of Single Yeast Budding Using Impedance Cytometry with a Narrow Electrode Span", **Sensors**. (2022), https://doi.org/10.3390/s22207743. (Impact factor: 3.9)

[3] Tao Tang[#], **Xun Liu**[#], Yapeng Yuan, Tianlong Zhang, Royata Kiya, Kengo Suzuki, Yo Tanaka, Ming Li, Yoichiroh Hosokawa and Yaxiaer Yalikun[*]"Impedance-based tracking of the loss of intracellular components in microalgae cells", **Sensors and Actuators B: Chemical**. (2022). https://doi.org/10.1016/j.snb.2022.131514. (Impact factor: 7.2)

2. Co-author Journal articles

[1] Yapeng Yuan, Doudou Ma, **Xun Liu**, Tao Tang, Ming Li, Yang Yang, Yaxiaer Yalikun, Yo Tanaka[*], "10 μm thick ultra-thin glass sheet to realize a highly sensitive cantilever for precise cell stiffness measurement", **Lab on a chip**. (2023), https://doi.org/10.1039/D3LC00113J. (Impact factor: 6.1)

[2] Yigang Shen, Yapeng Yuan, **Xun Liu**, Tao Tang, Yaxiaer Yalikun, and Yo Tanaka*, "Multiscale Integrated Temperature/Flow Velocity Sensor Patches for Microfluidic Applications", **IEEE Sensors Journal**. (2023), https://doi.org/10.1109/JSEN.2022.3230692. (Impact factor: 4.3)

[3] Yo Tanaka*, Satoshi Amaya, Shunichi Funano, Hisashi Sugawa, Wataru Nagafuchi, Yuri Ito, Yusufu Aishan, **Xun Liu**, Norihiro Kamamichi and Yaxiaer Yalikun, "A pressure driven electric energy generator exploiting a micro- to nano-scale glass porous filter with ion flow originating from water", **Scientific Reports**. (2022), https://doi.org/10.1109/JSEN.2022.3230692. (Impact factor: 4.9)

[4] Tao Tang, **Xun Liu**, Yapeng Yuan, Ryota Kiya, Tianlong Zhang, Yang Yang, Shiro Suetsugu, Yoichi Yamazaki, Nobutoshi Ota, Koki Yamamoto, Hironari Kamikubo, Yo Tanaka, Ming Li, Yoichiroh Hosokawa, Yaxiaer Yalikun*, "Machine learning-based impedance system for real-time recognition of antibiotic-susceptible bacteria with parallel cytometry", Sen**sors and Actuators B: Chemical**. (2023), https://doi.org/10.1016/j.snb.2022.132698. (Impact factor: 7.2)

[5] Tao Tang, **Xun Liu**, Yapeng Yuan, Tianlong Zhang, Ryota Kiya, Yang Yang, Yoichi Yamazaki, Hironari Kamikubo, Yo Tanaka, Ming Li, Yoichiroh Hosokawa, and Yaxiaer Yalikun*, "Parallel Impedance Cytometry for Real-Time Screening of Bacterial Single Cells from Nano to Microscale", **ACS Sensors**. (2022), https://doi.org/10.1021/acssensors.2c01351. (Impact factor: 9)

[6] Tao Tang, **Xun Liu**, Yapeng Yuan, Tianlong Zhang, Royata Kiya, Kengo Suzuki, Yang Yang, Yo Tanaka, Ming Li, Yoichiroh Hosokawa and Yaxiaer Yalikun*, "Assessment of electrical penetration of cell membrane using four-frequency impedance cytometry", **Microsystems & Nanoengineering**. (2022), https://doi.org/10.1038/s41378-022-00405-y. (Impact factor: 7.7)

[7] Tao Tang, **Xun Liu**, Yapeng Yuan, Royata Kiya, Yigang Shen, Tianlong Zhang, Kengo Suzuki, Ming Li, Yo Tanaka, Yoichiroh Hosokawa and Yaxiaer Yalikun*, "Dual-frequency impedance assays for intracellular components in microalgal cells", **Lab on a chip**. (2022), https://doi.org/10.1039/d1lc00721a. (Impact factor: 6.1)

[8] Tao Tang, **Xun Liu**, Yigang Shen, Yapeng Yuan, Tianlong Zhang, Yo Tanaka, Kengo Suzuki, Ming Li, Yoichiroh Hosokawa and Yaxiaer Yalikun*, "Microscopic impedance cytometry for single-cell shape characterization", **Biosensors and Bioelectronics**. (2021). https://doi.org/10.1016/j.bios.2021.113521. (Impact factor: 10.8)

[9] Ruopeng Yan, **Xun Liu**, Shuang Zhao, Chi Zhang, Liang Wang, Yaxiaer Yalikun, Du Wang, Cheng Lei, "A cost-effective and high-sensitivity optofluidic refractive index sensor for rapid edible oil analysis", **IEEE Sensors Journal**. (Under review)

[10] Dian Anggraini, Tianlong Zhang, **Xun Liu**, Kazunori Okano, Yo Tanaka, Naoyuki Inagaki, Ming Li, Yoichiroh Hosokawa, Sohei Yamada, Yaxiaer Yalikun, "Guided Axon Outgrowth of Neurons by Molecular Gradients Generated from Femtosecond Laser-Fabricated Micro-Holes", **Talanta**. (Under review)

3.Conference:

[1] **Xun Liu**, Jiehua Zhou, Tao Tang, Yoichiroh Hosokawa, Yaxiaer Yalikun and Cheng Lei, "Ultra high-throughput cell imaging enabled by optimized microfluidic device with horizontal connection", The 26th International Conference on Miniaturized Systems for Chemistry and Life Sciences (**μTAS 2022- Poster presentation**)

[2] **Xun Liu**, Tao Tang, Yoichiroh Hosokawa and Yaxiaer Yalikun, “The effects of differential impedance signal on droplet measurement”, The 27th International Conference on Miniaturized Systems for Chemistry and Life Sciences (**μTAS 2023- Poster presentation**)

4.Patent:

[1] Cheng Lei, **Xun Liu**, Jiehua Zhou, “The fabrication and application of the microfluidic chip with 3-D focusing and high throughput (一种三维聚焦的高通量微流控芯片及其应用和制作方法)”, application request number: 2023106676888

[2] Cheng Lei, Jiehua Zhou, **Xun Liu**, “A method to realize quick location of observation area on microfluidic chip(一种微流控芯片、快速定位样品观测区域的方法及系统)”, application request number: 2023107880482

Acknowledgements

This work was funded by many foundations like Grant-in-Aid funding from the NAIST, Amada Foundation, NSG Foundation and so on. I am grateful for all the financial support, which enabled me to carry out my experiments and researches.

It will be impossible for me to finish my research without the support and guidance from Professor Hosokawa, Professor Yaxiaer from NAIST and Professor Lei from Wuhan University, I would like to express my sincere appreciation and gratitude. I still remember just before my enrollment to NAIST, I lived in Wuhan where suffer the COVID-19; the lockdown and the limitation of international travel makes my doctor career ambiguous. Fortunately, I can carry my research in Lei`s lab of Wuhan University where I carried out the most important research there. Although the pandemic brought many difficulties for me, the difficulties firm my determination for researches on microfluidic which have the potential to achieve fast, simple detection of many biological indicator to tackle problems in pandemic.

I also thanks to Prof. Li Ming, she has given me many suggestions of English writing and helped me check the manuscripts. And I thanks to Dr. Tang, we carried the research on impedance flow cytometry together, he also helps me a lot. Then, I thanks to the Dr. Yan and Dr. Zhou, with your assistance on campus life and experiments, all things go right when I was in Wuhan University.

Additionally, I would like to extend my acknowledgement to all members of Bio-Process Engineering Laboratory (生体プロセス工学研究室) in NAIST and Laser and Fast Imaging Laboratory (激光与超快成像实验室) in Wuhan University for the cooperation and discussion. I wish all members and faculties have the bright and beautiful future.

At last, thanks to my family, for my wife and parents support me to continue my doctor career in these years. And, I would like to thank myself for my struggle in these years. I will keep moving forward.